UNIVERSITY OF SOUTHAMPTON

FACULTY OF PHYSICAL SCIENCES AND ENGINEERING

School of Physics and Astronomy

Vibrational and Electronic Excitations of Two Atom Diameter Mercury Telluride Nanowires Studied By Resonance Raman Spectroscopy

by

Joseph H. Spencer

Thesis for the degree of Doctor of Philosophy

August 2016

UNIVERSITY OF SOUTHAMPTON

ABSTRACT

FACULTY OF PHYSICAL SCIENCES AND ENGINEERING
School of Physics and Astronomy

Doctor of Philosophy

VIBRATIONAL AND ELECTRONIC EXCITATIONS OF TWO ATOM DIAMETER MERCURY TELLURIDE NANOWIRES STUDIED BY RESONANCE RAMAN SPECTROSCOPY

by Joseph H. Spencer

This thesis presents the results from a temperature dependant resonance Raman spectroscopy study of HgTe extreme nanowires embedded within SWCNTs. Extreme nanowires are nanowires at the absolute limits of the nanoscale, in this case, just 1-2 atoms in diameter. This work demonstrates that due to the effect of quantum confinement on the electronic wavefunction and the reordering of atoms creating a new allotrope of HgTe never previously measured, new physics of 1D materials is observed. In this body of work we perform resonance Raman spectroscopy experiments with excitation photon energies of 1.65eV to 1.90eV and sample temperatures between 4-300K on an ensemble of HgTe filled single-walled carbon nanotubes. The Raman spectra are analysed and show that 1D HgTe within a SWCNT exhibits new Raman peaks not associated with modification of the bulk material. We couple the Raman results with HRTEM and utilise symmetry arguments to propose two of the fundamental vibrational modes at 47cm^{-1} and 52cm^{-1} are associated with vibrations with B_g and A_g symmetry respectively. Most strikingly, our results indicate a decrease in the rate of Raman scattering as a function of increasing temperature, not clearly in-line with the expected behaviour of Raman scattering due to an increase in the thermal phonon population. Through detailed analysis of temperature dependent resonance Raman data we can understand this effect in terms of broadening of the linewidth of the optical transition. We set out the evidence that this result can be understood by a model in which the resonance's broadening is dominated by the coherence lifetime broadening. This allows us to determine the coherence lifetime of the underlying optical transition: 9fs at 295K and 18fs at 50K. The results are compared with similar results on carbon nanotubes which suggests that the optical transitions responsible for the Raman resonances are excitonic and is likely general to small diameter nanowires. A review of existing and comparable Raman measurements on such nanowires is presented and the implications of the main results in this thesis are discussed in terms of a general interest to the wider physics community.

Contents

List of Figures

List of Tables

Declaration of Authorship

I, Joseph H. Spencer , declare that the thesis entitled *Vibrational and Electronic Excitations of Two Atom Diameter Mercury Telluride Nanowires Studied By Resonance Raman Spectroscopy* and the work presented in the thesis are both my own, and have been generated by me as the result of my own original research. I confirm that:

- this work was done wholly or mainly while in candidature for a research degree at this University;
- where any part of this thesis has previously been submitted for a degree or any other qualification at this University or any other institution, this has been clearly stated;
- where I have consulted the published work of others, this is always clearly attributed;
- where I have quoted from the work of others, the source is always given. With the exception of such quotations, this thesis is entirely my own work;
- I have acknowledged all main sources of help;
- where the thesis is based on work done by myself jointly with others, I have made clear exactly what was done by others and what I have contributed myself;
- parts of this work have been published as: [1] and [8]

Signed:.....

Date:.....

Acknowledgements

First and foremost, I would like to express my most sincere gratitude to my supervisor, Prof. David Smith, who has guided, encouraged and supported me throughout the duration of this research project. I am truly grateful for the time and effort he has put in guiding me over the years.

Another academic I would like to thank is Prof. Jeremy Sloan of Warwick University. Jeremy was a key pioneer in the field of filled nanotubes and I thank him for his advice, discussions, visits and providing HRTEM images that supplement this thesis.

In addition I would like to convey my thanks to the workshop team for their input in helping fabricate the equipment and providing ingenious engineering solutions to the Raman system. An extra thank-you goes to Zondy Webber and Kathleen LeBlanc for their support in my clean room endeavours.

I would like to express a deep thanks to all members of the QLM group for their advice, support and friendship over the last few years. You have all been supportive and helped make this process a lot easier for me. Liam McDonnell has been a notable boost to the group and has assisted me in collecting portions of the data presented in this thesis. I wish him the best of luck with his PhD and research. Dr. John Nesbitt, I thank for providing passing me the keys to the Raman system. Dr. Andrew Turnbull I thank for being there to provide advice on how to write a PhD and being there at the pub on Friday's. Specifically I'd like to thank my friend Paul Gow, who has gone through this whole process with me and has made my PhD life a lot more interesting. I wish them all the best and the continued successes of the QLM group!

I'd also like to thank my family, Nicky, Ron and Aaron Spencer for their support and love over so many years. I hope they enjoy reading this as much as I did writing it.

Finally, Ashlea O'Neill deserves a special mention for being my emotional rock for the last few years and helping me through writing this thesis. She has been with me since the start, through the highs and lows of PhD life, and I count myself lucky every day that I met her. I couldn't have done it without her.

To my family...

Chapter 1

Introduction

Quantum engineering on nanoscale structures with reduced dimensionality has led to a huge range of exciting new physics and technology. Varying the number of quantum confined dimensions has allowed the production of quantum wells[9, 10], wires[11], and dots [12] which has lead to a wide range of new physics and applications in each case. The physics of nanowires has many unique features. Quantum confinement in two dimensions leads to strong van Hove singularities in the electronic density of states [13]. Enhancement of the electrostatic interaction between electrons and holes leads to very strong excitonic effects in semiconductor nanowires[14, 15]. The restriction of the electrons to a single degree of motional freedom leads to a strong tendency towards Peierl's distortions [16] and significantly reduced electronic screening in metallic systems leads to Luttinger liquids [17, 18]. Many of these 1D physical phenomena can be observed for relatively large diameter nanowires; e.g. quantum confinement requires nanowires smaller than the coherence length and is commonly observed in nanowires with diameters of 100nm ($\sim$1000 atoms). However these effects are enhanced as the diameter of the nanowires decreases, for example quantum confinement energies of the order of 1eV are possible in single walled carbon nanotubes [13] and quantized conductance can be observed in metallic atomic chains [19, 20]. In addition as the diameter of the nanowires decrease to a few atoms, new 1D phenomena occur such as rearrangement of bonding leading to new allotropes of materials not stable in bulk form [5]. As this example shows, few atom diameter nanowires are extreme in two senses; they are the limit of miniaturization of nanowires and they have entirely new properties due to their size.

One of the most versatile and successful methods for producing extreme nanowires with diameters in the range 1-3 atoms is filling the central pore of single walled carbon nanotubes (SWCNTs) [21]. This method can be used to produce extreme nanowires of metals, e.g. Fe [22], Ni [23], Ag [24] and Cu [25], semiconductors, e.g. S [26], Te [27] and Se [28, 29] and insulators, e.g CsI [30].

Raman spectroscopy has a proven track record in elucidating the physics of nanowires and acting as a key characterization tool for samples used in a wide range of other

studies. This is particularly true in the field of carbon nanotubes [4, 31, 32]. Raman spectroscopy has already been applied to study SWCNTs filled with atoms or molecules [33] and extended crystalline fillings [34], i.e. extreme nanowires. In the case of extreme nanowires, samples filled with Copper Halides [34], HgTe [5] and Silver Halides [35] have been studied. In all cases these studies have focused on the modification of the Raman scattering from the host SWCNTs due to the filling. For instance changes in the G-mode of filled tubes due to doping effects [36, 37, 38, 39] and changes in the RBM frequency which were explained in terms of mechanical effects [3, 35].
Despite the abundance of research on nanowires with lower dimensionality, there has been little to no direct studies on extreme nanowire systems. Such studies are useful as technology is fast approaching the fundamental limits of miniaturisation. This thesis reports, for the first time, on the effects of extreme reduced dimensionality on a novel nanowire embedded within a tube. Highlighting the new physics on such structures and the importance of cryogenic Raman spectroscopy studies on nanowires at this scale.

1.1 Thesis Content

This thesis reports on the Raman spectroscopy experiments performed on an ensemble of HgTe filled SWCNTs, using resonance Raman spectroscopy to quantify the observed features and probe the electronic transitions of this novel structure. It sets out the strong evidence for why the Raman features observed can be attributed to the tubular 2 atom diameter HgTe extreme nanowires and includes a discussion on DFT calculations of the vibrational and optical properties expected that were performed by collaborators (Eric Faulques). This work also discusses the significant experimental effort gone into ensuring that the RRS experiments were highly repeatable, to accurately determine optical transitions of the extreme nanowire structure. Finally, this thesis presents temperature dependant resonance Raman spectra in order to understand an unexpected temperature effect on the Raman scattering rate. The results, coupled the theoretical interpretation of various models allows for a much better understanding to the nature of the optical transition responsible for the Raman resonances and in particular to probe its coherent lifetime. This work has led to two publications[1, 8], which to best knowledge is the first time that the Raman spectrum due to a 2 atom nanowires have been measured.

1.2 Review

This section presents a detailed review of the literature surrounding this PhD. Including, but not limited to, a review surrounding Raman and its applications to carbon nanotubes, modifying the electronic properties of nanotubes by filling, as well as an investigation

into the other practical techniques used to probe nanoscale structures explaining why Raman is the focus of this thesis.

1.2.1 Carbon Nanotubes

Microtubules of graphitic carbon were first discovered in 1991 [40], where the group produced for the first time multiwalled carbon nanotubes (MWCNTs). Two years later the same group (and simultaneously another) synthesised SWCNTs by the arc discharge method [41, 42]. Since then many thousands of papers have been published on the topic [43], from fundamental studies on the electronic structure [44, 45, 46, 47] to investigation of their physical and mechanical properties[48, 49]. These fundamental studies resulted numerous publications on an array of applications. For example potential transistors [50, 51, 52], which can be suspended to reveal further information about the band structure [53] and even exhibit ballistic transport with zero Schottky barriers [54]. In addition the high Q-factor for such materials has interesting applications for MEMs devices [55, 56]. There has also been an array of works with medical applications of SWCNTs in targeted drug delivery [57, 58] which further highlights their wide interest and range of applications.
Single walled carbon nanotubes (SWCNTs) with diameters in the 1nm range are close to 1D structures, which has led to the discovery of a range of new physics [13, 59]. Despite their small diameters SWCNTs are still in many ways far from the limit of the smallest possible quantum wires, e.g. atomic chains. For instance, their band-structure can be fairly accurately derived from the band-structure of graphene using an envelope approximation based calculation [60]. The combination of strong quantum confinement, charge transport, reduced screening and constrained scattering leads to effects such as Luttinger liquids [61], long distance ballistic electron transport [62], and excitonic states in metallic systems [15] amongst many other unique effects. One common theme within these effects is greater coherence of electronic excitations.

1.2.1.1 Filling Carbon Nanotubes

Some years after the discovery of carbon nanotubes there was work published by Jeremy Sloan on the opening and filling of their internal channels of SWCNTs [63] through wet chemistry techniques. This led to some immediate incorporations of nanotubes with filling materials of C60 [64] and $RuCl_3$ [63]. Subsequently the technique has led to many other papers on the filling of SWCNTs with Jeremy Sloan being a notable contributor to the field. In fact to date there are over 100 published studies on the topic [3]. One of the most versatile and successful methods for producing extreme nanowires with diameters in the range 1-3 atoms is filling the central pore of single walled carbon nanotubes (SWCNTs) through melt infiltration[21]. As previously mentioned many different types of material have been encapsulated within a tube, each posing unique challenges to

achieve the goal. The most challenging is the encapsulation of atoms, which has been achieved with few elements such as metals [65, 22, 23, 24, 25]. Semiconductors, e.g. S [26], Te [27] and Se [28, 29] and insulators, e.g CsI [30]. Other common filling materials include a whole array of molecules, e.g. I_2 chains [66, 67] and most commonly Fullerenes with materials encapsulated within the cages [64, 68, 69, 70]. The most abundant of all the filling materials incorporated into SWCNTs channels are chemical compounds and attract a lot of interest because 1) the number of compounds suitable for filling is much greater and 2) they provide a wide range of physical and chemical properties for various applications. It has been reported in some cases that such filling forms extended nanowires or nanocrystals inside the nanotube channel, for example Ag halides [71, 35] and Chalcogenides [72], just to name a few. Metal Halides form the biggest group of chemical compounds used to fill nanotubes forming nanowires, with filling materials such as; SnF_2 [73], CuBr[74] and SnTe[75]. Overall, it is clear there is a great deal of interest in modifying SWCNTs in this way, and a whole host of materials available which exhibit new physics. If desired an extensive review of all of the filling types incorporated into SWCNTs can be found in the review paper by M. Kharlamova [3].

From the wide array of filling materials available it has led to the observation of new physics in these structures, and effects on the host tubes. It has been reported in a work by Li et al. [76] that filling SWCNTs with $MnTe_2$ causes a bandgap narrowing of the E^s_{11} and E^s_{22} transitions in the tubes due to modification of the bonding orbitals. In another report by Corio et al. [77] the authors filled SWCNTs with Ag and CrO_3 and characterised the sample with resonance Raman spectroscopy. They observed a charge-transfer effect where they noticed reduction of the tubes for Ag@SWCNTs and oxidation for CrO_3@SWCNTs. This was understood due to the observation of shifts in the G-band of the SWCNTs. Nanotubes filled with CuI causes changes to the G-band in the Raman spectra, which was ascribed to the shift of electronic band structure of filled SWNTs and transition of the metallic tubes to a semiconducting state[78]. This effect of tubes altering their type has been observed in many other types of filling an in general can be understood in terms of charge transfer effects where the filling material acts as either a donor or acceptor [79, 24, 35]. Despite the numerous publications reporting changes to the electronic structure of the host tubes, there are additional reports that do not observe any clear changes. For example in a work by Yashina et al. [75] the authors report on a novel crystalline filling of SnTe within a nanotube, however through the Raman spectra, they observe no obvious changes in the nanotube features, implying there is no interaction between the crystal and the host tube.

SWCNTs have a number of key advantages as templates; they protect the nanowires from oxidation and other chemical damage; they are atomically smooth; and they are electron transparent making full TEM characterisation of the extreme nanowires relatively easy (figure 1.1). Whilst they have some disadvantages, such as their polydispersity and the high fraction of metallic tubes, which may limit the practical applications of filled tube extreme nanowires, they are ideal as a pathfinder system for exploring extreme nanowire

physics. This has led to a range of publications on these materials. By far the majority of these publications cover the production and TEM characterization of filled SWCNTs. There are a few publications which focus on the physical properties [80, 81, 37, 82] and possible applications [83] however there is a real need for more research on the physics of these materials.

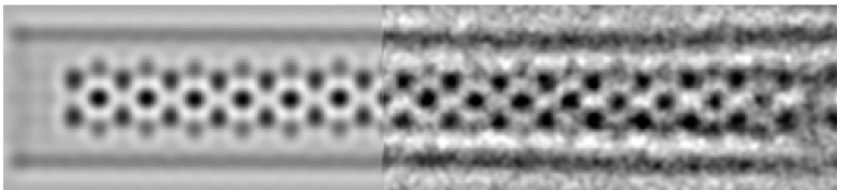

Figure 1.1: HRTEM image of HgTe embedded down the central pore of a SWCNT. Left panel is an image simulation based on a novel trial HgTe structure and shows a good match to observed crystal (Image adapted from [1])

Like with the array of potential applications SWCNTs has, filled SWCNTs possess an equally large scale field of potential applications. The possibility of encapsulating substances with a wide range of chemical and physical properties within SWCNTs channels opens up many possibilities. One of the most promising technological applications is in nanoelectronic devices [84, 85], where it was demonstrated that $Gd@C_{82}$ filled SWCNTs narrows the bandgap of the host tube, which can be utilised as channels with ambipolar conduction. Other works [86] report on the temperature dependence on the conduction of filled SWCNTs showing a change from p-type to n-type. Finally metal-filled carbon nanotubes represent a class of hybrid carbon-based nanostructures with a wide range of applications in various fields, from nanoelectronics and spintronics [87] to nanomedicine [88]. Overall, whilst there is a significant amount of work on the changes to the host tube, and charge transfer effects, there has been no reported work on new Raman modes of extended crystalline filling materials within the nanotubes. With the supporting literature, this opens up a new potential for the direction of this thesis to provide the first in depth study of Raman modes of a novel filling material within nanotubes.

1.2.2 Probing Filled SWCNTs

This section will discuss the various experimental techniques used to probe carbon nanotubes and the internal filling structure highlighting the advantages and limitations of each, which will aim to elucidate as to why Raman is the key characterisation tool used in this thesis.

By far the most rigorous and thorough method of characterisation of any nanotube sample is direct observation of the structure through high-resolution transmission electron microscopy (HRTEM/TEM)[89]. This form of microscopy has been extensively applied

to nanotubes and low dimensional crystal structures [90, 29], and can be used to determine the filling quotient of a sample of filled tubes and observation of the crystal structures that are formed and even in some cases used to directly observe phase-change behaviour [91]. The main disadvantage of TEM imaging, is that is generally a destructive characterisation technique and does not directly yield information about the electronic properties of the sample. With this in mind, TEM imaging is best suited to complement other characterisation techniques in this field and vice-versa.

In terms of determining the optical transition energies of extreme nanowire materials, UV-VIS-NIR absorption spectroscopy [92, 79] is by far simpler, and again can be used to determine optical and electronic properties of the host tube [93] by themselves, or through chemical/electrochemical doping [94]. Absorption spectra of SWCNTs show characteristic peaks in an energy range from 0.5 to 3 eV, which corresponds to the electronic transitions in the joint density of states of the various types of tubes. Changes in the absorption spectra of SWCNTs may reflect changes in the electronic properties of SWCNTs, which might occur due to filling tubes. Depending on the filling compound some literature reports on the decrease [95] or increase [96] of the optical absorption spectra of the first vHs in semiconducting SWCNTs. From these observations is was concluded that charge transfer occurs in filled nanotubes, although the direction of charge movement cannot be determined by the absorption spectra. However, in ensembles of SWCNTs it is not possible to separate which features are associated with particular extreme nanowire structures. It is likely that individualising nanotubes through various techniques such as density gradient ultra-centrifugation [97] can overcome this limitation. However, whilst this technique has been applied to unfilled nanotubes, there's little work performed on individualisation of extreme nanowires embedded within tubes.

Photoluminescence excitation spectroscopy (PLE) [98] is a technique which can be used to assign the optical features to particular structures [99]. It can also be used to study the effects of surfactant wrapping on the nanotubes due to strain[100]. This is useful to understand as SDS wrapping is a common technique used to individualise nanotubes, however was reported to not be stable at low temperature. PLE spectroscopy can be used to produce a 2 dimensional map of the PLE intensity on the wavelengths exciting the sample and the emitted radiation, which can be used to compare between pristine and modified nanotubes. However, this technique has a number of drawbacks, again it generally requires individualisation of samples to work best, and won't allow observation of metallic nanotube samples.

With this in mind, and in terms of equipment it is only slightly less complicated to perform than RRS. In terms of the vibrational modes observed, the only other alternative to Raman is infra-red spectroscopy (IR), however as apparent through the selection rules, it is likely IR spectroscopy will probe different vibrational modes that are not observable through Raman.

Overall, it is apparent there is an abundance of other techniques that can be used to probe nanotubes, and whilst some are easier to perform than others, it is not clear that there

is a single technique that can match RRS alone. In fact Raman spectroscopy appears to provide a rich amount of information on the host tube and filling compound, without the need to mono-dispersed samples and is non-destructive in nature. Whilst many of these techniques clearly compliment each other, the most obvious match for Raman in terms of additional information is HRTEM for the ability to couple with modelling techniques and assign the vibrational modes observed in Raman to the crystal structure.

1.2.3 Raman Spectroscopy of Filled Carbon Nanotubes

Since the first reports of filling carbon nanotubes [63] numerous studies have utilised Raman as a characterisation tool to probe the tube/filling material. Up to 2013 there have been around 19 studies on various filling compounds and the effects on the SWCNTs all using Raman spectroscopy or in some cases Raman spectroelectrochemical gating[34, 35]. A more general review on filled nanotube experiments and characterisation can be found in a 2013 review paper by M. Kharlamova [3]. This section discusses the scope of Raman studies on filled nanotubes.

In a study by Kharlamova in 2013 [101]. The author used melt infiltration to incorporate tubes with Zn, Cd and Tb chlorides and demonstrated through Raman (with optical absorption and XPS) that all these salts lead to charge transfer from the nanotube wall to the filling compound. The study showed clear changes to the G-band which upshifted by $\sim$7-15cm^{-1}. The origin of this shift is connected with a change in the C-C bond energy and the electronic structure of the SWCNTs. This is not an unprecedented effect, in fact, a number of studies observe changes to the electronic structure of nanotubes through Raman spectroscopy and understand the effect due to charge transfer either to or from the tube depending on whether the incorporated material acts as a donor or acceptor.

In a study by Corio et al. [102], the authors performed RS (Raman spectroscopy) on CrO_3 and Ag filled SWCNTs. They showed due to changes in the G-band of the Raman that charge transfer occurred between the filling material and host tube changing the electronic properties of the tube through oxidation or reduction. In both samples investigated they demonstrated that the filling compounds either acts as a donor (Ag) or acceptor (CrO_3) altering the electronic structure of the nanotubes. A 2007 study by Chernysheva et al. [78] report on capillary filling nanotubes with CuI nanocrystals. In this work they demonstrate clear changes to the G-band features upon impregnation of the filling material. Observing a broadening of the G-modes and shifts to lower frequencies, with the G$^-$-line of metallic tubes disappearing. This is ascribed to changes in the electronic structure through doping causing the tube to change from a metallic like state to semiconducting. These reports form a picture of the effects of filling on the nanotube modes and can be summarised as the filling material acting as a donor or acceptor to the nanotube characterised by changes in the G-band from the Raman. This is further supported by other experiments on filled tubes. For example incorporating nanotubes with Cu [24, 25], halides of Cu [74, 34] and Ag [35] show evidence of charge transfer to the

tubes. Whilst incorporating tubes with CuI [78, 103], Chalcogenides (S, Se and Te)[29], SnF_2 [73] and various metal Halides including; Ag[35], Fe[104, 36],Ni[37],Mn[105] and Co[106, 36], all demonstrate charge transfer from the tube.

There are also reports[35, 34] on utilising Raman spectroelectrochemical techniques to not only measure the change from metallic or semiconducting tube type by changes to the G-band Raman, but also tune the Fermi energy of the system by electrochemical gating observed through shifts in the resonance. Whilst the technique has not been used on filled tubes as much as unfilled tubes [107, 108, 109, 110]. The reports suggest it could be a powerful technique for controlling and altering the band structure of filled carbon nanotubes which has interesting applications for tunable electronics.

Observation of effects on filled tubes is not limited to inorganic materials, in a 2003 work by Takenobu et al. [95], the authors report on the incorporation of organic molecules in SWCNTs and their potential applications in molecular electronics. In this study the authors report on changes in the G-band indicative of n- or p-type doping of the host tube and being able to tune the Fermi energy near the Van Hove singularity of the underlying optical transitions. Recently (2015) in a study by Gaufrés et al.[111] the authors filled nanotube samples with an array of dyes (α-sexithiophene and β-carotene) and functionalised the nanotubes. In this report they demonstrate a giant increase in the resonant Raman scattering rate of the dyes, free from fluorescence and photo-bleaching. This work did not report on any changes to the Raman active modes in the nanotubes, but the notable increase in the dye Raman scattering rate gives many potential interesting applications in multiple nanoprobe labels which could give better spectral resolution than fluorescence imaging. Whilst this work is not relevant to semiconductor filled nanotubes, it does highlight the wider interest in filled nanotubes and its potential applications, as well as unexpected effects arising from filled nanotubes.

In another recent (2014) work by Li et al. [112], the authors report on the encapsulation of sulphur chains inside SWCNTs. In this study they report on the appearance of new Raman peaks originating from the confined sulphur species, whilst simultaneously observing a decrease in intensity of the higher frequency nanotube modes and a red-shift of one of the near-IR electronic transitions of the nanotube by $\sim$10%. They suggest in this study the new Raman modes in the S@SWCNT originate from strong coupling between the SWCNT excitons and the sulphur-sulphur vibrations. This report to date is the only work (despite this thesis and its associated publications [1, 8]) that details new Raman modes appearing in nanotubes due to a filling material. Even in ref [112] it is not reported that these modes are due to a novel structure of the filling material but instead due to tube-filling material interactions.

Whilst it is clear an array of organic [113, 111] and inorganic materials have been incorporated into tubes no work has reported directly on the Raman resonances of extended nanocrystalline structures within the tube. All studies to date reflect changes to the tube type and pose for interesting applications with tunable electronics by gating and filling tubes. However, it does appear there is a huge gap in the field for extensive studies on

the filling materials themselves through resonance Raman spectroscopy.

Chapter 2

Theoretical Background

This chapter will detail the various theoretical background concepts needed to understand the work in this thesis. If required an extensive review of Raman scattering in carbon nanotubes can be found in refs [13, 114]. Whilst this thesis focuses on novel 1D nanowires, we will begin our background understanding by focusing on one of the most well-understood 1D materials, namely single-walled carbon nanotubes. Whilst the physics of the most extreme nanowires, namely atomic chains is still a relatively new and emerging field, revealing new physics, it seems likely that some of the physics will be shared with the nanotube counter-parts. This chapter begins by setting out the notation used to describe the structure of a carbon nanotube, and how it is formed by a graphene sheet. We then move onto the electronic and vibrational properties of 1D carbon nanotubes and develop into the physics of 1D materials in general. The theoretical aspects of Raman spectroscopy is detailed, including the fundamentals of Raman and resonance Raman then moving onto the Raman features observed in 1D materials, explaining why resonance Raman is a useful tool for probing these structures.

2.1 Single-Walled Carbon Nanotube Structure

This section provides an introduction to the structure and properties of single-walled carbon nanotubes describing their 1D attributes and the evolution of the structure from a 2D graphene sheet. A SWCNT can be described as a hollow cylinder, made up from a single layer of a graphite crystal rolled up into a cylinder [2, 13, 115, 116]. This tubular structure, 1 atom thick usually has an extremely high aspect ratio ($\sim 10^5$) [114, 3] and it is this elongated structure, coupled with the large van der Waals forces that form tightly bound bundles of tubes [3, 117]. Disregarding the length, a SWCNT can be described by its chiral vector, $\vec{C}$, along which the graphene sheet is rolled, therefore this vector represents the circumference of the nanotube. This vector is usually denoted by a pair

of indices (n,m) that describe the number of unit vectors $\vec{a}_1$ and $\vec{a}_2$ of the 2D graphene lattice, as seen in equation 2.1

$$\vec{C} = n\vec{a}_1 + m\vec{a}_2. \tag{2.1}$$

This (n,m) assignment is useful as it qualitatively defines the properties of a SWCNT, these are described as armchair (n=m), zigzag (m=0) or chiral structures [3, 115, 118]. These can again be used to determine physical properties about the tube such as diameter and type of tube, for example; if n=m the tube is metallic, if n-m is a multiple of 3, then the tube is semiconducting with a small bandgap, other wise the tube is a wide bandgap semiconductor [115, 47, 119, 45]. Figure 2.1 visually shows the chiral vector and how a carbon nanotube can be made through the projection of a 2D graphene sheet.

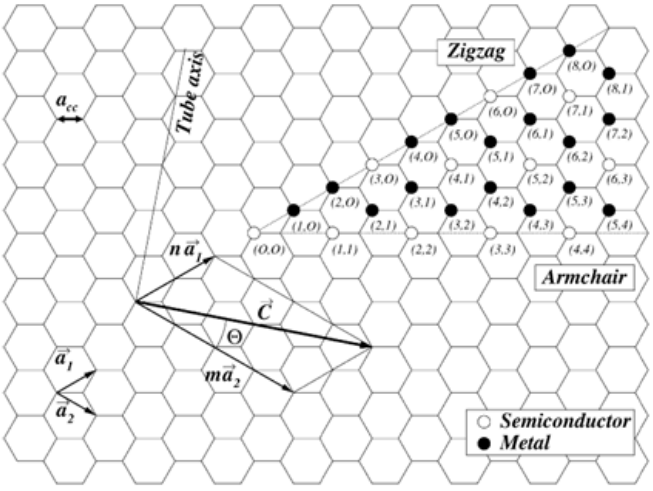

Figure 2.1: Projection of an unrolled carbon nanotube on a graphene sheet showing the chiral vector, $\vec{C}$, the tube axis vector and chiral angle along with unit vectors. Also depicted are various possible folding axis and the resultant (n,m) index and resultant tube type. Image adapted from [2].

The chiral vector, $\vec{C}$, as already discussed represents the circumference of the nanotube and is the vector running perpendicular to the nanotube axis, in terms of (n,m) assignment it can be therefore shown that the nanotube diameter d_t is given by;

$$d_t = \frac{C}{\pi} = \sqrt{3}a_{C-C}(m^2 + mn + n^2) \tag{2.2}$$

where a_{C-C} is the carbon-carbon bond length (~0.142nm) and C is the magnitude of the chiral vector.

The level of detail on the structure of SWCNTs discussed here is sufficient for a basic understanding of SWCNT structure and to understand other concepts discussed in this thesis. For a more rigorous review on the structure of SWCNTs and the types of tubes formed through graphene folding, there is a breadth of additional information about nanotube structure discussed in other works such as "Physics of Carbon Nanotubes" [13] or Carbon Nanotubes: Properties and Applications [2].

2.2 Electronic Structure and Properties of SWCNTs

The previous section demonstrated the atomic structure of a carbon nanotube is similar to that of graphene. This section discusses the electronic structure of carbon nanotubes, and how a good approximation can be obtained from the band structure of graphene through Brillouin zone-folding. The discussion of the zone-folding, and how quantum confinement of the electronic wave function around the circumference of the nanotube will also help in understanding the theoretical aspects of general 1D physics in the extreme nanowires.

2.2.1 Electronic Structure of Graphene Sheet

To first order the electronic structure of carbon nanotubes can be derived from the 2D parent material graphene [13, 118, 47]. The graphene unit cell (figure 2.2 left) contains two sp^2 hybridised carbon atoms, each atom has four valence electrons. Three of these form covalent σ-bonds, in-plane with the graphene sheet, whereas the fourth electron forms the weaker, delocalised π-bond which is outside the graphene sheet [114, 120] and is the reason for the weak interaction between bundled nanotubes [45]. Since the energy levels of the σ-bonds are far away from the Fermi energy (E_f) they do not play a role in the electronic properties of graphene. On the other hand, the π-electrons are close to the Fermi energy be optically excited from the valence to conduction band. The first

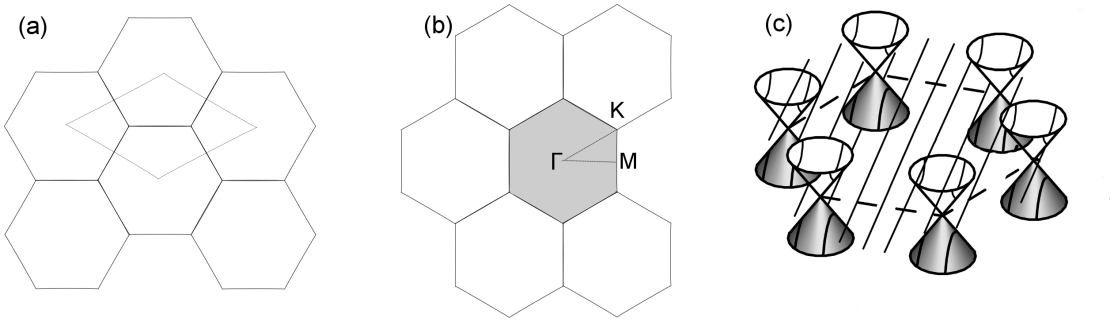

Figure 2.2: Honeycomb lattice of graphene (a) with graphene unit cell (dotted rhombus) containing 2 carbon atoms. First Brillouin zone (b) coloured in grey showing ΓKM, points of high symmetry. Depicted in (c) is the cone shaped conduction and valence bands at the 6 K-points of the first Brillouin zone at the Fermi level (adapted from [3]).

Brillouin zone of graphene (figure 2.2 b) has 3 points of high symmetry (Γ, M and K) which are important when understanding the dispersion relation of graphene, and when considering phonons in carbon materials. The optical transitions occur where the valence (π) and conduction ($\pi\star$) band touch (figur 2.2 c), the dispersion relation is linear around this K point yielding the unique electronic properties of graphene and SWCNTs. The formula for the energy dispersion relation can be derived using the tight-binding model [118], where the model assumes the π electrons are tightly bound to the carbon atoms

and the wavefunction of π electrons can be written as a linear combination of atomic orbitals (LCAO) as a Bloch wave. It predicts the following dispersion relation, E(k), for graphene [118]

$$E(k) = \frac{\pm\gamma_0\omega(k)}{1 \mp \gamma_1\omega(k)} \tag{2.3}$$

where γ_0 and γ_1 are parameters resulting from fitting to experimental observations and the + and - signs come from the antibonding $\pi\star$ and the bonding π bands respectively. The function ω(k) can be written out as;

$$\omega(k) = \sqrt{1 + 4cos\left(\frac{\sqrt{3}k_x a}{2}\right) cos\left(\frac{k_y a}{2}\right) + 4cos^2\left(\frac{k_y a}{2}\right)}, \tag{2.4}$$

where a is the carbon-carbon bond length (∼0.142nm). When looking at the band structure of graphene it can be seen that the π and $\pi\star$ touches at the 6 K-points at the Fermi energy, and a maxima and minima of the two bands can be found at the Γ-point. It is due to the touching bands at the K-points that graphene is considered to be a zero band gap semiconductor [120, 121].

2.2.2 Electronic Structure of SWCNTs

The local structure of SWCNTs is similar to that of graphene, however, the boundary conditions imposed on the structures are going to be different. The unit cell of a SWCNT is much larger than that of graphene, and in SWCNTs they can be regarded as infinite only in the direction they are extended. To understand the differences between graphene and SWCNTs, we will first begin with the electron wavefunctions of graphene. As stated the wavefunction of graphene can be written as a Bloch wave [122] of the form;

$$\psi(\vec{R}) = e^{i\vec{k}\cdot\vec{R}}u(\vec{R}), \tag{2.5}$$

where k is the electron wavevector and $u(\vec{R})$ is a positional function with the periodicity of the graphene lattice. In general with the models for SWCNTs the curvature of the tube is ignored, however, because of the seamless nature of the folded graphene sheet the electron wavefunctions will have a periodic boundary condition in the circumferential direction, which requires their wavevectors $\vec{k}$ to satisfy;

$$\vec{k}\cdot\vec{C} = 2N\pi, \tag{2.6}$$

where N=1,2,3.... This set of allowed wavectors form a set of N parallel cutting lines in the Brillouin zone of the graphene lattice. These cutting lines can be superimposed across the energy dispersion of the first Brillouin zone [114, 123]. The orientation of these cutting lines depends on the chiral angle, and their spacing is inversely proportional to the diameter.

By superimposing the 1D cutting lines (figure 2.3 (a)) from the energy dispersion of the first Brillouin zone of graphene onto a 2D energy wave-vector surface (figure 2.3 (b)) it is possible to obtain the electronic band structure of the SWCNT. This application

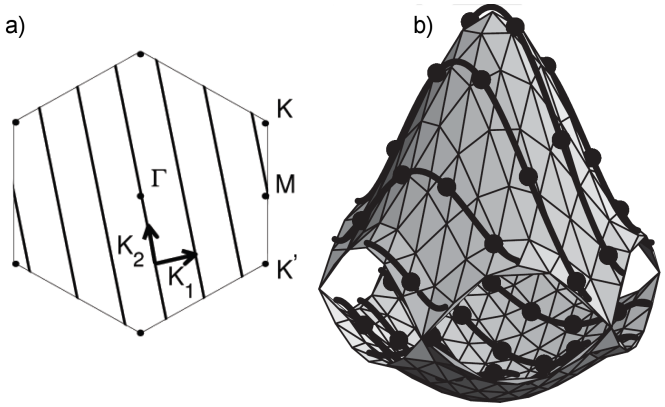

Figure 2.3: Figure (a) showing the cuttings lines of a nanotube in the 1^{st} Brillouin zone of graphene. Part (b) shows the superimposed cutting lines from (a) onto the calculated constant energy contours for the conduction and valence bands of a 2D graphene layer in the first Brillouin zone using the tight binding model. The black circles in the solid lines correspond to connection points to the edge of the Brillouin zone. Image adapted from [4].

of the tight-binding model seems a reasonable approximation based on experimental observation. However, the large curvature of small diameter nanotubes causes changes in the C-C bond length and requires more accurate methods for describing the electronic structure [124]. As can be seen from figure 2.3 (a), depending on the separation of the cutting lines, this can cause the line to intersect with the K-point of the Brillouin zone which will cause a tube to be metallic (if there is an intersection) or semiconducting otherwise. It is therefore useful to classify tubes to the following relation;

$$MOD(2n + m, 3) = 0, 1, 2 \tag{2.7}$$

or the modulo operation of the tube index. This is a useful relation as the value tells you where the nearest cutting line is. A remainder of zero denotes a metallic nanotube (the cutting line crosses the K-point), and a remainder of 1 or 2 denotes different types of semiconducting tubes. In reality, curvature effects in the 2D graphene sheet change the relative lengths of the C-C bonds parallel or perpendicular to the tubes axis. It has been found [3, 45] the aforementioned effect only has impact on MOD0 (armchair) nanotubes, creating small band gaps, however, this effect only applies to narrow diameter nanotubes. It is the translation of the 1D cutting lines onto the 2D energy bands and integrating along these lines that results in the electronic density of states for the band diagram [4, 3]. This is represented by figure 2.4, which shows the electronic density of states for a (5,5) nanotube (from [3]). It can be seen from figure 2.4 that when the energy dispersion passes through a local maxima/minima (i.e a turning point) there is a sharp peak (right hand of figure 2.4) at the turning points of the band structure in the density

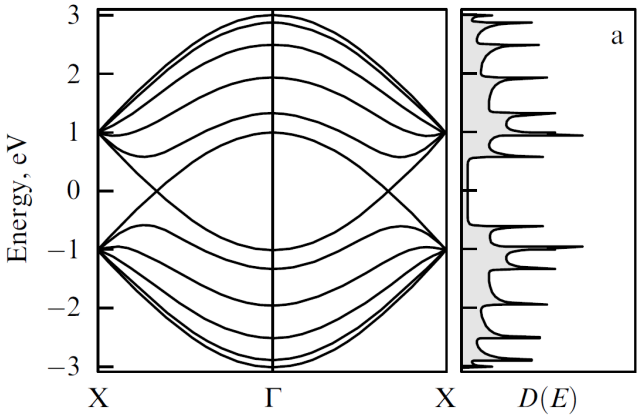

Figure 2.4: Band structure (left) and representative electron density of states for a (5,5) SWCNT. Image adapted from [3]

of states. These spikes in the DOS are referred to as van Hove singularities [32, 125] and physically, are where the cutting lines pass tangentially across an equal energy contour of the energy band structure of graphene. These singularities yield unique effects on the optical properties of SWCNTS, and other 1D systems [60, 126, 59, 99].

2.2.3 Optical Transitions

As previously mentioned, it is the spikes in the density of states that give SWCNTs their unique and interesting optical properties, this section will discuss further on the vHs, and the effects they have on the properties of tubes. These spikes in the density of states appear when the energy dispersion functions passes through a minima or maxima are responsible for the observed increase in the rate of emission (and absorption) in an optical process, due to an increased number of electronic states available [118, 13] and is the reason why it is possible to observe the optical response of individual carbon nanotubes using Raman spectroscopy [127, 60, 32].
Optical transitions can only occur between vHs singularities on the same cutting line, which allows for inter-band transitions between two vHs on the same cutting line close to the K-point. Due to this, it is often useful to label the energy difference between each vHs in the valence and conduction band, E_{ii}, where we can form what is called the joint density of states (JDOS)[128]. The vHs in the JDOS is often plotted as a function of the diameter of the tube as calculated by the tight-binding model and is referred to as the Kataura plot[60] shown in figure 2.5. It can be seen the Kataura plot forms distinct bands separated in energy which correspond to different optical transitions, which provide nanotubes with their unique optical properties for both absorption [129] and Raman spectroscopy. Interestingly, the equal energy contours about the K-point in the graphene band structure are not circular, but instead form a trigonally warped [130] shape with equal energy contours forming straight lines that connect the M-points in the graphene Brillouin-zone. This causes a shift in energy of the vHs in the DOS, depending

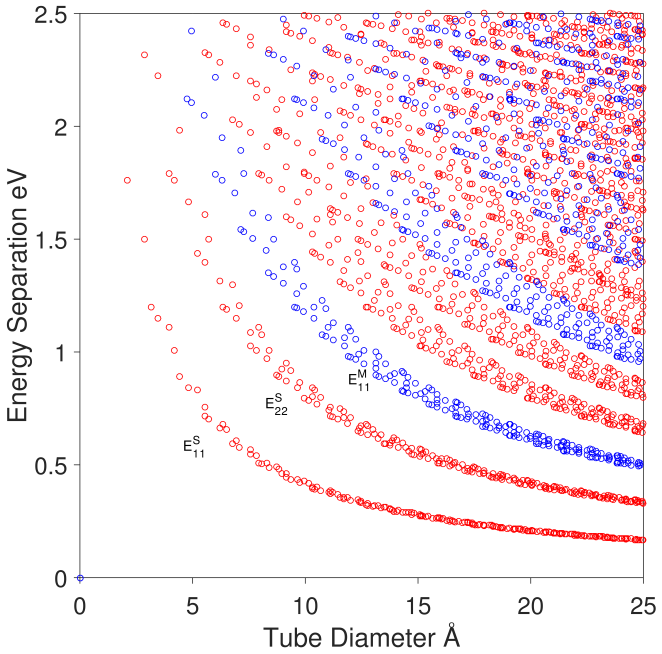

Figure 2.5: Kataura plot showing the transition energies of corresponding vHs from the JDOS as a function of nanotube diameter as calculated by the tight-binding model. Red open circles are represented by semiconducting SWCNTs, whilst blue open circles denote metallic SWCNTs, the first 2 transitions and the first transition for semiconducting and metallic tubes are labelled on the plot.

on where the cutting line is around the energy contour. This means that each (n,m) nanotube has a unique set of E_{ii}, and explains why the distinct bands in figure 2.5 widen with increasing energy.

Overall the SWCNT is an ideal quantum wire in which to discuss the physics of 1D materials, as it's 1D properties can be relatively easily predicted, and the measured properties agree well to the predicted properties [4]. Other quantum wires will likely exhibit similar physics to that of the nanotube when considering the electronic density of states of quantum wires follows a well-understood relationship [131].

2.3 Phonons

Phonons are the quantum of vibrational motion in a condensed matter system. Phonons play a huge role in the electronic and thermal properties of materials [132, 133]. There are two main types of phonon modes that appear in solids with more than one atom per unit cell. Acoustic phonons, which are displacements of atoms in the lattice from their equilibrium positions in phase with one another and in the low wave-vector regime can approximated as sound waves. The other is optical phonons, these are out-of-phase movements of atoms within the lattice, and can be excited optically. The physics of phonons in solid state systems is extensive [122] and plays a part in a huge amount of physics,

for example phonon interactions underpin superconductivity [134, 135]. The unit cell of graphene contains 2 carbon atoms and therefore has 6 degrees of freedom, resulting in 6 phonon branches [121]. In the same way that zone-folding of the 2D graphene electronic structure can be used to approximate the 1D SWCNT electronic structure. The 1D phonon structure of SWCNTs can be approximated from the 2D phonon dispersion of graphene [132]. Although these calculations ignore curvature effects, which in reality, lead to low-frequency twisting modes and the radial breathing mode (RBM) where the carbon atoms vibrate in the radial direction [13]. As reported in ref [132] the 1D phonon dispersions and vibrational DOS for a (4,2) nanotube were calculated, producing 90 distinct phonon branches, which is less than the expected number, due to a number of degenerate modes. From this it is clear there a significant number of vibrational modes in SWCNTs that can be investigated using spectroscopical techniques. However, through the selection rules, only a few of these will be active through Raman or IR and some are too weak to identify. The RBM feature is prominent in nanotubes and readily identified through Raman spectroscopy [4]. We will discuss the Raman effect and active modes in nanotubes in section 2.5.

2.3.1 Phonon Scattering in 1D Materials

The study of electron and phonon dynamics in materials is an extensive field, mainly because understanding carrier dynamics yields information about carrier transport properties and heat capacity amongst other physics that is of fundamental importance in semiconductor physics. In bulk semiconductors the role of electron-phonon, electron-electron and phonon-phonon interactions are generally well-understood and reported in a number of textbooks [136, 137]. However, in the case of 1D systems, such as SWCNTs and extreme nanowires, the confinement of electrons and phonons and the strong excitonic effects complicates the situation, which has led to some unusual new physics [14, 138, 139].

A common scattering event in materials, that is one of the main focuses of this thesis and measured by Raman spectroscopy, is electron-phonon scattering. Electron-phonon scattering (e-ph) is integral to understanding the inter and intra-valley scattering processes that occur in SWCNTs [140]. This scattering process is likely to be the limiting factor on the lifetime of the optical transitions investigated in this thesis, so it is likely that calculations of the coherence lifetime might also give an indication of the timescale of e-ph scattering events in SWCNTs and equivalent 1D materials.

2.4 Excitonic Effects

An exciton consists of an electron-hole pair that are bound to each other by Coulomb interactions. Excitons in bulk semiconductor materials usually have a binding energy on the order of meVs. In the case of nanotubes, because of the 1D properties, the electron-hole attraction becomes much stronger i.e on the order of electron volts. Furthermore excitons have been observed in metallic tubes, due to reduced screening effects [141]. Due to the narrow diameters and increased electrostatic interaction, this often leads to strong excitonic effects in SWCNTs, which have impact on the optical properties of tubes [14, 139]. In fact it was reported by Wang et al. that excitons [141] are responsible for the unique optical properties of SWCNTs rather than the presence of van Hove singularities in the joint density of states. The experimental evidence supporting the excitonic nature of the optical transitions originate from nonlinear two-photon absorption experiments. In this experiment, SWCNTs are excited in a two-photon process and light is observed around the energy of the first transitions. If the E_{11} transition was due to the creation of an exciton, the energy of two-photon absorption would be observed at a higher energy than E_{11}, which was observed experimentally[141, 139]. Other experiments have subsequently been performed lending support for the excitonic picture. For example, it has been shown by I. Mortimer and R. Nicholas that the PL efficiency of SWCNTs has a temperatures dependence due to bright and dark excitons in nanotubes. [142].

2.5 Raman Spectroscopy

Raman spectroscopy is a powerful spectroscopic technique allowing observation of vibrational, rotational and other low-frequency modes in an atomic system [143]. The technique is widely used as a characterisation tool as molecules and such systems possess a unique Raman finger print. It is because of this versatility that Raman spectroscopy has been applied to a wide range of problems within science [144]. In molecular systems it is used to complement IR spectroscopy for determining vibrational spectra and also used to determine composition of materials. It has been widely exploited in the field of solid state physics to understand the physics of crystalline systems, this is highlighted by the fact the Light Scattering in Solids series [137] of books extends to nine volumes. This section explains the physics behind the Raman effect, moving onto resonance Raman scattering and applying the technique to 1D materials of those studied in this thesis.

2.5.1 The Raman Effect

Raman scattering is a very weak optical process, in comparison to its counterpart, Rayleigh scattering. Raman scattering is the inelastic scattering of a photon that can

involve many processes and excitations. In this study we are only interested in the processes which involve phonons [132]. For extra clarity and details of the Raman effect, a detailed review can be found in various sources [145] [146]. Most photons are elastically scattered, meaning that the scattered photon has the same energy as the incident photon, some photons are inelastically scattered, meaning the scattered photon has a different energy from the incident. For single phonon Raman scattering in a solid state system the dominant process involves sequential absorption of a photon creating an electronic excitation of the system, scattering of this electronic excitation by a phonon to generate a second electronic excitation, and then emission of a photon and destruction of the second electronic excitation. A common way to represent Raman processes is through Feynman diagram formalism [147] seen in figure 2.6, which presents the simplest 1-phonon emission process. The shift in energy of the scattered photon is called the Raman shift, and is commonly measured in wavenumbers (cm^{-1}), this unit is relative to the photon causing the excitation. Detecting emitted photons reveals information about the energy of the phonons and thus information on the structure and composition of the atom or molecule. As stated this is a weak process, where only about 1 in 10^7 photons are inelastically scattered, this stresses the need for sensitive experimental equipment to detect the Raman. The figure 2.6 depicts a typical Stoke's shifted Raman scattering event. Alternatively, it is possible the excitation can absorb a phonon through an intermediate state and hence the emitted photon is of higher energy than the incident, in this case the emitted photon is referred to as anti-Stoke's shifted. Using Raman spectroscopy and measuring the Stoke's and anti-Stoke's Raman modes, it is possible to determine further information about the sample probed, for example the temperature [114, 148, 149].

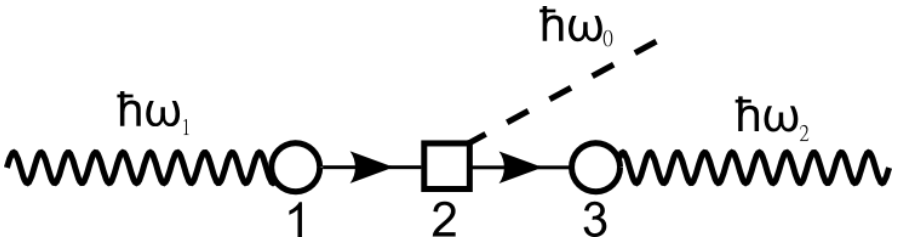

Figure 2.6: Feynman diagram of a typical 1 phonon Stoke's Raman process. The incident photon ($\hbar\omega_1$) creates and electron-hole excitation at vertex 1. This excitation then propagates and scatters by the emission of a phonon ($\hbar\omega_0$) at vertex 2, to a second electron-hole excitation, which propagates until it decays emitting a photon ($\hbar\omega_2$) at vertex 3.

The processes underlying Raman scattering and resonance effects are basically well understood, even if it is not trivial, and sometimes not possible, to quantitatively predict the strength and dispersion of Raman spectra [150, 137]. Due to the weak interactions involved, time-dependent perturbation theory can be used to model Raman scattering successfully [137]. The theory gives rise to the standard formula for the intensity of

Raman scattering;

$$|\sum_{n,m} \frac{\langle 0|\,\hat{H}_{exc}\,|n\rangle\,\langle n|\,\hat{H}_{phonon}\,|m\rangle\,\langle m|\,\hat{H}_{scat}\,|0\rangle}{(E_l - E_n - i\Gamma_n)\,(E_l - E_{ph} - E_m - i\Gamma_m)}\,|^2 \tag{2.8}$$

where $|n\rangle$ and $|m\rangle$ are first and second electronic excitations with complex energies $E_n - i\Gamma_n$ and $E_m - i\Gamma_m$, and $\hat{H}_{exc}$ and $\hat{H}_{scat}$ are dipole interaction Hamiltonians for the excitation and scattered light and $\hat{H}_{phonon}$ is the phonon interaction Hamiltonian. E_{ph} is the energy of the scattered phonon. In the simple case of a single discrete, optically active electronic excitation the denominator leads to resonances when the incoming and outgoing photon energies are equal to the energy of the electronic excitation. In the limit that $E_{ph} \gg \Gamma$ this leads to two distinct resonances whose scattering intensity is proportional to Γ^{-2}. In the limit that $E_{ph} \ll \Gamma$ this leads to one resonance whose scattering intensity is proportional to Γ^{-4}. In both cases the dependence on the scattering rate is due to the coherent nature of Raman scattering [137]. In real solid state systems it is likely that the electronic excitations will not be discrete but form a continuum. The theory of Raman can become more complicated with the possibility of interference effects and multiphonon Raman scattering. The level detailed here is enough to understand the main concepts in this thesis, later on in the thesis we will explore the details of eq 2.8 and the complications of multiphonon Raman scattering and lifetime effects.

2.5.2 Resonance Raman Scattering

In the previous section it was mentioned that the possibility of resonances exist. During a Raman scattering process, when any of the intermediate states are real electronic transitions, the rate of Raman scattering is greatly increased [137]. This effect, resonance Raman scattering (RRS) is of use for not only increasing relative signal of Raman peaks when compared to non-resonant Raman scattering, but also yields information about the electronic structure of the sample. For a 1 phonon process, there are two resonance conditions for these optical transitions: 1) the resonance is with the incident laser energy and 2) the resonance is with the scattered photon. These two cases can be described by;

$$\begin{aligned} E_L &= \Delta E \quad \text{(incident resonance)}, \\ E_L &= \Delta E + \hbar\omega \quad \text{(outgoing resonance)}, \end{aligned} \tag{2.9}$$

where E_L is the incident laser excitation energy, ΔE is the energy gap between the initial and excited electronic states and $\hbar\omega$ is the energy of the phonon involved in the scattering.

In the case of carbon nanotubes, the ΔE represents the allowed transition energies between the van Hove singularities. It is these van Hove singularities in the joint density of states (JDOS) that contribute to the enhancement of the Raman intensity, to the point that when the energy of the laser is the same as the vHs energy in the JDOS, it is

possible to observe Raman modes from individual tubes; isolated or in the presence of other (n,m) conformations [114].

2.5.3 Raman Scattering in 1D Materials

In addition to resonance effects observed in 1D materials because of the van Hove singularities, other effects can lead to an enhancement of the optical processes. For example, with incident light polarised perpendicular to the long axis of a 1D material, the transitions are suppressed due to depolarisation effects. It is possible to show that for a group of randomly orientated, non-interacting tube the relative Raman intensity changes as a function of input electric field angle (θ) as;

$$1 + \frac{1}{2}cos(2\theta), \tag{2.10}$$

where two input polarisations perpendicular to one another would lead to a relative signal of $\frac{3}{2} \rightarrow \frac{1}{2}$, yielding a 3:1 suppression of the signal between two orthogonal polarisations. This effect can be understood with the following example; if the nanotube was parallel to the electric field, the re-radiated field would be in the direction of the tube orientation. If the nanotube was perpendicular to field, the emitted radiation would be massively suppressed due to depolarisation effects. If the tube were at 45° to the incident field then the radiated electric field would have a component vertical and horizontal. In the case of many randomly orientated tubes this leads to the 3:1 ratio stated earlier. This will become important in chapter 4 where we investigate the polarisation dependence on the Raman intensity.
Resonance Raman scattering is commonly used to increase the relative amount of weak Raman scattered light modes in a sample of interest. In the case of nanotubes, there is a large density of states at singular transition energies due to a combination of strong excitonic effects and Van Hove singularities. In this circumstance RRS not useful, but integral in probing the electronic transitions in these structures, as if the excitation energy does not match the transition there will be little or no signal. This is why RRS studies are important on SWCNTs and other 1D structures in order to first determine the fundamental optical transitions in the material.

2.5.4 Raman Active Modes from Carbon Nanotubes

The extreme nanowires studied in this thesis are embedded within the central pore of SWCNTs, it is therefore important to understand the Raman features that appear in the host tube. Both in terms of their representative Raman spectra, to ensure observed Raman features are correctly assigned, and to explain the physics of phonons observed in well-understood 1D systems. A representative Raman spectra of unfilled nanotubes

taken at 1.766eV can be seen in figure 2.7, which presents the RBM, D-band and G-band, which will now be explained.

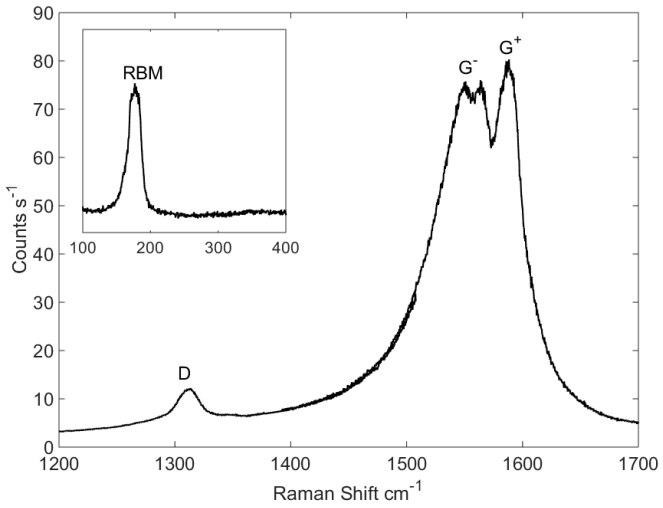

Figure 2.7: Representative Raman spectra of bulk unfilled SWCNTs deposited onto Si/SiO_2 substrate, acquired using an excitation energy of 1.766eV. Inset shows the RBM region of the spectra.

Since the electronic structure of SWCNTs is derived from that of the 2D graphene sheet, it is clear that the Raman features observed in SWCNTs would be similar to that of graphene [114, 151]. The Raman active modes in SWCNTs can be first or second order, and yield information about the type and properties of the tube. First order Raman scattering involves a single phonon (figure 2.6). For an electron to recombine with a hole, the scattered state must not differ by more than two times the photon wave vector, this conservation rule, coupled with the small wave vector photon is the reason that zone-centre, (Γ-point) phonons are observed in solid state systems. There are many first order Raman modes that appear in SWCNTs, but only a few are Raman active, the G-band (from 2D graphite) and the RBM (radial breathing mode). The RBM is a mode unique to nanotubes, not appearing in the graphite equivalent, this mode can be found in the frequency range 120-350cm^{-1} [118] for SWCNTs with diameter range 0.7-2nm, and is due to all the carbon atoms around the circumference moving in-phase in a radial direction perpendicular to the tangent of the circumference. This RBM feature is different in each (n,m) confirmation of nanotube, with the frequency shift varying inversely proportional to the diameter of the tube by;

$$\omega_{RBM} = \frac{A}{d} + B, \tag{2.11}$$

where d is the tube diameter and A and B are parameters that vary depending on the tube environment [114, 119]. Furthermore, the RBM is strongly dependant on resonance conditions, and the resonance energies correspond directly to the energy gap between the vHs singularities, which by the Kataura plot (figure 2.5) is strongly related to the tube diameter.

The other first-order feature in SWCNTs is the G-band is a mode that appears in 2D graphite at around 1582cm^{-1}, and is related to the tangential vibrations of two carbon atoms in the graphene unit cell. In the case of SWCNTs, this mode is split in to various features depending again on the (n,m) confirmation of the tube between 1520-1595cm^{-1}. This splitting can be assigned to two main features, the G^{+} at 1593cm^{-1} and the G^{-} at 1570cm^{-1}. Out of these two features it is only the G^{-} band that exhibits any diameter dependence, in addition the G^{-} band is also sensitive to the (n,m) confirmation of the tube. For semiconducting tubes the G^{-} is well fitted to a Lorentzian lineshape, whilst for metallic tubes the band is asymmetric, fitting to a Breit-Wigner-Fano (BWF) lineshape [152]. It is these differences in the Raman that make it a powerful tool for characterisation of nanotube samples to investigate the diameter of the tubes, distinguish between metallic and semiconducting tubes and importantly for this thesis, probe the charge transfer due to doping of the SWCNT[38, 80].

In second-order Raman scattering the $\bar{q}$ scattering wave vectors cause the electron to return to its original k point after the scattering event. Second order Raman can consist of (1) one-phonon and one elastic scattering, or (2) two-phonon scattering. An example of both of these cases are observed in SWCNTs. The one-phonon case is observed as the so-called D-band at 1350cm^{-1} and for two-phonon the G$'$-band at 2700cm^{-1}, an overtone of the D-band[153]. The D-band is activated by disorder in the graphite crystal [154], and has a dispersive behaviour in SWCNTs where the Raman shifted frequency red-shifts $\sim$53cm^{-1} per eV of laser energy [114, 155].

Overall there are several Raman active features of carbon nanotubes that can yield useful information about the nature and type of tube present. In the experiments performed in this thesis, the only significant Raman feature of SWCNTs that needs to be considered are the RBMs, as the expected Raman shift of this feature has a frequency shift comparable to that of the Raman features of the HgTe filling materials investigated.

Chapter 3

Experimental Apparatus and Techniques

In this chapter, the experimental apparatus and techniques employed throughout this thesis are discussed. The main experiments in this body of work are based on the continuous wave (CW) Resonant Raman Spectroscopy (RRS) as a function of sample temperature. The first section of this chapter discusses the preparation and TEM characterisation of Mercury Telluride filled SWCNTs (HgTe@SWCNTs). The second section contains details on the laser system employed for RRS experiments, including a discussion of the Raman microscope and efficiency throughput of the detection system. The ability to probe the Raman scattering cross-section as a function of excitation energy and sample temperature in a repeatable manner was crucial to the results of this thesis. Therefore a discussion is provided on the techniques used to take repeatable measurements on filled nanotube samples, and to understand the sources of uncertainty in the measurements. This high level of repeatability in the experimental system is also presented in our 2016 publication [8]. Analysing and fitting data was also an important part of understanding the physics of the results, so a section is also dedicated to the data processing portion of this work. Finally, this chapter concludes with a brief review on how the RRS experiments were performed for a general overview of the chapter.

3.1 Sample Preparation

Filled carbon nanotube samples were prepared using a technique known as melt infiltration [116, 90, 156]. Where a desired filling material, of an appropriate wetting energy, is incorporated into a host tube by heating the tube-material conglomerate above the melting point of the filling material and letting capillary action draw the melt inside the tube[90]. 50mg of nanotube product was preheated to $\sim 500^{o}C$. Nanotube product was transferred to an Argon atmosphere glove box with the desired filling material (i.e.

HgTe). Equal mass of nanotubes and filling material were ground together for ∼20mins in an agate pestle and mortar. This mélange of tube and filling material was transferred to a quartz ampoule which was subsequently vacuum sealed. The sealed ampoule was then placed in a muffle furnace and heated at a rate of $5^oC\ min^{-1}$ to $\sim 100^oC$ above the melting point of the filling material (for example Mercury Telluride has a melting point of 670^oC). The furnace cycled the temperature $\pm 100^oC$ either side of the melting point for 12 hour periods for a total cycling time of 2 days. This process allows the filling material to melt, then capillary action draws the melt into the central pore of the tube. The sample was cleaned to remove exterior bulk material and other impurities. Cleaning the sample involved removing it from the ampoule and refluxing in an admixture of HCl and HNO_3 with a 1:1 ratio and ∼50mL for about 1 hour. The final product was then washed with deionised water through filter paper. The process of refluxing and washing with deionised water is advantageous as it removes bulk compound and other impurities whilst leaving the nanowire within the SWCNT intact.

It is generally accepted that Raman studies on SWCNTs are best performed at a single nanotube level, where effects of inhomogeneous broadening on the Raman features are minimised [31, 32, 152]. Whilst isolated SWCNTs nanotubes can be grown through CVD techniques [32], isolating filled carbon nanotubes is not trivial and involves many extra chemical steps and usually centrifuging [97] is involved, complicating the sample, and the preparation. In addition, spectral acquisition is further complicated as it can be difficult to locate a tube under the microscope and the relative signal of the Raman scattering is weak. This work therefore focuses on studies of bundled, filled SWCNTs.

To generate the sample to be probed through Raman, filled nanotube powder (∼20mg) was added to a vial containing 20mL of Ethanol. The vial was then sonicated in a bath sonicator for ∼20 mins to break up large agglomerates of nanotube product. The sample was left in the sonic bath for ∼24hrs to allow for potentially harmful aerosolised tubes to settle back into suspension (Figure 3.1 a). A small amount ($\sim 100\mu$L) of the filled nanotube mixture was pipetted onto a silicon substrate with a 200nm SiO_2 coating and the ethanol allowed to evaporate at room temperature. The resulting sample can be seen in figure 3.1 b, where dark black agglomerates of nanotube product are easily observable by eye. The resulting silicon chip was then mounted onto a sample holder using silver conductive paint and sealed in a cryostat which was used to hold the sample under a moderate vacuum of about $1x10^{-6}$mbar.

Depending on the exact method of fabrication, raw nanotube product can come in a range of diameter ranges, and vary in concentrations of type (i.e. semiconducting or metallic). Based on this, multiple sample of filled nanotubes were made using nanotubes from different sources (Sigma Aldrich, NanoIntegris and tubes produced by Krestinin et al.[157]). This was done to compare the Raman features of the filling compound to understand if the host tube environment had a significant effect on the Raman features. It was found that across all three tube types the Raman spectra were generally the same,

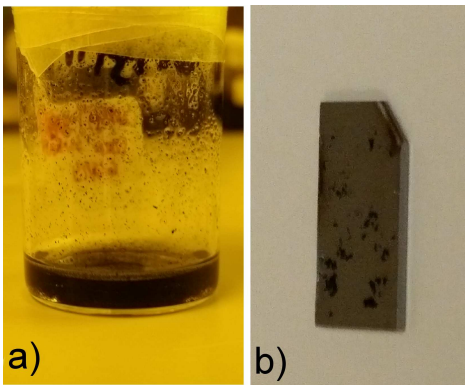

Figure 3.1: (a) Sample vial containing filled nanotube product suspended in ethanol after sonication. Panel (b) shows filled nanotube sample deposited on a 200nm SiO_2 coated Si chip, dark black agglomerates correspond to nanotubes.

this is highlighted by the data presented in figure 3.2, which shows a representative Raman spectra taken at 4K, using 1.776eV incident laser energy of the 3 tube types. The only differences between the 3 samples were the frequency shift of the RBMs, and some variation in the relative heights of the peaks. The first of these differences can be understood due to changes in the nanotube diameter between samples, which is expected. The second can be understood due to changing sampling area and inhomogeneous effects. By inspection of figure 3.2, it is clear there is a remarkable level of similarity in

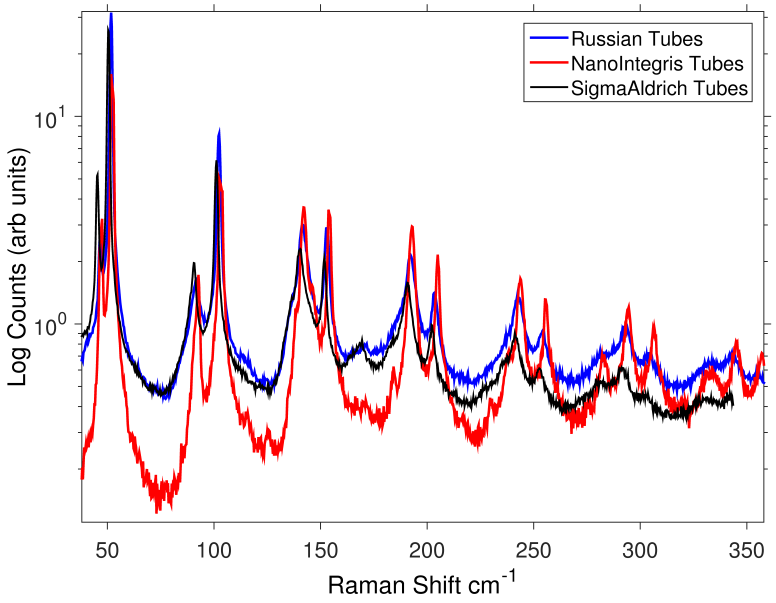

Figure 3.2: Representative Raman spectra of HgTe@SWCNTs, using nanotube batches from three different source all taken using 702nm incident wavelength. The scale of the y-axis has been logged for ease of viewing the higher order Raman features.

the Raman spectra of the filling modes within all three tube types. This suggests that in each sample there is generally the same crystal structure that predominates throughout

the sample. The difference between the intensity of the background between the red and blue/black lines can likely be explained due to probing a different sample environment with a differing number of tubes. Overall the data suggests that the signal observed is not unique to one batch of nanotubes from a particular source. In subsequent chapters, Raman experiments were performed using a single sample of HgTe@SWCNTs, from the Krestinin source. This source was chosen for the presented Raman experiments because in general the filling quotient was greater, and the nanotube diameter range narrower.

3.1.1 HRTEM Characterisation of SWCNTs

The empty and filled form of the SWCNTs from the Krestinin source were characterised under high resolution transmission electron microscopy (HRTEM) to understand the range of tube diameters in a typical sample. A large variation in nanotube diameter could effect the type of crystal formation of nanowires within the tube, which would lead to greater uncertainty as to what the structure that is probed under Raman is. The imaging and crystal modelling was performed by Jeremy Sloan at Warwick University. Images of nanotube samples were obtained by using a JEM-ARM 200F microscope operating at 80kV equipped with duel STEM/HRTEM CEOS aberration correctors and a Gatan SC1000 ORIUS camera equipped with a 4008x2672 pixel CCD [1].

3.1.1.1 Unfilled SWCNTs

HRTEM characterisation was performed on a number of samples of the Russian SWCNTs (Krestinin source). A sequence of representative HRTEM images of the unfilled SWCNTs are presented in figure 3.3, which shows the TEM image, alongside a histogram to show the tube diameter (right). It is important to note that the diameters presented in figure 3.3 are not a true representation of the actual diameter of the nantoubes. In reality, the true diameter is slightly larger than the observed diameter because of curvature effects of the tube, this effect is more pronounced at smaller diameters and can be corrected for using a simple linear correction of $y = 1.1x - 0.0879$, where x is the true diameter, and y is the measured diameter in nm. This correction factor was calculated by Jeremy Sloan after multiple diameter measurements of nanotubes with a known (n,m) index, and therefore a known true diameter. A table of the measured diameter and the true diameter for each nantoube in figure 3.3 is presented in table 3.1. Also presented in this table is the best assignment for the (n,m) index of the tube based on the diameter and the TEM observations.

By inspection of panel A of figure 3.3 it can be seen in that there are wall-carbons visible on the lower half of the fragment, this is also the case for panel B. This observation can be understood if the SWCNT measured was chiral [158], and allows for a better assignment of the (n,m) index of the tube based on the true diameter, as chiral tubes

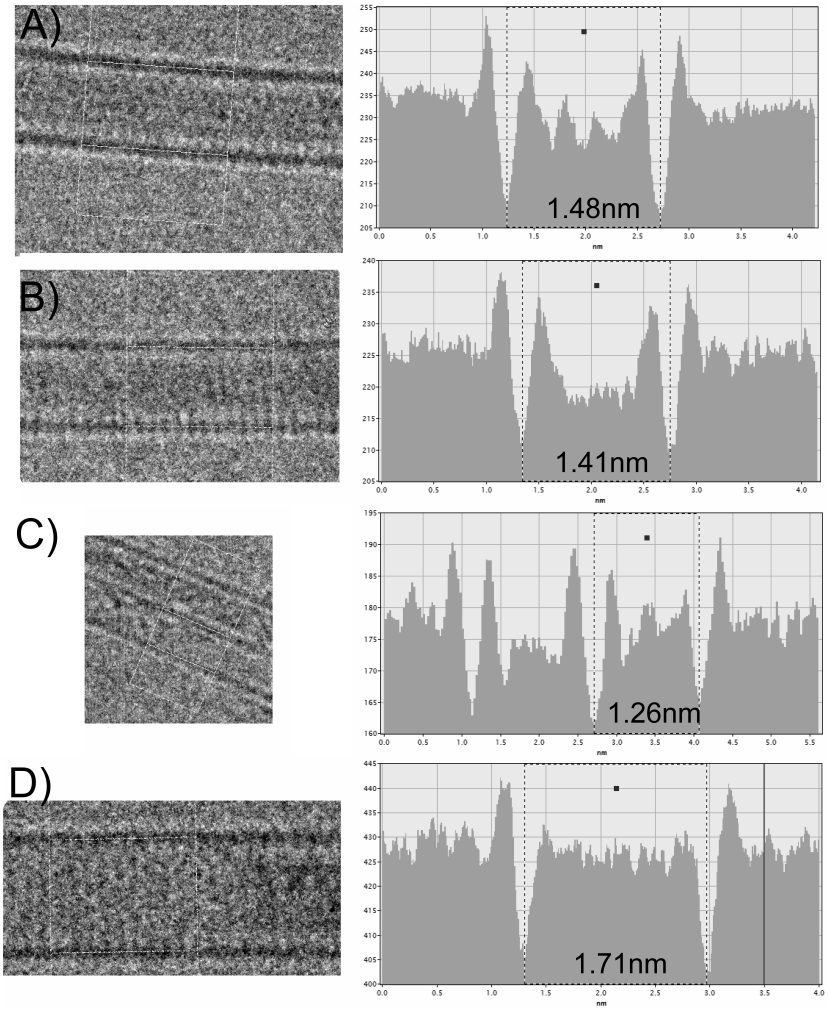

Figure 3.3: Representative HRTEM images (left) of unfilled SWCNTs from the Krestinin source. Also shown (right) is the measured diameter of the sample nanotube.

Table 3.1: Table showing the observed diameter from the labelled nanotubes presented in 3.3, alongside their calculated true diameter and the most likely (n,m) index based on image observations and diameter.

Label	Observed Diameter (nm)	True Diameter (nm)	(n,m) assignment
A	1.48	1.55	(12,11)
B	1.41	1.48	(16,5)
C	1.26	1.33	(17,0)
D	1.71	1.78	(16,10)

have a particular set of allowed n,m indices. The true diameter of the tube presented in panel B was ∼1.5nm, and formed the vast majority of nanotube diameters in the sample. Panel C of figure 3.3 shows a sample of the smaller tubes that appear in the sample, it can also be seen in this image that there are two tubes bundled together. This is common in nanotubes and gives some overall alignment to the tubes which will become important when understanding the polarisation dependence of the Raman

spectra. Panel D of figure 3.3 shows an example of the larger diameter nanotubes that are in the sample. In general the diameter distribution follows a Poisson distribution, after analysis of multiple HRTEM images, it was found that ∼85% of the sample consisted of tubes within the diameter range of 1.2-1.6nm, which is the ideal range for formation of the tubular form of HgTe (1.35-1.45nm)[159]. In some cases the sample consisted of extremely large nanotubes (∼5nm), however these were rare and no filled forms of these tubes were found.

3.1.1.2 Filled SWCNTs

HRTERM images were acquired under identical conditions as the unfilled case, using the HgTe filled SWCNT samples. After filling and purification, EDX analysis was performed and for the samples surveyed, it was found there was a one to one ratio of Hg to Te throughout all the sample. An extensive HRTEM survey demonstrated that the diameter range was the same as the unfilled tubes and the vast majority of nanotubes (>80%) were filled with HgTe. It was also found through TEM analysis that the predominant form of HgTe throughout the sample corresponds to the microstructure depicted in figure 3.4 (a). It can be seen by inspection of figure 3.4 (d top panel) which shows a fragment of tubular HgTe imaged in a discrete tube next to a TEM simulation of the structure based upon the ball and stick model from panel b. It is clear that the predicted TEM image provides an excellent match to the observed structure corresponding to a 70° orientation of the HgTe fragment. Throughout the sample multiple different structures were observed, however after performing rotation and tilt based simulations of the trial HgTe structure (3.4 C) it was found that all of the different structures were actually due to a single crystal form of HgTe where the crystal structure was rotated with respect to the incident beam. This effect of beam orientation with respect to crystal structure is illustrated by panel B of figure 3.4. Similarly, relative tilt of the sample with respect to the incident beam can result in the same effect. TEM simulations at multiple tilt and rotational angles were also performed to identify tilted structures. It was found that there was a good match between experimental observations and simulated tilt angles based on the trial structure, as can be seen in panel F of figure 3.4.
Overall the TEM evidence provides useful information that can be used for DFT calculations (presented later), and suggests that in the filled nanotube case the predominant form of HgTe is the same crystal structure. This is further supported by the spatial homogeneity of the Raman spectra observed in multiple positions on the same and different samples of filled SWCNTs.

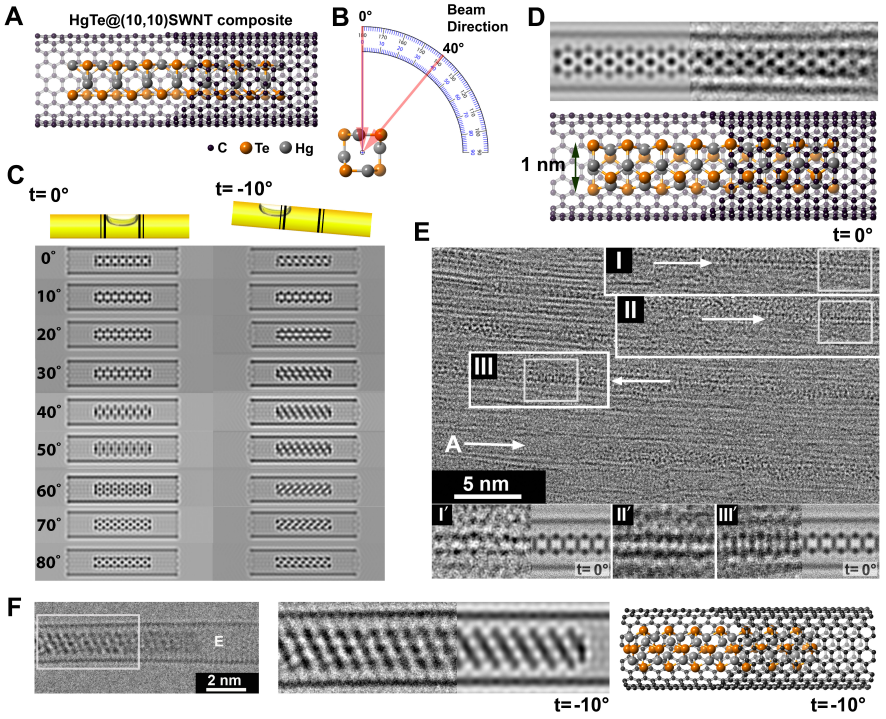

Figure 3.4: Structure models, HRTEM simulation protocol and experimental images of ∼1nm thick HgTe nanowires embedded in ∼1.4 nm diameter SWNTs. A typical partial cutaway model (A) of a SWNT is assembled in which a ∼1 nm diameter, 3 nm long fragment of HgTe, based on a repeated $Hg_4 4Te_4$ motif[5, 1] is embedded in a (10,10) SWNT in a starting orientation. Relative to this orientation, it is possible to define different electron beam directions (B) in order to represent different projections for a series of orientations of the HgTe@(10,10)SWNT composite (C, LH simulations). For the interpretation of some tilted fragments, it is necessary to model the effect of this also (C, top graphic and RH simulations). HRTEM images (D top right) can be matched against the table (C) and matched with the experimental image (D top left and right) and this will correspond to a particular orientation of the fragment (D bottom cutaway model). For a HRTEM image obtained from a thin SWCNT bundle (E), this can be used to observe embedded ∼1 nm HgTe nanowires (I, II and III) and correlate these with simulations in the table (i.e. insets I', II', and III'). Some fragments are tilted (F, left) by some angle t, an effect that can be easily be modelled by simulation (F, middle) which corresponds (cutaway model, F right).

3.2 Experimental Apparatus for Raman Spectroscopy

This section focuses on the experimental systems developed for optimal, repeatable detection of Raman spectra from all samples studied in this thesis. The overall schematic for the system used to undertake Raman experiments is presented in figure 3.5. This is placed here as a reference for points that are discussed in this section, a detailed discussion of figure 3.5 is presented later in section 3.3.

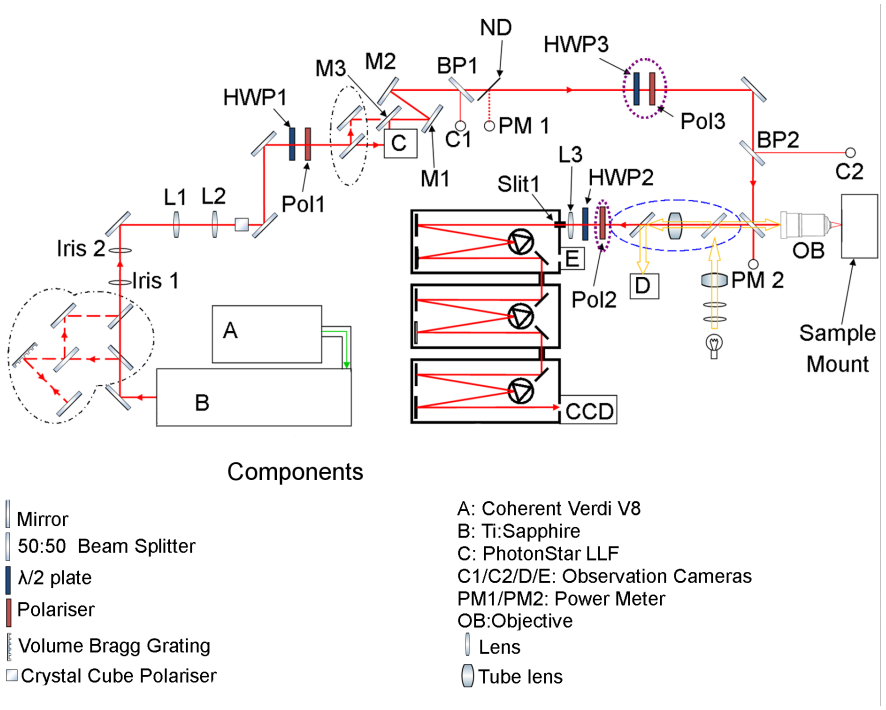

Figure 3.5: A plan view of the entire experimental system employed to undertake high resolution RRS experiments.

3.2.1 Laser

The laser source used in this thesis was a Coherent Mira 900-P Titanium Sapphire ($Ti:Al_2O_3$ or Ti:Sapphire) solid state laser, pumped by a Coherent Verdi V8 frequency doubled diode-pumped single mode laser of wavelength 532nm. The Ti:Sapphire is an ideal tool for resonance Raman spectroscopy experiments as it is continuously tunable between 680-1000nm in CW mode and can be mode-locked and passed through a 2^{nd} harmonic generator to allow access to the blue regime (400-460nm). The theory of operation of such lasers and the principle of mode-locking can be found in various textbooks [160, 161] and hence will not be covered in detail in here. This subsection discusses the basic principles of operation of the laser system used and the techniques used to characterise and monitor the laser pulse.

3.2.1.1 Laser Output

The schematic for the laser cavity of the Mira-900 is illustrated in figure 3.6. A pump beam (Verdi V8) using 532nm (green) light enters the system and is centred on a focusing lens (L1), which focuses the beam onto the Ti:Sapphire crystal. When performing experiments the wavelength of the Ti:Sapphire is tuned by adjusting a birefringent filter (BRF) using a micrometer gauge. When this micrometer is adjusted, further corrections must be made on the GTI to optimise power output. The output spectrum of the laser was monitored in real-time using an Ocean Optics HR400 high-resolution spectrometer

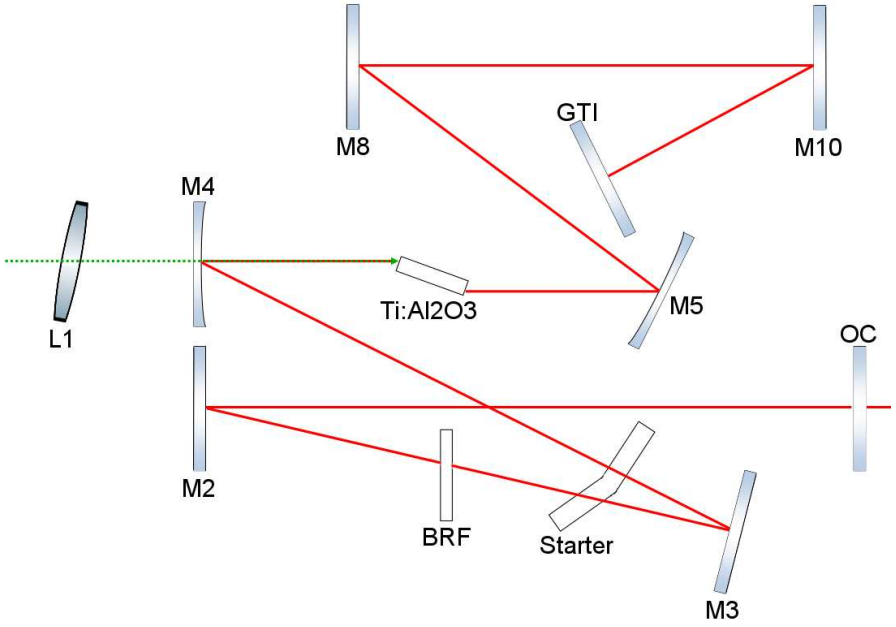

Figure 3.6: Schematic of Coherent Mira 900-P laser cavity in CW mode, showing Gires-Tournois interferometer (GTI) for daily optimisation of laser cavity, output coupler (OC) for initial alignment of laser and BRF (birefringent filter) used to tune the wavelength in CW mode.

with a resolution of 0.25nm/px. The output power of the laser system was measured using a Spectra-Physics 407A thermopile detector, rated for operation between <5mW and to 20W. The power meter was placed in the beam path and power recorded was maximised at each incident wavelength for Raman experiments by adjusting the GTI on the laser. The CW component of the laser was monitored by a diode in the MIRA cavity through a digital display on the laser control box. In general the power output of the laser varies as a function of wavelength as illustrated by the data presented in figure 3.7, with a peak power at ∼800nm, dropping off rapidly at the extremes of the operational limit. It is due to this lack of power, and absorption of water-vapour, that makes mode-locking difficult at certain wavelengths. With this in mind it is important to keep the laser optics clean to allow better power throughput, and when mode-locking is desired, to purge the system with gaseous Nitrogen to lower the relative humidity of the cavity.

There are a number of advantages in using a Mira 900-P for resonance Raman experiments. The main advantage of which is the low noise (<0.1%) and long term stability of the intensity (<3%) of the output beam. This is important for RRS measurements which are taken over the course of several tens of seconds to minutes, to ensure that any variation observed in intensity is not due to a change in the output laser parameters. Further information about how the variations in incident power can effect the Raman signal is detailed later in the chapter.

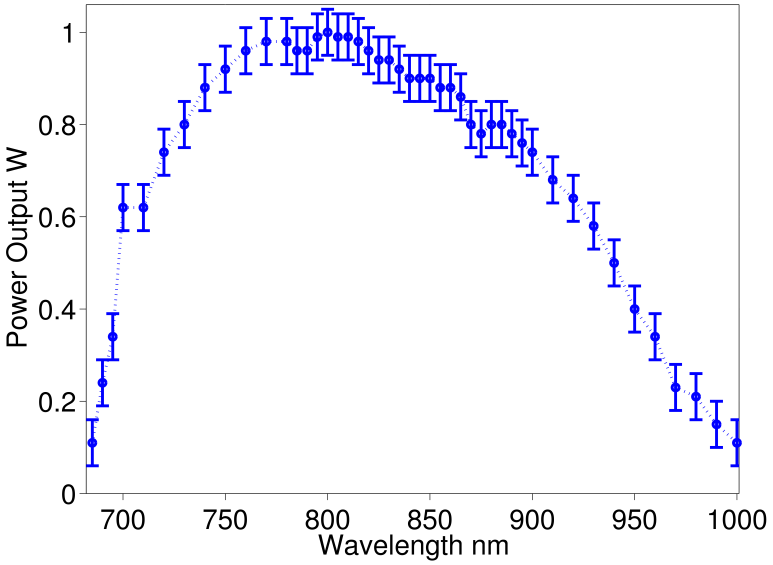

Figure 3.7: Output power of Mira 900-P using 6W pump source, measured in Continuous Wave (CW) mode over entire operational range

3.2.1.2 Laser Filtering

When operating in CW mode it is necessary to spectrally filter the laser to remove unwanted broadband fluorescence produce by the Ti:Sapphire that could enter the detection system. In addition, the method for filtering the beam both at this step and in the spectrometer itself needs to produce as narrow bandwidth as possible, as it is predicted (and demonstrated) that Raman modes in low-dimensional structures such as those investigated in this thesis appear at very low energy. The laser source was filtered using a Photon Etc laser line tunable filter (LLTF). This filter has an operational range between 700-1000nm with a bandwidth of <0.4nm, with a suppression of ND4 at 50cm^{-1} from the laser line, ideal for Raman spectroscopy experiments close to the laser line. When the laser was to be operated below 700nm, the Photon Etc LLTF does not function. For wavelengths <700nm a Volume Bragg Grating (VBG), with a bandwidth of <0.3nm was employed and the optical path changed accordingly (figure 3.5 black dashed lines) to filter the Ti:Sapphire laser. The full operational range of the VBG was between 680-720nm, so when the VBG filter was used RRS were measured over the full operational range to allow for the most overlap between the spectra acquired using the VBG and the LLTF.

3.2.1.3 Raman Microscope

The experiments in this thesis were performed using a custom built Raman microscope, in a back-scattering configuration as illustrated by figure 3.8. The back-scattering geometry delivers laser light down an objective whilst collimating the back-scattered light and

coupling it into the spectrometer for detection. This configuration is used in most studies on nanotube Raman [162, 163]. The design also includes an in-situ optical microscope which allows for real-time imaging of the laser spot on the sample. This addition, along with motorised actuators was an invaluable tool for the precise repositioning of the sample, and allowed the development of a Raman mapping system. Figure 3.8 illustrates

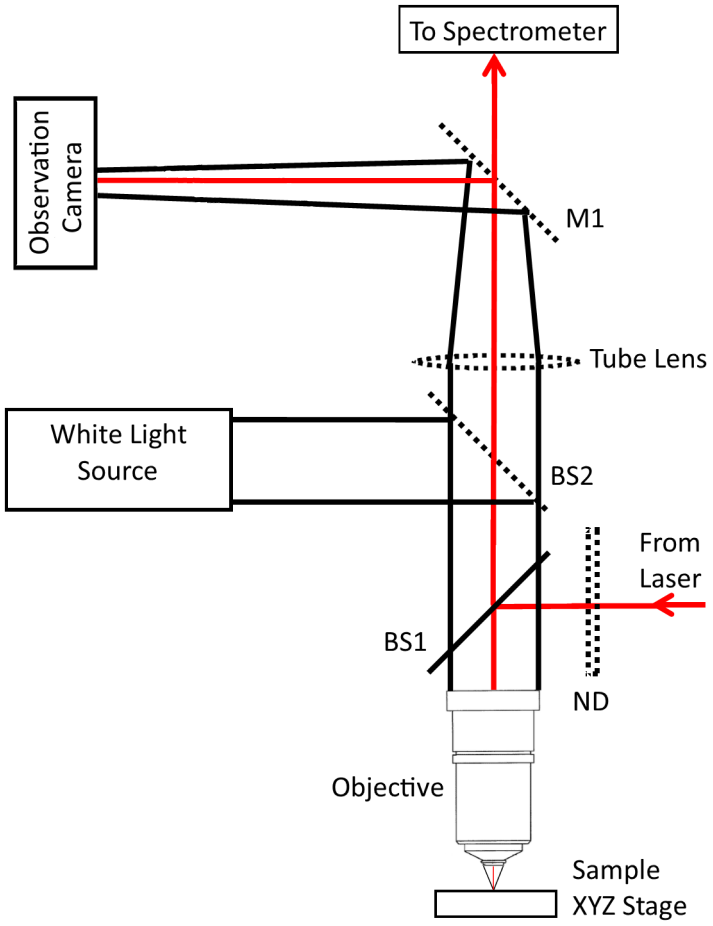

Figure 3.8: Schematic of Raman microscope with in-situ optical microscope. Dashed lines indicate components that are changed over when moving between imaging modes.

the schematic used for the 2 types of imaging optics (Raman and white light imaging). A typical white light illumination source was setup with an aperture stop and field stop. When optical sample viewing is required, a beam splitter (BS2) and mirror (M1) are added the optical set up as indicated by the dashed lines to position the white light onto a Chameleon CMLN-1352M CCD USB camera. A Zeiss tube lens was placed at a distance from the objective to form an image of the objective focal plane on the camera. In addition a neutral density filter (ND10) was added before the laser beam entered the objective to allow for viewing of the laser spot without saturating the camera. When used for Raman spectroscopy, laser light is initially split through a thin 50:50 beam splitter and focused onto the sample through a LMPLan-IR 50x objective with NA of 0.55,

focal distance of 3.6mm and working distance of 6.0mm. The light transmitted through the beam splitter is incident upon a Newport 2832-C power meter which is used as a reference point to set the power onto the sample surface. Because the beam is focused, this results in a sampling volume, which has a focal spot size where the energy density is greatest. In general Raman spectra were taken at the focal point of the laser spot to give the greatest Raman scattering signal. The back-scattered light passes through the beam splitter again, some of which is retroreflected along the incident path (discussed later) where the other portion is directed towards the entrance slits of the spectrometer. Prior to the spectrometer entrance slits there is a lens which focuses the beam onto the slits, and before that a half-wave plate to maintain the input polarisation to match the grating efficiencies (discussed later). The sample was mounted on an XYZ stage to move the sample spatially (XY) and through the focusing volume of the laser beam (Z), to position to the focus of the laser spot.

3.2.1.4 Spot Size Measurements

The laser spot at the focus was measured by use of a knife-edge measurement. A blank silicon chip was mounted on the XYZ stage and the laser was set to 2mW and 1.776eV excitation energy. An ND filter was placed in the optical path 3.5 after beam-profiler 1 (BP1) and a second power meter head placed to measure the retroreflected Rayleigh scattered laser light. The power meter was placed at a sufficient distance along the retroreflected path to best match the distance the Raman and Rayleigh scattered photons would travel from the sample through the spectrometer and to the CCD. The sample was positioned such that the laser was visible on a piece of blank silicon but close to the edge of the substrate. The CCD and the power meter head were controlled through a LabView script to record the reflected power, and the Raman spectrum of the well-defined LO phonon mode of silicon at 520cm^{-1} [164] as a function of discrete 100nm steps in the x-direction (horizontal), until it was clear the laser spot was no longer on the silicon substrate. The focal point for the experiment was chosen as the point which gave the maximum retroreflected power. The results of both these measurements were fit in Matlab using a least-squares fit to equation 3.1.

$$y = Aerf\left(\left(x - B\right)C\right) + D \tag{3.1}$$

Where $erf(x)$ is the error function and A,B,C and D are fitting parameters. The fitted data for the absolute power reflected, and the peak of the Raman scattering is shown in figures 3.9 and 3.10 respectively. By inspection of the data, there is a clear drop-off of reflected power (left) and the Raman intensity peak (right) as a function of micrometer position.

Through the best fit, it is possible to extract the spot-size in two ways, the first being an approximation of the spot size by taking 90% and 10% of the maximum value of the fit.

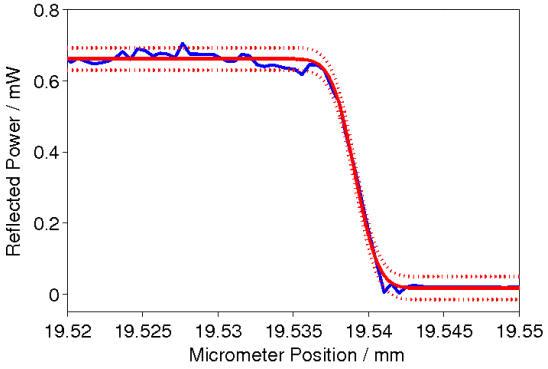

Figure 3.9: Reflected power fitted to error function, dashed lines correspond toe 95% confident bounds from fit.

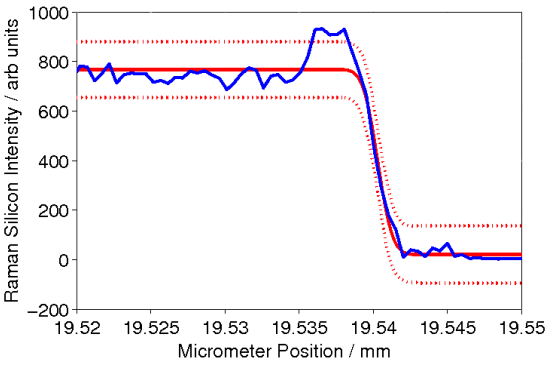

Figure 3.10: Peak Raman signal fitted to error function, dashed lines correspond toe 95% confident bounds from fit.

The other more robust method is to plot the derivative of the error function, which is a Gaussian line-shape, and to calculate the width at $1/e^2$ of the maximum absolute value of the Gaussian fit. The derivatives of the error function for both the reflected power and maximum Raman scattering intensity is shown in figures 3.11 and 3.12 respectively. A table of all possible methods for calculating the spot size is presented in table 3.2. From this sequence of experiments, performed at room temperature, the average spot size and standard deviation was determined to be 3.1±0.7μm. The spot size measurements were

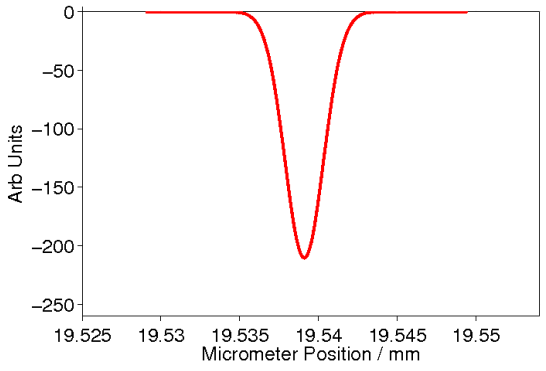

Figure 3.11: Gaussian Function extracted from fit to reflected power.

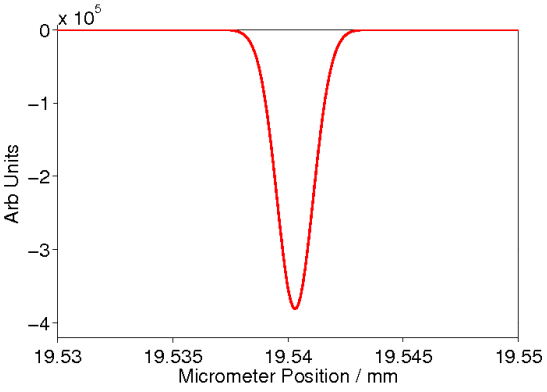

Figure 3.12: Gaussian Function extracted from fit to Raman peak.

Method	Reflected Power	Raman Peak
90/10 Error function	2.1μm	3.3μm
$1/e^2$ derivative	3.2μm	3.8μm

Table 3.2: Spot size as determined by fitting reflected power and Raman peak to the error function and calculating the position at 90% and 10% of the maximum value, and by calculating the $1/e^2$ of the derivative of the function.

also performed as a function of sample temperature and it was found that there was no significant spot-size dependence as sample temperature was varied.

3.2.2 Controlling the Sample Environment

To measure the Raman spectra both on and off resonance, and to study the temperature dynamics of the phonons, it was necessary to mount the filled SWCNT sample in a way that can be temperature controlled between 4-300K as well as having optical access to the sample. Additionally, it was important to perform various experiments on the sample spot of interest, to ensure variations in Raman cross-section measurements were not due to measurement of different tube formations, orientation of the crystal structure, or density of sampling area. This section discusses how the sample was mounted and how the environment was controlled in such a way as to reduce the sample drift during Raman experiments.

The silicon chip with nanotubes deposited was attached with silver conductive paint to a chip holder and mounted in a helium flow Oxford Instruments Microstat (figure 3.13). The cryostat was evacuated by use of a Oerlikon PT70F Turbopump, which at room temperature holds a stable vacuum of $\sim$6x10^{-6}mbar inside the sample chamber. The front flange of the cryostat mount has a $\sim$1cm^2, 0.5mm thick, sapphire window to allow laser probing of the sample area. The cryostat was mounted onto the XYZ motorised stage which was securely fastened to the lab bench to minimise movements of the mounts. Inside the cryostat chamber, the sample was mounted to a silver cold finger which was thermally anchored to the tip of a heat exchanger. A syphon was used to link a 60 litre liquid helium dewar to the cryostat for cryogenic measurements. The cryostat exhaust line was connected to a helium gas flow controller and a small gas flow pump, which was used to control the flow of helium to the heat exchanger. Temperatures below 4.2K were achieved by lowering the pressure in the heat exchanger using a needle valve on the syphon. The internal sample temperature was measured by using a three point calibrated rhodium iron temperature sensor which was mounted on the heat exchanger. To control the sample temperature between 4K and 300K, an Oxford Instruments ITC502 temperature controller would automatically supply and monitor a current to a heating element which was in thermal contact with the heat exchanger. This setup had a temperature stability of <0.1K, once the system came to a thermal equilibrium.

During cooling and heating thermal expansion of the cold finger would cause sample drift. This meant that it was necessary to track the sample position as the temperature was changed and make positional corrections to return to the sample to the same sampling area. This was done using the in-situ microscope (section 3.2.1.3) and stage controllers, where the relative coordinates of the desired sample and an obvious feature about the sample (i.e. edge of silicon) were recorded at the start of the experiment. Once the sample position had been relocated, it was left for 40 minutes to ensure the environment was in

Figure 3.13: An image of the cryostat that the nanotube samples are mounted in to cool to cryogenic temperatures.

thermal equilibrium. As stated, the cryostat was mounted on an XYZ-stage controlled with high-speed and high-load motorised actuators with an incremental motion of 100nm and a backlash of $\sim$1.1μm. These actuators can be used manually to reposition the sample, or used alongside a LabView code, to control the position. It was found by visually returning to the same sample spot multiple times, and comparing the images on the camera that the sample could repositioned to within 500nm, which is less than the laser spot size. During Raman experiments, the syphon that anchored the cryostat to the helium dewar caused a significant amount of sample drift due to vibrations in the pump, it was found that this could be significantly dampened by draping a cloth over the syphon and vacuum line, this reduced vibrational motion to <500nm.

3.2.3 Raman Detection

Raman scattering is inherently a weak optical process, where approximately 1 in 10^7 photons undergo Raman scattering [165]. With this in mind, the detection system must be able to measure very small signals amongst the large quantity of Rayleigh scattered light. The system used in this thesis was a Princeton Instruments TriVista triple 600nm spectrometer and a Roper Scientific PyLoN LN/400BR liquid Nitrogen cooled deep depleted CCD. This section provides details of the detector system including its configuration and specifications and the techniques used to calibrate the detector.

As seen in Figure 3.14, the spectrometer consists of 3 stages all based upon the same Czerny-Turner design, using a collimating mirror, changeable turret grating, focusing mirror and both entrance and exit slits. For Raman detection, the spectrometer has 2 main modes of operation; subtractive and additive mode, both with advantages and disadvantages. The Raman experiments in this thesis use the system in subtractive mode. With the spectrometer set in subtractive mode, the first and second stage are both used

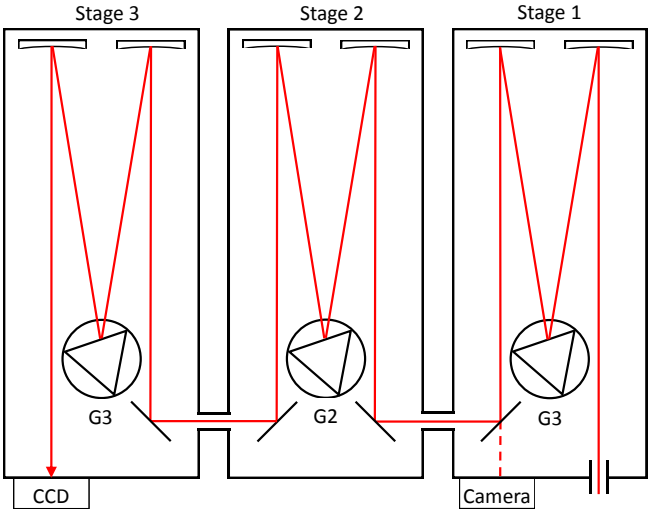

Figure 3.14: Diagram of Raman spectrometer.

as a tunable bandpass filters, allowing the desired portion of the spectrum through to stage 3 where the grating disperses the light and projects it onto the CCD. In this mode, illustrated in figure 3.15 the resolution is defined by the groove density of the grating in the third-stage, and whilst the resolution is reduced in comparison to additive mode, this setup has superior stray light rejection. Which means Raman measurements can be performed very close to the laser line, where one would expect to observe low energy phonons associated with a 1D material.

In subtractive mode the gratings in the first and second stage of the spectrometer have to be the same. In this thesis the gratings selected for stage 1 and 2 had a groove density of 900 lines per mm with a linear dispersion of 1.93nm/mm at 800nm. Depending on the excitation energy used, the input polarisation and the spectral resolution desired, two different configurations were chosen for the 3^{rd} stage of the spectrometer. Either 1800 lines/mm or 1500 lines/mm which have dispersions of 1.43nm/mm and 0.63nm/mm @800nm respectively. As the gratings exhibit different efficiencies and resolution for different wavelengths, the configurations were set and maintained at the start of resonance Raman experiments to optimise stray light rejection and to maximise CCD coverage. The experiments performed in this thesis were taken over wavelength range 680-1000nm, for this reason the optics within the spectrometer were protected silver coated, this allowed for better reflectivity over a relatively large spectral range. However the CCD detector efficiency is still wavelength dependent, this is discussed further in section 3.2.3.1. Another issue with the detection system is that it is heavily polarisation dependent with the highest throughput being when p-polarised (horizontal to the lab frame) light is used. It is therefore important to ensure that the polarisation state of the Raman remains invariant when entering to the first entrance slit (S1) of the spectrometer seen in figure 3.14. To maintain the polarisation input, a broadband half-plate was placed just prior

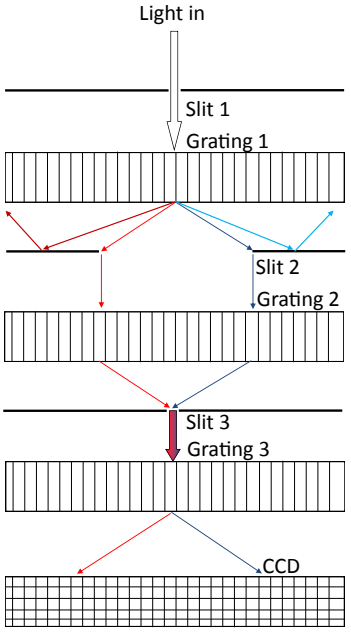

Figure 3.15: Schematic of spectrometer setup in subtractive mode

to the focusing lens before the entrance slits, which rotated the plane of polarisation to p-polarised. This had the effect of maximising the amount of any given signal, and minimising the chance that variation in signal would be due to a polarisation sensitive inefficiency of the detector.

3.2.3.1 Spectrometer Calibration and Resolution

As previously stated, the efficiency of the CCD varies significantly over the spectral range probed in this thesis. It is important that any variation in the spectral response is corrected for during RRS experiments, as the laser is tuned over a large wavelength range. If the efficiency throughput is not corrected for, it is impossible to be certain that a change in the intensity of the Raman spectra is due to a change in the Raman scattering rate, or due to the inefficiency of the detector at the wavelength.
To calibrate the detector system the following technique was used. Firstly an Ocean Optics LS-1-CAL-INT-220 tungsten halogen light source was collimated and passed through a linear polariser to either s- or p-polarised light. The spectral response on the CCD was measured in 5nm steps over the entire operational range of the detector system for both the 9_9_18 and 9_9_15 grating configuration in subtractive mode, for both s- and p-polarised light. The spectra was then compared to against the calibration data

curves from Ocean Optics for the lamp used. A function was applied in Matlab to calculate the efficiency correction factors between the data obtained and the white light calibration spectrum. To correct the Raman spectra, the raw data was imported into a function that applies the correction factor calculated to the spectrum for a particular central wavelength. If the centre wavelength shares the same value as the calibration data the correction factor applied was simply the actual value of correction factor. If the centre wavelength differed to that of the calibration data an estimate of the correction factor was made based upon a linear interpolation between the correction factor of the wavelength below and above that from the Raman data. This interpolation technique was a good approximation because the correction factor for a specific pixel varied linearly between two spectra taken 5nm apart.

To measure the fundamental resolution limits of the detection system, laser light was indirectly scattered into the spectrometer and the CCD triggered for 100ms centring the spectral window at the estimate for the laser wavelength. The resulting data for the laser line spectrum can be seen in figure 3.16. By inspection of the data presented in figure

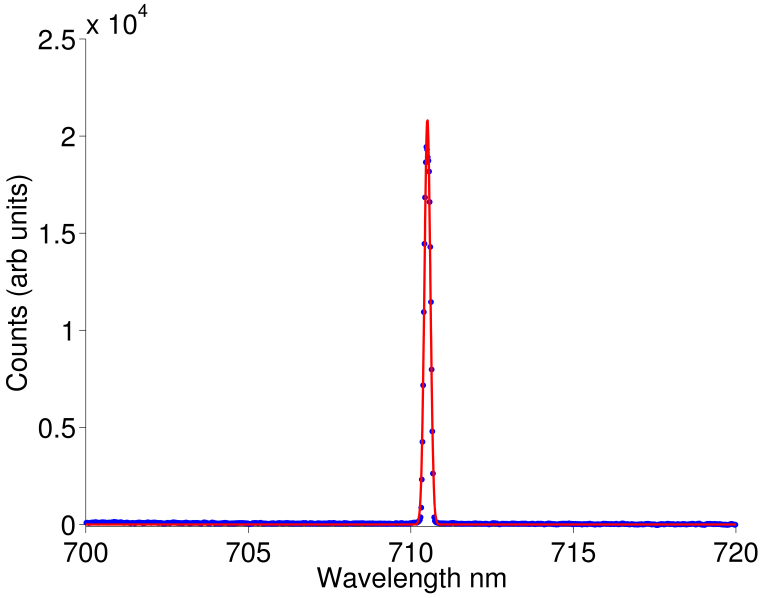

Figure 3.16: Laser line measurement of Ti:Sapphire source scattered into spectrometer, set up in 9_9_18_Sub configuration. Profile fitted with a Gaussian distribution indicates the wavelength was 710.51nm with a FWHM of 0.21nm, and a pixel resolution of 0.02nm/px.

3.16, it is clear that out of the 1340 pixels on the CCD, only 21 of them are involved in detecting measurable signal of the laser line. The limit of resolution on the measurement of the laser, by the FWHM is 0.21nm, or $\sim$4.5cm^{-1}. This is important when measuring the linewidth of the Raman features observed in the samples investigated in this thesis. The pixel width is much less than the linewidth of the laser, but the minimum detectable width would be associated with the pixel resolution of the CCD. The pixel spacing was calculated from representative Raman spectra at 1.776eV by taking the difference between the Raman shift of adjacent points. The resulting pixel width at

1.776eV is plotted as a function of Raman shift in figure 3.17.

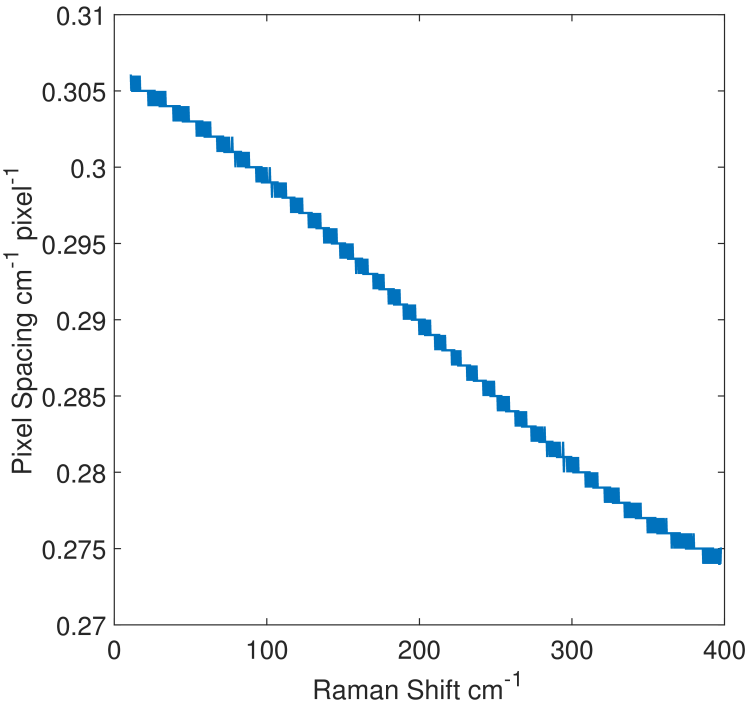

Figure 3.17: Calculated pixel spacing of laser line measurement from figure 3.16. It can be seen the dispersion is fairly linear over the whole CCD, but does not vary significantly over the linewidth of the observed Raman features. From this as pixel spacing correction factor can be calculated and applied to the Raman shifted peaks to calculate the spectral weight of the peaks.

It can be seen by the data presented in figure 3.17 that the Raman shift between adjacent pixels is not uniform over the whole CCD, this can be explained due to dispersion in the Raman system. By analysis of the data presented in figure 3.17, the dispersion is approximately linear and varies by ∼3% at both extremes of the CCD from the middle pixel value. Even though the effect is dispersive, the pixel spacing does not change significantly over the linewidth of the laser, nor the observed Raman peaks presented in this thesis. Whilst this effect does not directly effect the Raman intensity, it can effect the calculations of total spectral weight of the Raman peaks, and for this reason should be corrected for. The correction was calculated by multiplying the Raman shift for each observed peak, by its corresponding pixel spacing, and as the effect is due to dispersion, at each incident wavelength, a different correction factor was calculated and applied. This gave a pixel width correction factor for each Raman peak, which could be used to convert the measured linewidth into pixels, and therein calculate the spectral weight of a particular Raman feature.

3.3 Experimental Considerations

Now the details of the experimental systems have been explained, this section gives an overview of the experimental method for acquiring Raman spectra. A significant amount of work has gone into understanding the Raman system to best optimise the setup to yield the best throughput with highest level of repeatability when realigning. This section will also discuss the work undertaken to tune the system and understand the limitations on the experiments, it will focus on understanding repeatability in intensity, centre shift and linewidth of the Raman features observed. To understand the limitations on resonance Raman experiments, this section will first discuss the Raman system as a whole with reference to figure 3.5.

The Ti:Sapphire laser (component B) was pumped by a Verdi V8 (component A) details of the laser output can be found in section 3.2.1.1. As already stated in section 3.2.1.2, the laser is capable of being tuned between 680-1000nm, however the filter (component C) has an operation range only down to 700nm, so to complete the RRS experiments on HgTe filled SWCNTs, a VBG (Volume Bragg Grating) was added to the optical setup, as can be seen in figure 3.5 by the components encircled by black dashed line, further details of this will be discussed shortly. The laser was directed through 2 irises, and then through a sequence of lens' to collimate the beam (L1 and L2). The beam then passes through a crystal cube polariser to ensure the beam was horizontally polarised with respect to the lab frame. The polarised laser beam then passed through a half-wave plate (HWP 1) and second polariser (Pol 1) to control power and polarisation of the beam. When operating with in the range 700-1000nm the laser is filtered using the Photon Etc LLTF (component C). The filtered laser is steered onto the desired optical path (by use of M1 and M2) to couple in the spectrometer. This optical path was defined by initially optimising to the Silicon Raman peak and then made easier for subsequent experiments by the addition of observation cameras (C1 and C2) where beam-samplers reflected some laser light onto the cameras. The laser beam, is focused upon the sample and back-scattered Raman and Rayleigh light was split by the beam-splitter and coupled into the spectrometer. Other scattered photons were retroreflected and directed onto a power meter, PM1, to monitor the reflected power to provide a consistent reference point of focal position in which Raman measurements could be made. The Raman and Rayleigh scattered light that was coupled towards the spectrometer first passed through a half-wave plate (HWP2), which allowed control of the polarisation plane to best match to the detection efficiency of the gratings in the spectrometer. Then in turn through a focusing lens (L3), to focus the light onto the entrance slits of the spectrometer, where the Raman scattered light was measured.

There were also various sub-systems labelled on the diagram to monitor the experiments. Labelled with a blue dash line in 3.5 were the optics added to the setup to allow for the viewing of the sample and repositioning of the sample with respect to the laser. The components highlighted by the purple dashed line were added for polarisation dependant

experiments. Finally, as already discussed briefly, the VBG system that was used when the filter, C, was out of operational range. Components highlighted in the black lines were added to the setup, and M3 was removed. The laser was tuned to below 700nm and steered onto the VBG, which was then adjusted to suppress the throughput of the beam. The light was then retroreflected back onto the VBG and the retro-reflecting mirror adjusted to minimise the throughput as measured by a power meter. The irises were closed and the beam steered using the 2 preceding mirrors to centralise the laser spot ensuring the beam was now on the same optical path. A full discussion of the experimental methodology for collection resonance Raman data can be found in our publication [8].
Now we have discussed reviewed the experimental setup in full we are in a position to discuss the potential challenges on the repeatability of the Raman system, and in turn how these were controlled and corrected for.

3.3.1 Laser Heating

One factor that potentially could play a significant role in the uncertainty of the Raman data is localised laser heating. Because of the small focal spot size, it's possible that the sampling region could be heated to a temperature above which the heat exchanger from the environment is capable of equalising within the time scales of the experiment. This would mean the temperature sensors would give incorrect readings as to the exact local temperature. Many factors can effect the heat exchange from laser energy and the cold finger, most notably, using bundled tubes allows for more heat exchange than isolated ones. Furthermore, extreme low sample temperatures will, in theory have a lower specific heat capacity, as evident from the Debye model for specific heat capacity [136], which means that it would require less energy to cause a single degree change in temperature. The concern of laser power on the sample is most important when considering the temperature dependent data. If the laser were to heat the sample above the indicated temperature, it may introduce non-linearities in the Raman signal skewing the results of the temperature dependant measurements.
To check the laser power dependence on the sample Raman spectra was collected on the filled carbon nanotubes as a function of discrete changes in power from 0.01mW to 10mW, using 1.76eV, and the intensity of the B modes determined via Lorentzian fitting. This was performed at 4K, and repeated at 25, 50, 100, 150, 225 and 295K. In each case the Raman intensity was plotted as a function of incident power to determine the point where non-linear effects began to dominate and therein perform subsequent experiments using an incident power in the linear regime. The power dependence on the Raman intensity for 4K, for powers between 0.01-1.1mW is presented in figure 3.18. It is clear from the data presented in this figure that the intensity of Raman scattering is non linear at higher powers, however, it can be seen that at suitably low power the intensity is relatively linear. It was found for sample temperatures of 4K, 25K, 50K,

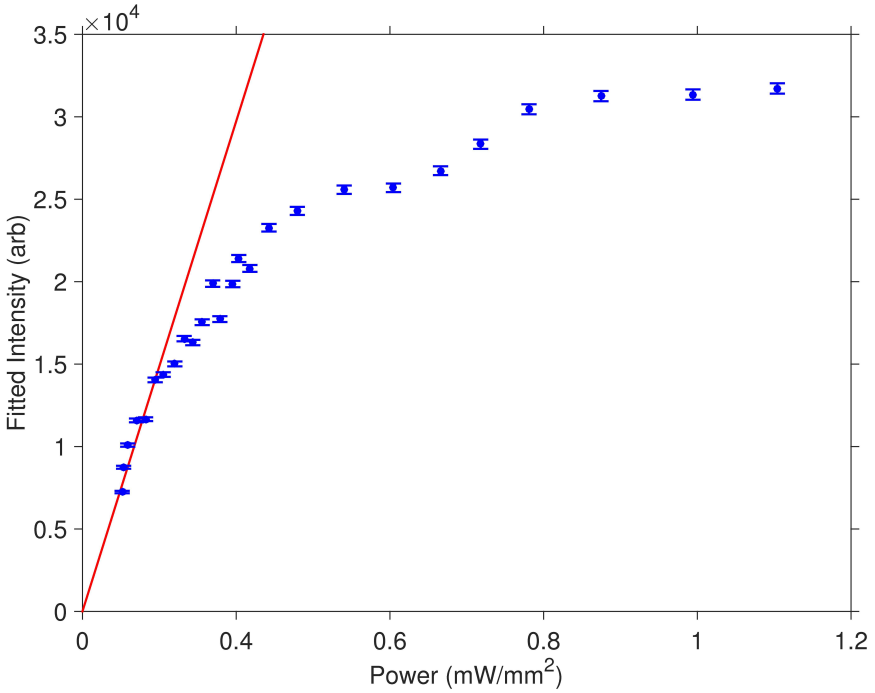

Figure 3.18: Incident power dependence on the fitted Raman intensity of the B mode appearing in HgTe@SWCNTs at 4K using incident laser wavelength of 702nm (blue dots). The red trace is a simple linear fit, forced through zero, to the fitted intensity up to 0.2mW. A range of data was tried to apply the linear fit between to give the best fit, it was found that 0.2mW was marginally the best. The error bars in the data correspond 95% confidence intervals of the fitted Lortentzian.

100K and 150K non-linear effects began to dominant at powers in excess of 0.2mW. In the case of 225K and 295K since the sample was at higher temperature non-linear effects began to dominate at ∼10mW. For this reason, when performing temperature dependant measurements, the incident power was kept at a constant 0.1mW for sample temperatures between 4-150K, for temperatures above 225K it was found that 0.1mW was too low to obtain a measurable signal and for this reason the incident power was chosen to be 1mW. Because the sample temperatures were probed in the linear regime in all cases, it was possible to normalise the results to their respective power to allow for direct comparison.

3.3.2 Measuring Repeatability

The work done in this thesis reports mainly on strong resonant effects in extreme nanowires. To understand the energy dependence of the Raman scattering cross-section it is important that any change in absolute intensity due to experimental variation is minimised. There are many aspects of the experiment that can effect the noise seen in the intensity. This section will discuss through the possible sources of noise in the Raman

system, how the noise was quantified, and subsequently minimised.
It was thought that there were two main sources of variation in intensity. These were 1) misalignment of the laser during change of the wavelength and 2) changes in the focusing volume between Raman spectra. In the case of 1) small variations in the alignment would cause not only the laser to probe a different sample spot, but also change the way the light was incident on the coupling lens and therein change where the Raman light was incident on the gratings and CCD. With regards to 2) the choice of focal position not only changes the sampling volume, but also changes the intensity of the Raman scattered signal. This is demonstrated in figure 3.19, which presents the Raman intensity of the silicon mode as a function of discrete (2μm) changes in the focal depth of the sample. The data was fit to an arbitrary Gaussian line shape, and it can be seen by the data presented in the fit from figure 3.19 that a repositioning error of 10μm either side of the focal point would cause an 8% variation in the signal intensity (comparable to the repeatability measurements). Considering the actuators can be positioned to well within

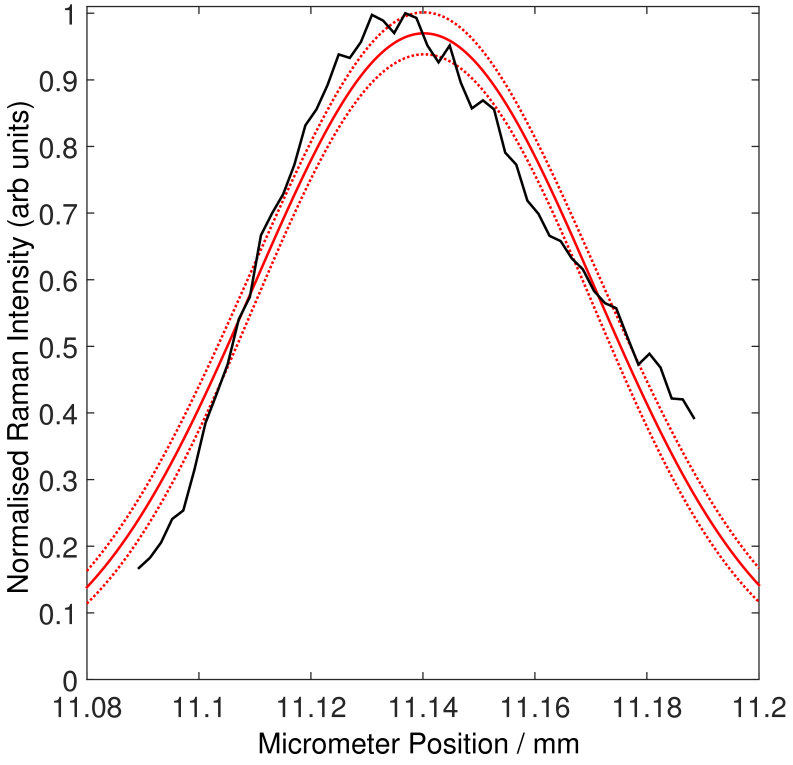

Figure 3.19: Fitted Raman intensity of the silicon mode, normalised to the maximum intensity recorded, as a function of 2μm changes in the position of the sample through the focusing volume of the laser. Also on the plot is a Gaussian fit to the trace, along with the 95% confidence bands of the fit.

10μm, it seems unlikely this is the source of error. As in fact, if the limits of the focusing are associated with the 1μm backlash of the actuators, this would lead to <0.5% variation in the intensity either side of the maximum. The technique of adjusting the lateral depth of the sample through the focal point of the laser, monitoring the reflected power

of the retroreflected light and acquiring the Raman spectra where the reflected power was maximised, was chosen for subsequent RRS.

In some resonance Raman experiments the variation in signal intensity from repeat measurements due to misalignment of the laser was found to be greater than 50% as seen in the top left hand panel of figure 3.20, which presents the peak intensity of one of the strongly resonant Raman modes observed in HgTe@SWCNTs. This variation was

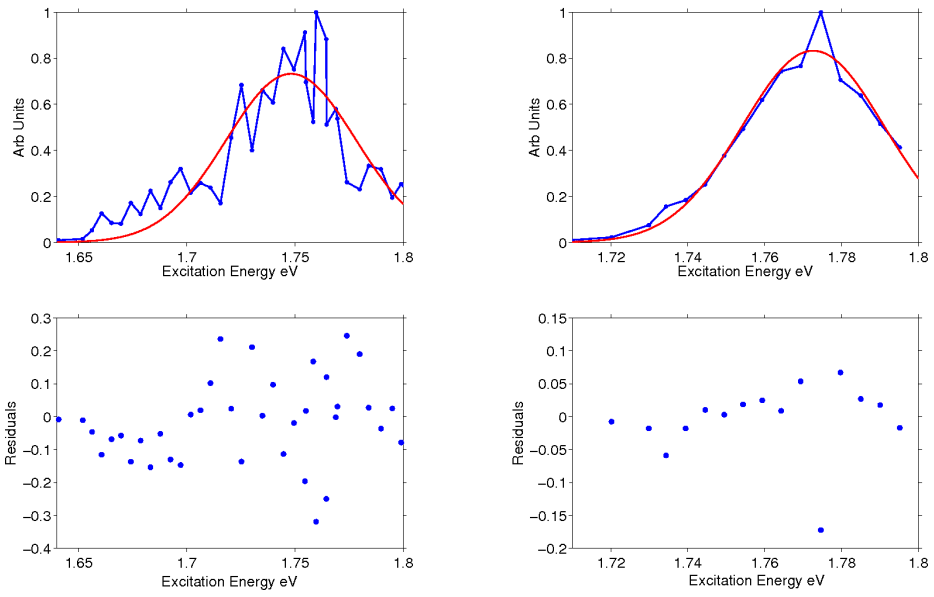

Figure 3.20: A comparison of the RRS experiments performed before the system depicted in 3.5 was developed (left column) and after it was developed (right column).

reduced significantly by the addition of two observation cameras (C1 and C2) to monitor the optical path (figure 3.5). These cameras proved integral to achieving highly repeatable Raman spectra. This is demonstrated in figure 3.21, where the figure presents data of multiple independent spectra of the HgTe@SWCNTs taken using the same excitation energy after deliberate misalignment then realignment.

It can be seen in figure 3.21 the data shows little variation between the multiple spectra, and by picking the peak value of the 52cm^{-1} feature in the inset, the variation (repeatability) was determined to be 8%, as calculated by dividing the standard deviation by the mean. This notable improvement in the repeatability of the Raman spectra is also highlighted by direct comparison of the resonance Raman data taken using the optimised realignment procedure (right hand panel of figure 3.20) against the suboptimal data set (left panel of fig 3.20).

Another example of noise that was apparent during data acquisition were fluctuations in the laser intensity over time during a spectral acquisition. Usually Raman spectra are taken over a 30 second period, which means that any fluctuations in incident power over a short time period would ideally average out, however a systematic change in power over a 30 second period could significantly alter the light intensity on the CCD. Even

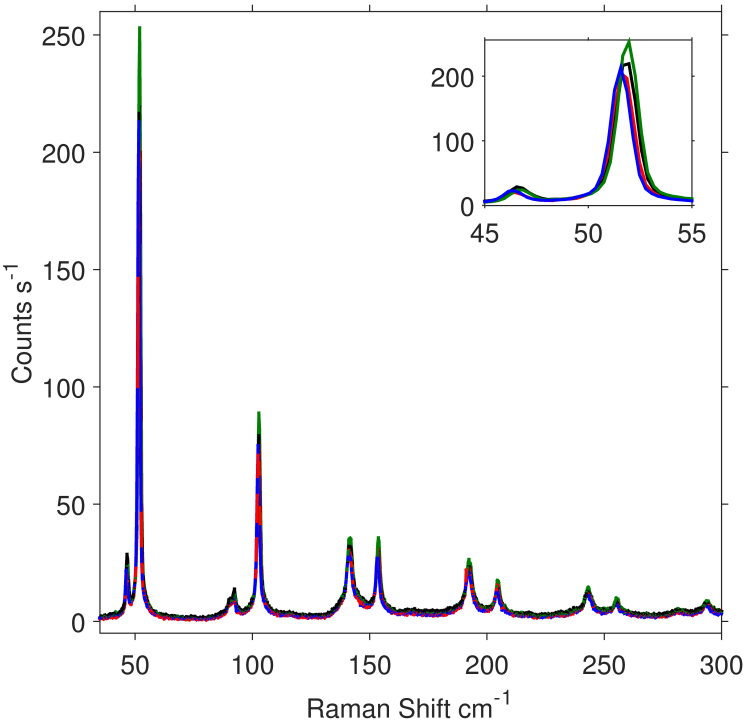

Figure 3.21: 4 independent repeats measured on the same sample position after realigning the laser system during a resonance Raman experiment at 4K.

though no long term drift in power was observed over time, at least not in the time frame of a spectral acquisition, the variation in power over multiple Raman measurements was recorded to understand how this contributes to the noise. The incident power was set to 2mW and a Raman spectra of silicon acquired over a 30 second time period. A DAQ recorded the power at a sampling rate of 100Hz for the 30 second period. This was repeated multiple times. A representative sample of the incident power (2mW) recorded as a function of time is shown in figure 3.22. By analysis of the data presented in figure 3.22, the mean output voltage, which is linear with the power was 1.32V, and the standard error 0.0033. The variation in incident power over time was also recorded at various other defined input powers between 100μW and 10mW. The mean and standard error was calculated at each power, and the average of all the standard errors was calculated to be 0.0089. From this, we can conclude that fluctuations in the power may play a small role in the limits of repeatability, however, it is not possible to state the power fluctuations alone are the limiting factor on repeatability considering the variation in power is about 10 times less than the variation in the intensity of Raman spectra on multiple repeat measurements. Whilst it is possible to record the power over time and normalise each spectra with respect to the average power over time, it is not clear whether this will remove the noise associated with variations in the power, as it is inherently random it could compound the noise increasing the uncertainty.

Another prevalent source of error, and one most likely to effect repeatability is homogeneity of sample environment. The nanotubes are inherently randomly distributed in

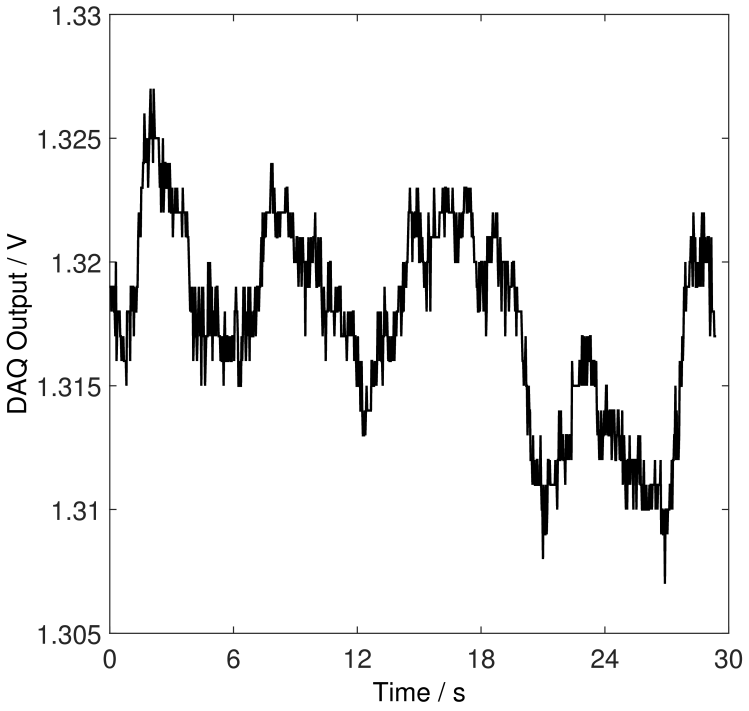

Figure 3.22: Recorded output voltage of power meter over a 30 second period of time with 2mW incident on the power meter head.

nature, which means that on a sample of nanotubes a variety of conformations of tubes are available, and there is likely to be changes in the filling fraction of tubes in a sample area. The laser spot used to probe the nanotubes is around 3μm, and the accuracy of repositioning the sample is ∼500nm or around 16% of the spot size, which in principle, if on a particularly inhomogeneous sample area would lead to variations in the Raman intensity on this order. This effect was minimised by deliberately choosing a sample spot that was homogeneous over a large (at least 5μm) area. Once such a spot was located through trial and error, the relative sample coordinates were recorded with respect to an obvious feature on the sample substrate i.e. the edge of the silicon chip. The homogeneity of the sample area chosen was checked at room temperature and 4K, where it was found there was no clear change in the homogeneity of the sample spot. This indicated that the spot chosen was not only spatially homogeneous, but retained this characteristic at the extremes of sample temperatures.

Overall, there are a number of possible sources of variation and error that will limit the repeatability of the Raman spectra, however, it is not possible to eliminate random noise by normalising it out, as it could compound the error. It has been demonstrated that thinking about possible sources of error and taking sensible measures to reduce the noise has improved the repeatability of the system to around ∼8% for independent Raman spectra acquired under the same conditions [8].

3.4 Fitting Procedure

This section outlines the procedure used for fitting the observed peaks, and resonances to quantify the parameters of peak width, Raman shift, resonance width, energy and Raman scattering cross-section of the observed features in the Raman spectra. In general, it is expected from theory [137] the Raman modes should fit well to a Lorentzian line shape. However, in practice this is not always the case as inhomogeneous broadening, or resolution limitations can complicate the lineshape of the peaks [4]. The resonances of the Raman modes are further complicated as any variation in the coherent lifetime between the intermediate states can also affect the lineshape [166]. Despite these possible limitations on the Lorentzian line fitting to the observed peaks, it was found that in general the features fit well to this line shape and multiple phenomenological fits were applied, such as a Gaussian, or Lorentzian squared or Voigt, it was found the Lorentzian was marginally the best fit.

3.4.1 Fitting Raman Peaks

The fitting procedure used in Matlab was based upon a least square regression algorithm, the model applied to fit the spectra was a linear combination of a number of Lorentzian lineshapes equal to the amount of features being fit. A linear background of $p_0 + p_1 x$ was also applied to the fits. The overall model for the fitting is shown in equation 3.2;

$$f(x, p_0, p_1, a_1, \Gamma_1, c_1 ....a_n, \Gamma_n, c_n) = (p_0 x + p_1 x) + \sum_{i=1}^{n} a_i \frac{\Gamma_i^2}{(x - c_i)^2 + \Gamma_i^2} \tag{3.2}$$

where Γ is the width of the lineshape, c is the central position and a is a fitting parameter to scale the amplitude and n is the number of lineshapes applied to the fit. It was found, in general that simultaneously fitting to all of the observed features (as seen in figure 3.23) although possible, was often difficult and produced poorer quality fits. To overcome this limitation the number of modes fit in any spectral window was limited to around two, and each set of peaks were fit individually. It can be seen by the data presented in figure 3.23 that the Lorentzian lineshapes (red trace) is a reasonable fit to the Raman spectrum (black trace). The bottom half of figure 3.23 shows the residuals of the fit, and it can be seen whilst not perfect, as there are some large differentials in the data points near the Raman peaks, the absolute value of the residuals for each peak is far less than the magnitude of the peak itself ($\sim$7% in the case of the second peak).

3.4.2 Fitting Resonances

Fitting to the resonances observed in this thesis is not as trivial, there are many possible fits, and theories that dictate what the optimum fit should be. In most cases when

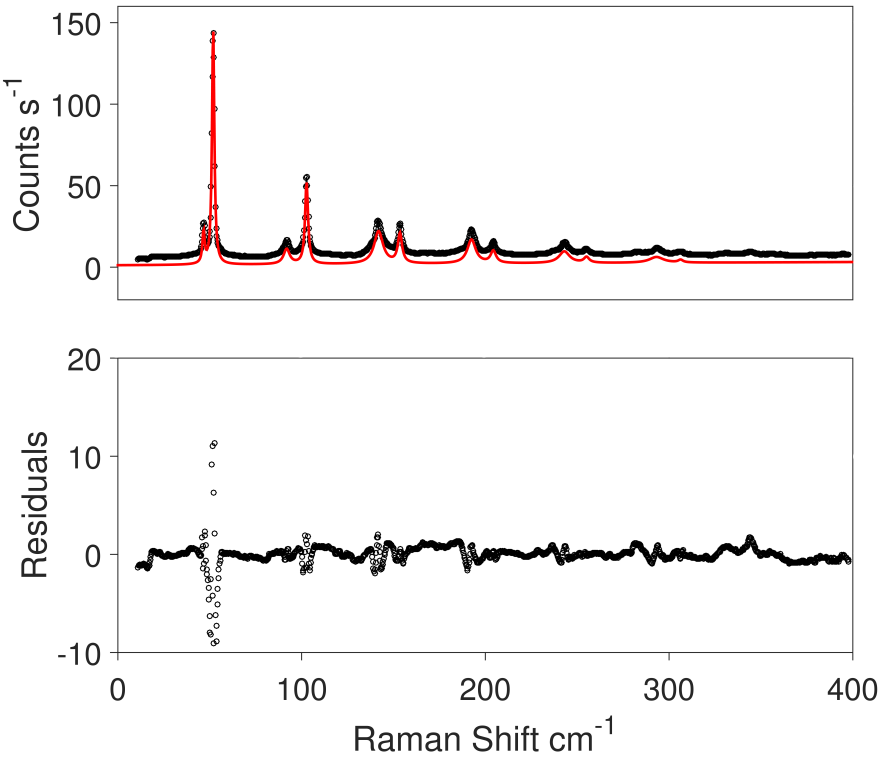

Figure 3.23: Representative Raman spectra of HgTe@SWCNTs measured at 4K, using 702nm incident laser wavelength. Top panel shows Raman spectra (black) and Lorentzian fits to observed modes up to 6^{th} order. The bottom panel shows the residuals of this fit.

resonance at a fundamental vibrational mode, the fit should be some combination of a Lorentzian centred at the resonance energy multiplied by a Lorentzian at the resonance energy shifted by the phonon energy. For purposes of chapter 4, the exact form of the resonances are not strictly relevant, as this chapter focuses on reporting them for the first time. For this reason the resonances are fit to simple Gaussian lineshapes to extract peak parameters. The true form of the resonances become more important in chapter 5 where the coherent lifetime of the underlying states involved in the Raman process is studied.

For data acquired in chapter 5 multiple fits were attempted to understand the form of the resonance and the dynamics of the linewidth as a function of temperature. The data was fit to Gaussian, Lorentzians, and higher-order Lorentzians for resonances of the harmonics. After a extensive review of the underlying theory of multiphonon Raman scattering [137] it was found that the most appropriate lineshape would be a modified double Lorentzian fit of the form;

$$f(x, A, \Gamma, c, p) = \frac{A}{\left((x-c)^2 + \Gamma^2\right)\left((x-p-c)^2 + \Gamma^2\right)} \tag{3.3}$$

where A is an amplitude fitting parameter and p corresponds to the energy of the phonon involved in the emission process, which is measured by fitting a Lorentzian lineshape to a Raman peak. Equation 3.3, was applied to all the resonances observed, however, further attempts were made with multiphonon Raman, to understand the emission process in terms of sequential or simultaneous emission. This means the fits for the resonances of the harmonics were different from equation 3.3. In the case of simultaneous multiphonon Raman the only change to eq 3.3 was a change in the phonon energy, p. However, in the case of sequential Raman, where phonons are emitted in subsequent electronic scattering events an extra term in the denominator was added, which, for 2-phonon scattering yields;

$$f(x, A, \Gamma, c, p, p2) = \frac{A}{\left((x-c)^2+\Gamma^2\right)\left((x-p-c)^2+\Gamma^2\right)\left((x-p2-c)^2+\Gamma^2\right)} \tag{3.4}$$

where p2 corresponds to the fitted energy of the 1^{st} overtone. The rule can generalised that for sequential emission, the higher harmonics will have an extra $\left((x-p_n-c)^2-\Gamma^2\right)$ term in the denominator, with p_n being the appropriate the energy of the phonon.
All fits were performed using a least-squared fitting routine in Matlab, outputting all the fit parameters and the 95% confidence bounds of the fit. The distinction between the various fits applied and which peaks they should be applied to will become more apparent later in the thesis.

3.5 Resonance Raman Spectroscopy Experiments

As stated the key technique applied in this thesis is RRS (resonance Raman spectroscopy). This section will detail how RRS and other experiments in chapters 4-5 were performed and the conditions used to acquire the results.
In chapter 4 RRS experiments were performed on a sample of HgTe@SWCNTs prepared in the way as discussed earlier, under vacuum and at cryogenic temperatures (4K). The laser used was the Mira-900p in the energy range 1.7-1.8eV in 5meV steps. Control experiments on bulk HgTe and unfilled SWCNTs were performed at a single excitation energy of 1.77eV, and RRS experiments were also performed on the unfilled SWCNTs at 4K in the energy range 1.4-1.9eV in 10meV steps. In the case of the filled SWCNTs it was necessary to use both the VBG and LLTF to acquire a full resonance profile of the filling modes. An overlap area of 5 data points between 702-712nm was taken using the VBG system and it was found that at 4K, the Raman intensity of the peaks for the VBG data was consistently less than the LLTF equivalent. This is likely due to a change in spot size when the VBG was used due to the collimation optics. To correct for this, the ratio between the overlapping data points was calculated and the VBG data scaled by the mean of these values.

Polarisation dependant data was collected in chapter 4 to determine if the Raman features were indicative of nanowires structures. The system was changed in accordance with the purple dashed line in figure 3.5, by the addition of broadband half-wave plate and linear polariser prior to the objective, and another linear polariser prior to the half-waveplate and lens before the spectrometer. The incident wavelength was set to 1.776eV and the desired input polarisation was set to either vertical or horizontal with respect to the lab bench using Pol3 and HWP3 3.5) the Raman spectra measured as a function of 10° changes in the polarised (Pol2) with the input half-wave plate (HWP) rotated in 5° to correct for the spectrometer polarisation dependence.

In chapter 5 we report on temperature dependant RRS experiments on the sample spot of filled HgTe SWCNTs. The RRS experiments were performed in the same way as with those presented in chapter, with the addition that RRS experiments were repeated at sample temperatures of 4, 25, 50, 100, 150, 225 and 295K. The sample temperature was controlled in the way as discussed in section 3.2.2, and at each temperature initial checks were performed to ensure the incident power was in the linear regime, as discussed in section 3.3.1. Incident power was set to 0.1mW in the temperature ranges 4K-150K, and 1mW for 225 and 295K, it was demonstrated that the intensity dependence of the power was in the linear regime for both these powers at the temperatures.

Chapter 4

4K Resonance Raman Spectra of HgTe Extreme Nanowires

4.1 Motivation

The central pore of SWCNTs allows for the encapsulation of inorganic materials forming nanowires with diameters on the order of the unit cell [90, 167]. In SWCNTs of appropriate diameter (between 0.8-1.6nm) it has been shown that the encapsulated material can form unique metastable crystalline structures not found in the bulk form, or larger nanoscale forms of the same material [168, 5, 1].

A technique that has made a huge contribution to the study of SWCNTs is Raman scattering [169]. Specifically Resonance Raman Spectroscopy has proved to be a powerful tool for providing information about the electronic structure [126] and allowed for assignment of diameter and structure [119, 170, 171] on both bundled [163] and individual tubes [31]. In addition it allows for selective studying of SWCNTs of a particular type through resonant excitation [152, 162].

For filled SWCNTs, RRS can provide a rapid, non-destructive technique for characterising the type of filling present in a CNT, as well as providing useful information about the host tube. Despite this, the application of Raman scattering to filled tubes has been relatively limited. So far the main bodies of work on filled tubes have focused on the effects of filling on the nanotube host [34, 172, 36, 102].

This chapter presents the results from resonance Raman spectroscopy experiments on HgTe filled SWCNTs, which reveals information about the vibrational modes and electronic transition states of such extreme nanowires, and the effects of filling on the well-defined nanotube Raman modes. The main results of this chapter are illustrated in figure 4.1, where we can see that in the sample of HgTe@SWCNTs we observe many strongly resonant peaks in the Raman spectrum that, upon detailed analysis, we assign to be due to 4 fundamental vibrational modes of a HgTe nanowire embedded within the

nanotube. The remainder of this chapter will present the data and discuss the physics and implications of the key results that lead us to this conclusion.

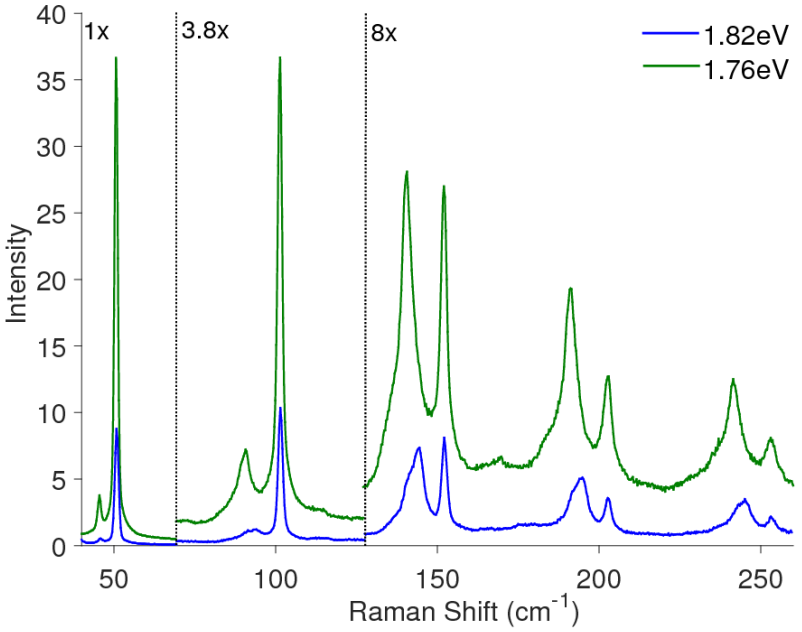

Figure 4.1: Representative Raman spectra of HgTe filled SWCNTs acquired at two laser excitation energies (1.82 and 1.76eV). Portions of the spectra have been separated and scaled by arbitrary factors for ease of visualisation for the higher energy peaks.

This work is based on a 2014 publication [1], where we set out, for the first time, new Raman modes of HgTe extreme nanowires within a nanotube. It is important to note that since the publication of the paper in 2014, a lot of work has gone into improving the experimental system as detailed in chapter 3. The data presented in this thesis is the optimised low temperature resonance Raman data collected subsequently to the publication. The improved data set does not have any impact on the conclusions drawn from the publication, and gives better insight as to the resonance behaviour of the observed modes.

4.2 Experimental Details

This section details the excitation range and sample condition for both resonance Raman spectroscopy and polarisation dependant Raman spectroscopy experiments. A detailed discussion on the apparatus and experimental techniques is presented in chapter 3.
Resonance Raman spectroscopy (RRS) experiments were performed on a sample of HgTe filled SWCNTs, drop-cast on a Si/SiO_2, to understand the excitation energy dependence of the Raman shift, line width and scattering cross-section for particular Raman features observed. The sample was held at 4K in a cryostat and Raman spectra was taken between the energy range 1.7-1.8eV in 5meV steps. Equivalent samples of unfilled SWCNTs

were measured in the energy range 1.4 to 1.8eV in 10meV steps. Raman spectra of bulk HgTe was acquired at room temperature using a single excitation energy of 1.77eV. Polarisation dependant Raman spectra was collected by exciting the sample with a constant incident excitation energy (1.77eV) and by setting the incident polarisation to either s- or p-polarised light at normal incidence to the sample. An analyser was added to the setup and Raman spectra was collected as a function of discrete (10°) steps of the analyser, at each analyser angle the half-wave plate was also rotated accordingly to maintain the polarisation input to the spectrometer to counteract the grating efficiency dependence on polarisation.

4.3 Raman Spectra of Control Samples

This section will detail the representative Raman spectra acquired from bulk HgTe and unfilled SWCNTs to directly compare to the peaks observed in the spectra illustrated in figure 4.1, and subsequent resonance Raman data. It will also discuss representative data through external literature of nanoscale equivalent forms of HgTe, namely HgTe quantum dots and related structures. Figure 4.2 shows the Raman spectra obtained for a sample of bulk HgTe and a sample of unfilled SWCNTs, both acquired at room temperature / pressure using 1.77eV excitation energy. The blue trace in the figure shows four distinct Raman peaks, labelled at 89, 118, 137 and 261cm^{-1}. The position of these peaks is in good agreement with other measured and predicted phonon modes of bulk zinc-blend HgTe [173, 174]. It has been reported [175], that these phonons do have a resonant enhancement near the E_1 gap at ∼2.24eV.

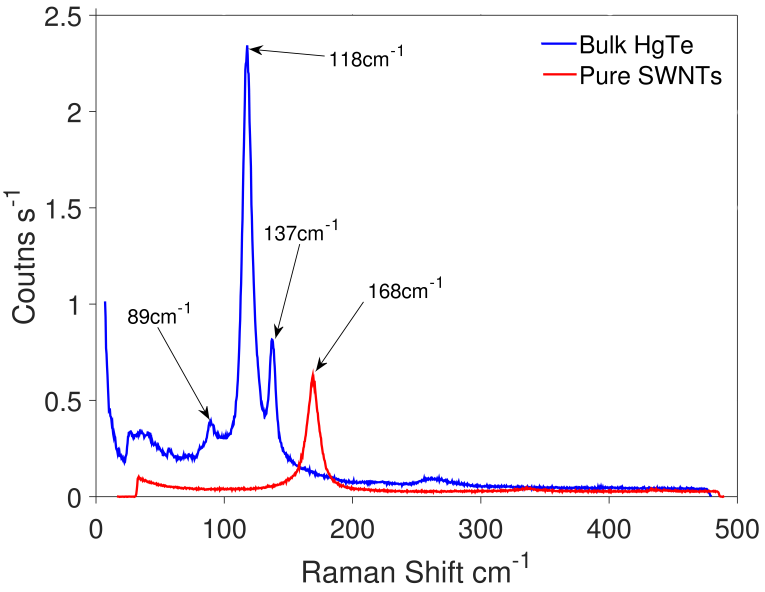

Figure 4.2: Raman spectra of bulk Mercury Telluride (blue trace) and an unfilled SWCNT (red trace). Both spectra were taken under ambient conditions using 1.77eV excitation energy.

Although not experimentally verified in this thesis, there have been some Raman studies into ∼2nm quantum dots of HgTe [5] and other related colloidal semiconductors eg CdTe [6] (Figure 4.3). The results of which show that new Raman modes, attributed to the confined acoustic modes, zone edge phonons and surface optical phonons do occur. However, even for the smallest diameter nanostructured quantum dot, the Raman spectra are still dominated by the LO phonons appearing in the bulk for both materials.

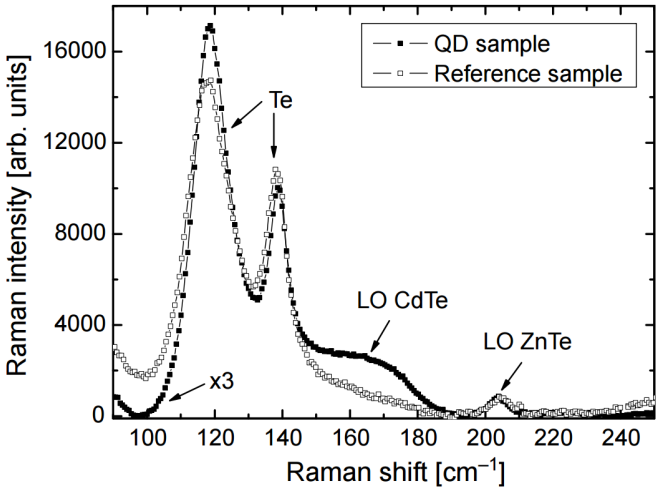

Figure 4.3: Representative spectra from CdTe quantum dots and equivalent bulk scale CdTe. Image from [6]. It is clear that in this 6 layer stack of quantum dots, the dominant features in the Raman are unmodified from the bulk, with the additions of an LO phonon at ∼160cm^{-1}.

The red trace from figure 4.2 shows a spectra of unfilled SWCNTs from the Krestinin source[157] (referred to as Russian tubes), the only observable feature in this trace is labelled at 168cm^{-1} and as detailed later in table 4.1, is likely to correspond to a radial breathing mode (RBM) of a (12,9) nanotube, 1.45nm in diameter that has a resonance of 1.683eV. It is likely that because of inhomogeneity, the sample consists of a distribution of RBMs that resonate at different energies [4]. Because of this it is important to understand the resonance behaviour of the unfilled nanotubes, to assign all observable RBMs to avoid confusion with labelling the peaks observed in the filled samples. By inspection of figure 4.4, the only observable features in the same excitation energy range as the filled tubes (1.7-1.8eV) are between 100-200cm^{-1} and are likely to be associated with RBMs of the nanotubes. By fitting the RBMs to simple Lorentzian lineshapes it is possible to determine nanotube conformation and diameter [170]. In the spectral range measured for the filled nanotubes (1.7-1.8eV), there were 4 RBMs observable in the unfilled equivalent for the same energy range. After a review of the literature, the best assignments, based upon experimental observations or calculations using the tight-binding approximation for the modes are shown in table 4.1. Whilst there are in principle other possible assignments of nanotube conformation and resonant energy, for example if the resonance is associated with another transition i.e $E_{3,3}$ [4, 60], the assignments presented in table 4.1 are chosen as they are the most likely assignment.

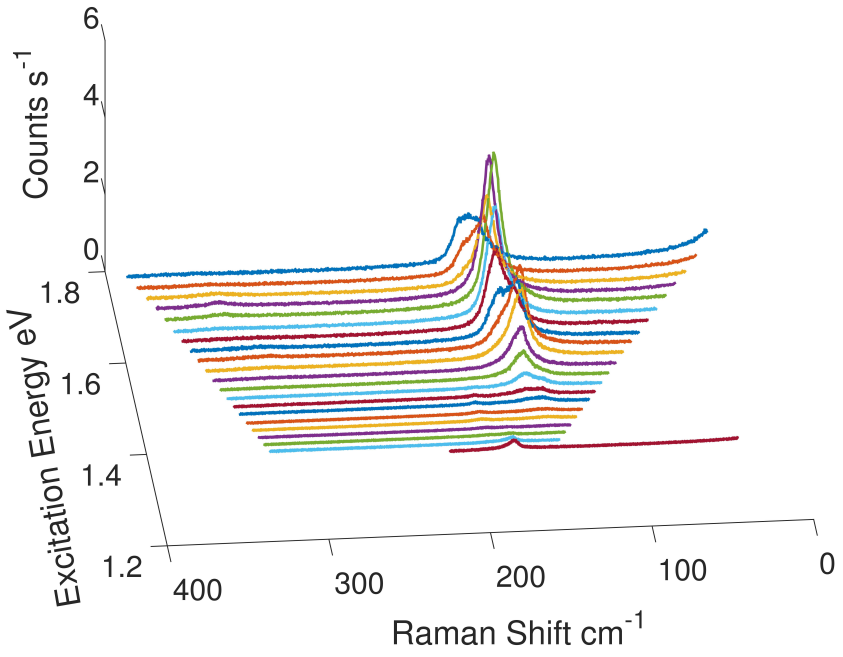

Figure 4.4: Resonance Raman spectra of "Russian" unfilled SWCNTs between 1.4 and 1.8eV.

This system		External observations				Ref
RBM (cm^{-1})	Fitted Energy (eV)	RBM (cm^{-1})	Transition Energy (eV)	(n,m) index	Diameter (nm)	
148 ± 2.1	1.510 ± 0.13	148	1.51	(15,9)	1.67	[119]
158 ± 1.9	1.587 ± 0.06	158	1.52^1,1.67^2	$(18,3)^1$,$(14,8)^2$	1.56^1,1.51^2	^{1}[119] / ^{2}[176]
168 ± 2.7	1.683 ± 0.04	167	1.67^1,1.73^2	$(12,9)^1$,$(18,0)^2$	1.45^1,1.41^2	^{1}[170],^{2}[176]
177 ± 2.3	1.98 ± 0.56	176	1.83	(18,0)	1.43	[119]

Table 4.1: Table showing possible RBM assignments based on the observed Raman shifts, and resonance energies of the nanotubes probed in the experiment. In the case of some of the observations by other sources, multiple resonances and assignments can be made, this is highlighted by the superscript and cross-referenced accordingly.

4.4 Results from RRS experiments on HgTe@SWCNTs

This sections presents the results from resonance Raman characterisation of a sample of HgTe@SWCNTs at 4K. It will discuss the results obtained in comparison to the constituent components of the sample (i.e. bulk HgTe and SWCNTs) and through fitting, assign labels to all the peaks observed and present the evidence that the higher order peaks could be harmonics and combinations of lower energy peaks. It will then present the results from high resolution resonance Raman spectroscopy experiments to understand the excitation energy dependence on the Raman shift, width and intensity of the peaks. Polarisation dependent data is presented to support the claim that the peaks are due to a nanowire like structure. Finally, the section discusses how when the data

presented is coupled with HRTEM and density functional theory (DFT); it supports the hypothesis that the peaks observed are most likely due to vibrational modes of a novel structure of HgTe.

Figure 4.5 shows the data collected for a sequence of representative Raman spectra of the HgTe@SWCNT sample (Russian tubes) acquired at 4K using incident laser excitation energies of a) 1.81eV, b) 1.76eV, c) 1.73eV and d)1.67eV, with all observable peaks assigned a label in numerical order (panel a). The intensity (y-axis) of each subfigure has been converted to a log scale for ease of viewing the weaker, higher energy peaks. Inspection of figure 4.5 clearly shows significant differences in the Raman spectra to that from the data presented in figure 4.2. The most striking difference is the appearance of multiple Raman peaks not coinciding with shifts of the bulk material or unfilled SWCNTs. There is no direct evidence from the data presented in figure 4.5 that the peaks observed are due to bulk HgTe. The other obvious feature with regard to each trace in figure 4.5 is what appears to be harmonics in the data, as apparent by a visual periodicity in the Raman spectra, which decrease in intensity at higher Raman shifts. Finally, it is apparent that the most of the peaks are strongly resonant at ∼1.76eV excitation energy (panel b), and drop off in intensity by more than an order of magnitude by shifting the excitation energy 90meV (panel d).

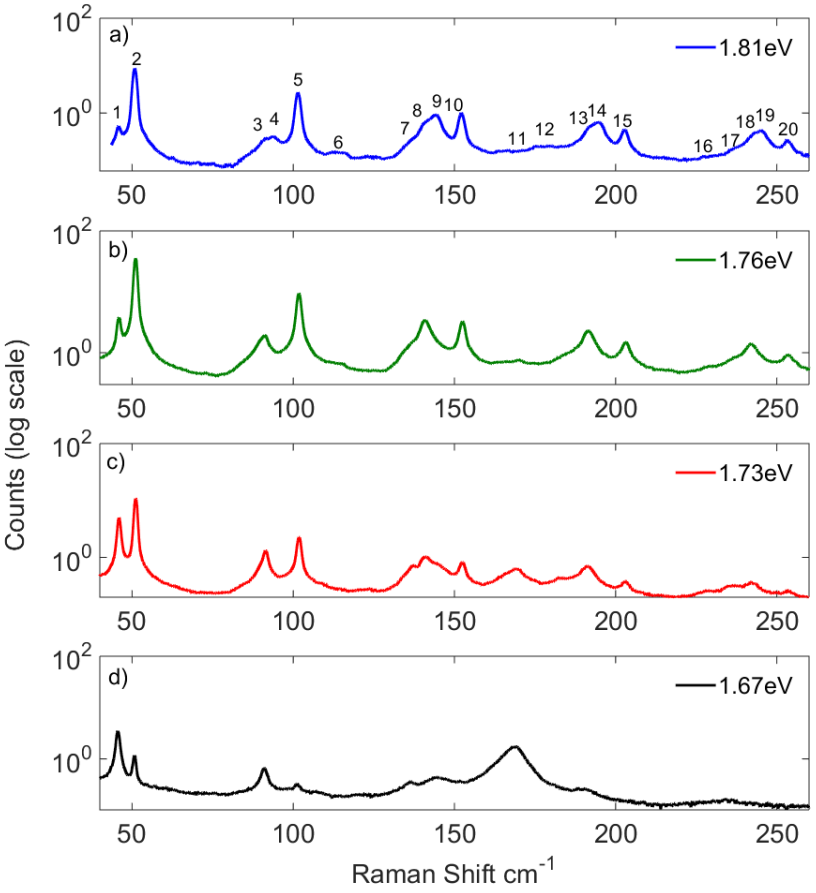

Figure 4.5: Representative Raman spectra of bundled HgTe filled SWCNTs on a Si/SiO_2 measured at 4K using multiple excitation energies.

4.4.1 Discussion and Assignment of Peak Labels

In order to better understand the features observed in figure 4.5, each peak at each of the four excitation energies were fitted to Lorentzian lineshapes (section 3.4). This allowed for direct comparison to the peaks observed in figure 4.2, and the possibility of labelling the peaks in terms of harmonics. Each observable peak was given a numerical assignment from low to high energy as illustrated in figure 4.5, and each peak fitted at the four excitation energies to determine the mean Raman shift and standard deviation. The result of this fitting process is presented in table 4.2.

Ref Label	Raman Shift (cm^{-1})
1	45.79 ± 0.17
2	50.94 ± 0.20
3	91.07 ± 0.17
4	94.49 ± 1.00
5	101.55 ± 0.33
6	113.82 ± 0.48
7	136.57 ± 0.43
8	141.22 ± 0.52
9	144.57 ± 0.27
10	152.55 ± 0.33
11	167.17 ± 2.80
12	175.50 ± 1.87
13	184.53 ± 1.00
14	191.57 ± 0.37
15	195.93 ± 0.95
16	202.96 ± 0.15
17	235.47 ± 0.81
18	242.63 ± 0.72
19	244.70 ± 0.60
20	253.03 ± 0.10

Table 4.2: Table showing the mean Raman shift of each observed peak in figure 4.5. The errors in the fitted peak corresponds to the standard deviation of multiple fits.

Upon inspection of table 4.2, and comparing the observed peaks to those shown in table 4.9 and the peaks presented in figure 4.2, it is clear that two of the peaks in figure 4.5 (peak 11 and 12) at 167.17 and 175.5cm^{-1} coincide (to within errors) with two RBMs at 168 and 177cm^{-1}. It is clear that the 167.17cm^{-1} feature becomes strongly resonant at 1.67eV (panel d of figure 4.5), which is contrary to the resonance of the majority of the other peaks observed in figure 4.5. Furthermore the observed resonance effect at 1.67eV is inline with the expected resonance for this RBM. From this, it is reasonable to assume that peaks 11 and 12 from table 4.2 are likely Raman peaks associated with SWCNTs. It is not immediately obvious that the other RBM peaks (148 and 158cm^{-1}) from the unfilled SWCNT appear in any of the spectra from figure 4.5. However, the RBMs at 148 and 158cm^{-1} are not resonant at any of the excitation energies presented

in figure 4.5, in addition the Raman shift of these features may be hidden within the tail of the intense peaks labelled 9 and 10 at 144.5 and 152.5cm^{-1}. The peak at 136.57cm^{-1} from figure 4.5 (labelled peak 7) appears to coincide with the 137cm^{-1} feature of the bulk HgTe, however the two other bulk HgTe Raman features (89 and 118cm^{-1}) are not observed in figure 4.5.

4.4.1.1 Labelling of Harmonics

Now the peaks that appear in the control sample have been dealt with, we are in a position to discuss the other peaks that are observed in the Raman spectra of HgTe@SWCNTs. Visually it seems likely that the higher energy peaks are harmonics of some or all the low-energy peaks. This is further supported by inspection of the fitted data presented in table 4.2. To understand the harmonics we first re-label the 2 lowest energy peaks at 45.79cm^{-1} and 50.94cm^{-1} as A and B respectively (table 4.3). If the higher order peaks in the Raman spectra are harmonics they will likely obey a pattern of nA or nB where n is the harmonic order.

By use of the tabulated peak positions (table 4.2) it seems likely that peaks 5, 10, 16 and 20 at 101.55, 152.55, 202.96 and 253.03cm^{-1} are harmonics of the 50.94cm^{-1} (B) peak. These peaks, and the fundamental, B, are plotted in figure 4.6 as a function of harmonic order, n, and fit to a straight line $mx+c$. It can be seen by the data presented in panel b of figure 4.6, that there is a near-perfect linear relationship with these peaks as a function of n. The straight line fit yielded a gradient of 50.7 $\pm$0.3cm^{-1}, which corresponds (to within uncertainty) to the fundamental peak labelled B. The y-intercept of the line was at 0.52$\pm$0.32cm^{-1} and if consistent with subsequent fits, will likely correspond to a systematic error in the Raman spectra, which can be corrected for by this value. This relationship now allows us to relabel peaks 5, 10, 16 and 20 as 2B, 3B, 4B and 5B respectively (table 4.3).

By applying the same logic as used in the assignment of the nB peaks, it seems likely that peaks 3, 7 and 13 at 91.07, 136.57 and 184.53cm^{-1} from table 4.2, follow the pattern nA. Again, these peaks (along with A) were plotted as a function of harmonic order. From the data presented in panel a of figure 4.6 it can be seen that these peaks fit well to a straight line with a gradient of 46.42 $\pm$1.2cm^{-1}, which corresponds to the A peak at 45.79cm^{-1}, to within the confidence bands of the fit, as expected by the hypothesis. The y-intercept for this line was -0.94$\pm$4.31cm^{-1}, which because of the large uncertainty in the fitting, does fall within the error for the same offset as the B peaks. It can be seen that the hypothesised 4^{th} order peak labelled 13 at 184.53cm^{-1} is slightly higher than what the expected 4A peak would be (183.16cm^{-1}), by more than the uncertainty of peak 13. If this peak is ignored within the fitting process, the gradient of the fit to the remaining peaks is 45.39$\pm$2.21cm^{-1}, with an intercept of 0.36$\pm$1.17cm^{-1}. In both cases for fitting the y-intercept falls to within the error bands of certainty to be the same as the offset found for the B peak. Since the B harmonics are the more intense of all

the features, we will assume the offset calculated by fitting for the B peak is the more correct offset and will apply it to subsequent Raman spectra.
By the fitting of peak 7, it is apparent that it fits well to the 3A peak at 136.57cm^{-1}, but is also coincident with the 137cm^{-1} peak, corresponding to the LO phonon mode of bulk HgTe as mentioned earlier. It is possible that this is a coincidence, as there is no evidence for any other peaks of bulk HgTe in any of the Raman spectra and we will continue to work on the assumption that the 136.57cm^{-1} feature is the 2nd harmonic of A.

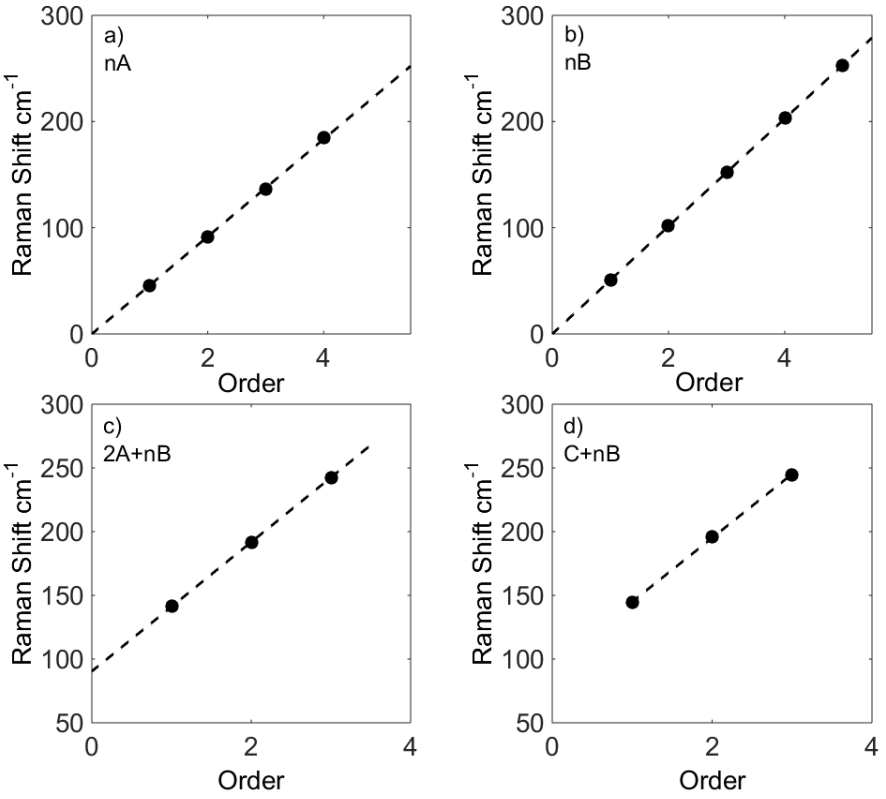

Figure 4.6: Figure showing all the peaks from table 4.2 that fit well to harmonics of (a) the 45.79cm^{-1} labelled A, (b) the 50.94cm^{-1} feature labelled B, (c) combinations following the pattern 2A+nB and (d) combinations following the pattern C+nB, where C is the 94.49cm^{-1} feature.

So far, by assuming the peaks to be harmonics of some fundamental peaks A and B (presented in panels a and b of figure 4.6), has allowed us to reliably label nine of the features observed in figure 4.5. An additional 2 peaks (11 and 12) from figure 4.5 can be understood as RBMs of the host tube. This leaves 9 peaks (94.49, 113.82, 141.22, 144.57, 191.57, 195.93, 235.47, 242.63 and 244.7cm^{-1}) that cannot be explained in terms of simple harmonics of the fundamentals A and B.
Now we move to re-labelling the 2 lowest energy peaks (94.49 and 113.82cm^{-1}) of the remaining 9 as C and D. However, unlike with the A and B case, none of the remaining 7 peaks can be explained simply as direct multiples of nC or nD. Inspection of the remaining peaks suggest that some of peaks could be based upon linear combinations

and multiples of the fundamentals i.e. A, B, C and D. Looking at the peak positions in table 4.2, it seems likely that the peaks at 8, 14 and possibly 18 (141.22, 191.57 and 242.63cm^{-1} respectively) follow the combination of 2A+nB. These peaks were also plotted as a function of n and the data is presented in panel c of figure 4.6. By fitting the 3 data points to a straight line of equation $mx+c$, which should correspond to nB+2A, we find the gradient of the line equal to 50.70±3.21cm^{-1}, which corresponds to the value of B, to within the error bounds, as expected. The y-intercept is 90.40±6.02cm^{-1}, which corresponds to 2A, as expected. Although in this case the confidence bounds are large, because only 3 data points are fit, it is still likely the pattern 2A+nB is valid for these peaks as the natural number of the fit is sufficiently close to the expected value.

It is also expected that the peaks at 144.57, 195.53 and possibly 244.70cm^{-1} follow the pattern C+nB. Again, through fitting the data (presented in panel d of figure 4.6) it can be seen that the peaks follow a linear trend as a function of order with a gradient of 50.06±6.29cm^{-1} and y-intercept of 94.8±10cm^{-1}. This natural values of the gradient and y-intercept fall very close to the B peak (50.94) and the C peak (94.8), as would be expected if the relationship C+nB were true.

This leaves 2 peaks, one labelled D at 113.82cm^{-1} and one at 235.47cm^{-1}. It was not possible to observe any harmonics or combinations involving the D peak. There were multiple possible assignments for the 235.74cm^{-1}, the closest possible assignment for the 235.47cm^{-1} feature would be a combination of the 2A+B (141.22±0.52cm^{-1}) peak with the C peak (94.49±1.00cm^{-1}), which would be at 235.71±1.12cm^{-1}, this is well within the error bounds to allow for this assignment.

Raman shift (cm^{-1})	Label
45.79 ± 0.17	A
50.94 ± 0.20	B
91.07 ± 0.17	2A
94.49 ± 1.00	C
101.55 ± 0.33	2B
113.82 ± 0.48	D
136.57 ± 0.43	3A
141.22 ± 0.52	2A+B
144.57 ± 0.27	C+B
152.55 ± 0.33	3B
167.17 ± 2.80	RBM
175.50 ± 1.87	RBM
184.53 ± 1.00	4A
191.57 ± 0.37	2A+2B
195.93 ± 0.95	C+2B
202.96 ± 0.15	4B
235.47 ± 0.81	2A+B+C
242.63 ± 0.72	2A+3B
244.70 ± 0.60	C+3B
253.03 ± 0.10	5B

Table 4.3: Table showing all the peaks observed in 4.5 with their best assignment of labels A, B, C and D based upon fitting appropriate harmonics and combination peaks.

From the direct inspection of fitted Raman shifts of peaks presented in table 4.2 it was possible to unambiguously assign all the peaks in terms of harmonics or combinations of the fundamental peaks A, B and C. A summary of the assignment of various peaks is given in table 4.3, and from now on we will refer to the peaks observed in the Raman spectrum as the labels given here. From this we can conclude that the peaks assigned in table 4.3 are the most likely the correct labels in terms of numerical multiples and combinations of the A, B and C peaks and that none of the features labelled A, B, C or D (except with the possibility of the 3A peak) appears in the bulk HgTe or the unfilled nanotubes.

4.4.2 Excitation Photon Energy Dependence of Raman Peaks

Now the features observed in figure 4.5 have been unambiguously assigned labels it is reasonable to move onto one of the most obvious features of the spectra; that is the strong excitation energy dependence on the intensity of the peaks. This section presents the results from RRS experiments on the HgTe@SWCNTs at 4K and the results of fitting to understand the effect of excitation energy on the Raman shift, linewidth and intensity of the peaks observed. For clarity, the pre-fit data is presented in figure 4.7 where it can

be seen there is a strong narrow resonance of all of the peaks.

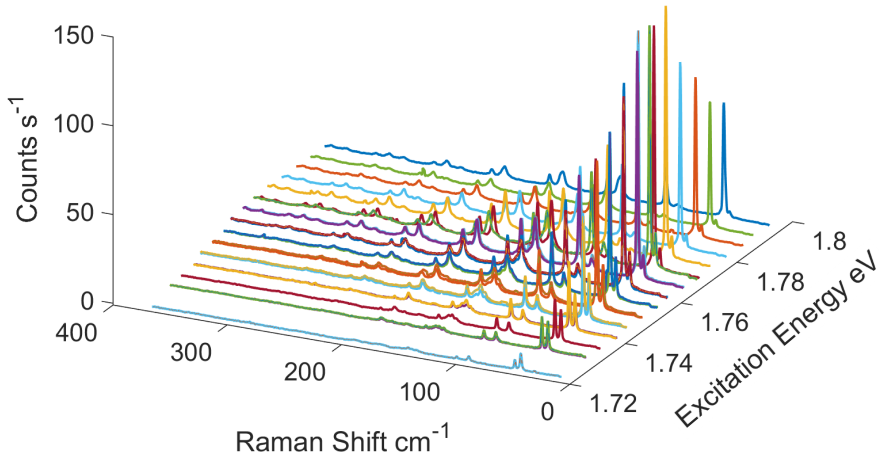

Figure 4.7: A 3D plot showing how the peaks observed vary with discrete changes in excitation energy. RRS measurements were taken at low temperature (4K) in the same sampling region throughout. The wavelength was typically varied by 2nm, with an overlap region of ∼20nm in the region where the volume Bragg grating filer was used.

There is an overlap region between the volume Bragg grating and the tunable laser line filter used in this experiment of roughly 5 data points, that do not vary by more than 8% which is well within the limits of the repeatability of the experiment. It is possible that in some situations a scaling factor needs to be applied to provide the best overlap between all the data points. Details on scaling data sets is discussed in chapter 3. Fitting (section 3.4) was applied in individual segments of each spectra as discussed and the peak data for both the volume Bragg grating (VBG) and data collected using the LLTF were saved in separate matrices, then spliced together in Matlab to give the full range and overlap region. The fit was applied up to the A, B, 2A, 2B, 2A+B and 3B peaks, the weaker C and D peaks, and the higher energy peaks were spurious and the fitting routine was not able to reliably fit the data.

Raman Shift of Peaks

The fitted central shift of the measurable peaks are presented in figure 4.8, and the average centre shift of each peak as a function of excitation energy is presented in table 4.4. The fitted shift of each peak was corrected for by the 0.52cm^{-1} systematic offset in the Raman spectrum as calculated from analysis of figure 4.6 . The various panels shows the A and B peaks on the bottom, the 2A and 2B (middle) and the 2A+B and 3B peak on the top panel all in blue and green respectively. The error bars in the figure were determined by multiple independent measurements of the sample at the same incident wavelength (702nm). These repeat measurements were fit in the same way as discussed and the peak intensity, width and centre shift averaged over the number of repeats to give a value of the standard deviation and standard error in that particular resonance

run. Upon inspection of the data, it can be seen that there is no significant change in centre shift as a function of laser excitation energy and no obvious trend or dependence. It is clear from the data presented in the figure there is a significant anomalous results at ∼1.77eV, where all the Raman shifts of the peaks are lowered by ∼2cm^{-1}, this is likely due to an experimental error through processing the results and will be ignored. The Raman shift for the first 2 data points of the 2A+B trace (top panel, blue trace) are clearly significantly higher than the rest of the trace. Whilst it is not possible to be certain of this, it is apparent from figure 4.5 that the 2A+B peak has the most other features adjacent to it (3A and B+C) than any other peak fit out of the A, B, 2A, 2A+B or 3B, and is not resonantly enhanced at low energy. This means that the fitting process could be unreliable in this regime, and the model may have applied a best fit to the B+C peak (at 144cm^{-1}) for these 2 data points. Despite this, there is no evidence that the shift of the 2A+B or any of the fitted features are significantly dispersive with excitation energy. Which, if the peaks were due to vibrational modes as hypothesised is entirely expected.

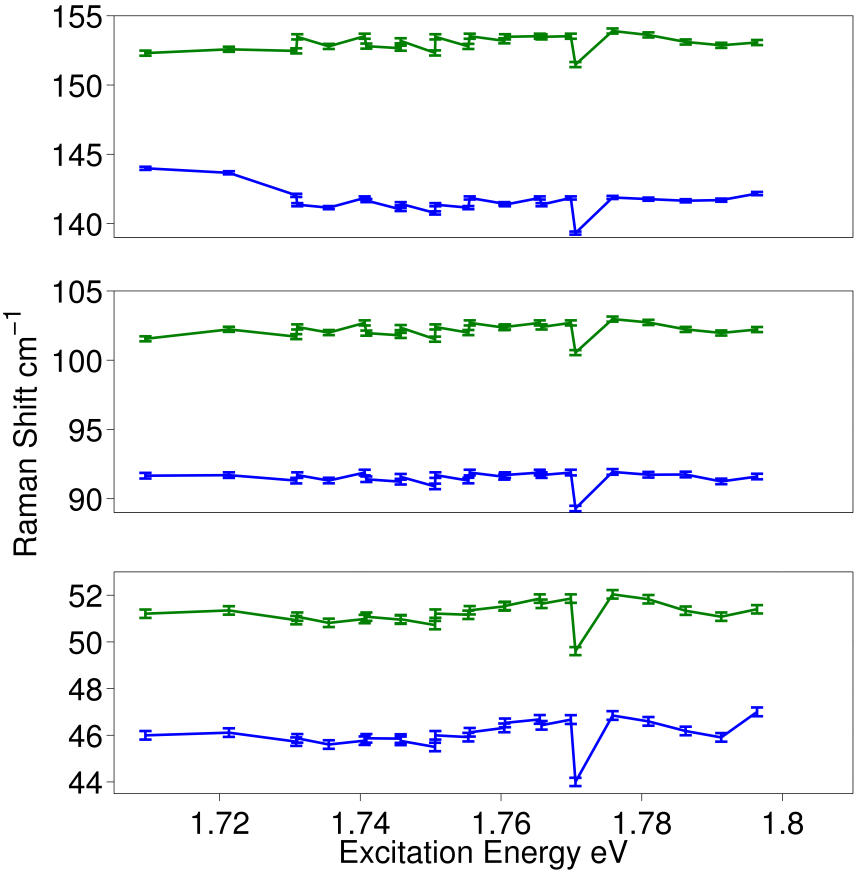

Figure 4.8: Fitted centre shift of modes as a function of wavelength. Top panel 2A+B and 3B, middle panel 2A and 2B and bottom panel A and B, all in blue and green respectively. Error bars in all cases are the standard error of multiple independent measurements of the Raman spectra at 702nm. The anomalous result at 1.77eV is discussed in the main body of the text.

Label	Mean Raman shift (± standard error) (cm^{-1})
A	46.90 (±0.04)
B	50.7 (±0.04)
2A	92.39 (±0.02)
2B	101.66 (±0.02)
2A+B	142.03 (±0.01)
3B	152.52 (±0.01)

Table 4.4: Mean Raman shift of each fitted feature as a function of excitation energy as corrected for by linear offset, errors in the mean correspond to the standard error.

Width of Raman Peaks

Figure 4.9 presents the fitted widths of the A and B peaks (bottom panel), 2B and 3B (middle panel) and the 2A and 2A+B peaks (top panel). The error bars from the figure represent the 95% confidence bounds from the least-squares fitting routine. The 95% confidence bands determined by the fitting was chosen over the standard error of the repeats at 702nm because of the resonant nature of the peaks, at energies off resonance the peaks are hardly observable and fitting becomes more unreliable, hence it is better to overestimate the error from the fitting process rather than underestimate it. The mean width for each peak along with the standard error of all the widths are presented in table 4.5. It can be seen from the data presented in the bottom panel of figure 4.9 that the A and B labelled peaks do not change significantly with excitation energy. The middle panel of figure 4.9 shows the energy dependence on the width of the 2B and 3B peaks, and again there is no evidence, to within the error, that the peaks change with energy. Finally the top panel of figure 4.9 shows no clear energy dependence on the width of the 2A+B peak, nor the 2A peak. Table 4.5 shows that in all cases the mean of the A peaks are broader than their equivalent B peaks, and that the 2A+B peak is significantly broader than the 3B peak. Whilst the higher energy peaks are broader than the fundamental peaks i.e the 2A is more than twice the width of the A, and the 2B peak is approximately twice that of the B, the 3B peak is not significantly broader than the 2B. Overall there is no clear energy dependence of any of the peaks widths measured, which again, if the peaks are due to vibrational modes, is the expected behaviour.

Label	Mean linewidth (± standard error) (cm^{-1})
A	0.55 (±0.11)
B	0.48 (±0.10)
2A	1.62 (±0.27)
2B	0.78 (±0.31)
2A+B	2.51 (±0.36)
3B	0.80 (±0.32)

Table 4.5: Mean linewidth of each fitted feature as a function of excitation energy. Errors in the mean correspond to the standard error.

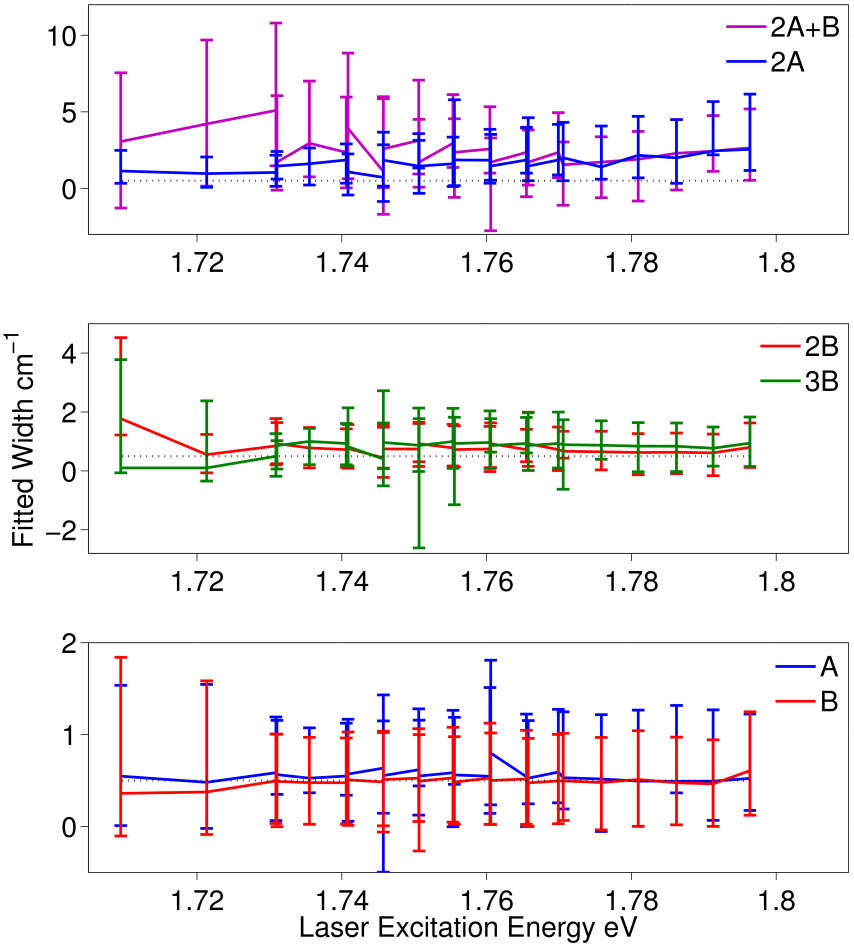

Figure 4.9: Fitted width of peaks as a function of laser excitation energy. In each subplot is also a black dashed line corresponding to the resolution limitations on the spectrometer and CCD. The error bars in each sub figure are the 95% confidence bands from the least-squares fitting routine applied to the peaks.

Intensity of Raman Peaks

After demonstrating there is no significant laser energy dependence of the Raman shift, or linewidth of the peaks that could alter the spectral weight of the peak, we are in a position to analyse the excitation energy dependence of the intensity of the peaks. The data presented in figure 4.10 shows the fitted peak intensity of the A, B, 2A, 2B, 2A+B and 3B features as a function of excitation energy. The data shows strong resonances with all the measured peaks, and as can be seen in figure 4.10, the resulting resonance profiles were also fit to a Gaussian lineshape. This lineshape was chosen to simply quantify the resonances. Multiple fits were attempted and it was found that the Gaussian gave marginally the best fit. The peak data, including the intensity, central energy and width of the Gaussian profile is presented in table 4.6, along with the 95% confident bands from the fit.

Peak	Amplitude (Counts s^{-1})			Width meV			Central energy eV		
	Lower 95%	Value	Upper 95%	Lower 95%	Value	Upper 95%	Lower 95%	Value	Upper 95%
A	33.13	36.16	39.18	46.88	54.93	62.99	1.727	1.734	1.74
B	251.3	269.7	288.2	31.12	34.35	37.59	1.774	1.776	1.778
2A	9.223	9.802	10.38	48.8	54.9	61	1.745	1.749	1.753
2B	84.86	92.37	99.88	29.64	33.35	37.05	1.775	1.778	1.78
2A+B	30.06	33.13	36.19	28.51	32.62	36.72	1.774	1.777	1.78
3B	30.78	34.03	37.28	28.95	33.28	37.6	1.777	1.78	1.783

Table 4.6: Fit parameters obtained from least square fitting of a Gaussian lineshape to the resonance Raman data at 4K. For each of the 3 parameters; amplitude, width and central energy we present the best fit and the lower and upper 95% confidence intervals from the fit.

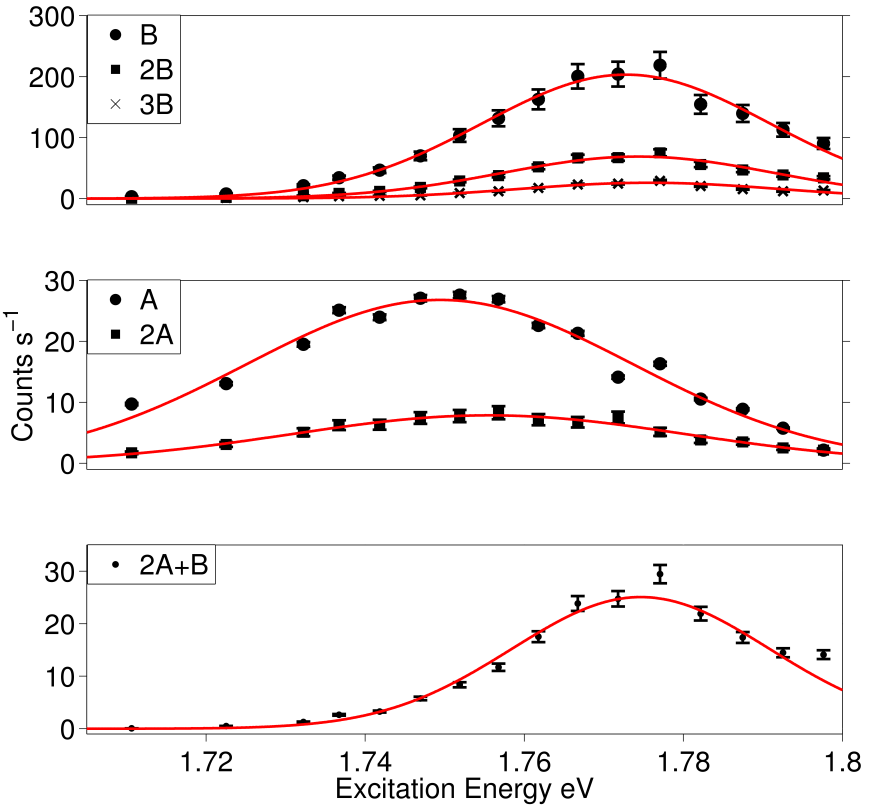

Figure 4.10: Fitted intensity of B, 2B, 3B, A, 2A and 2A+B peaks versus excitation photon energy measured at 4K. The resonances observed have been fitted with Gaussian lineshapes giving fit parameters presented in Table 1. The choice of a Gaussian lineshape is discussed within the main text.

It is clear from table 4.6 and figure 4.10 that the B, 2B and 3B peaks have a resonance at the same excitation energy of 1.778eV ±0.002eV. This value was calculated by the mean and standard deviation of the fitted central energy of each harmonic. It is also apparent from the figure that the intensity of the resonance decreases with increasing harmonic by nearly a factor of 10 between the B and 3B. In terms of the linewidths, there is no clear change to the width of the B, 2B and 3B resonances. However, we cannot be certain of this based upon the 95% confidence bounds from the fitting. The middle panel of figure 4.10 illustrates the intensity of the A and 2A peaks, which have a central energy of 1.734 and 1.749eV respectively. To within the 95% confidence bands of the fitting it can be said these two peaks have the same resonant energy. However, the resonance energy of the A and 2A are significantly different from the average resonate energy of the B harmonics by on average 36meV. The intensity of the 2A peak is $\sim$ 3.5 times less than the A peak, which when considering the confidence bands, is approximately the same ratio as the intensity of the 2B:B peak. Finally, like the B harmonics, there is no clear change to the width of the resonance with increasing harmonic order, however it is apparent that the width of the A and 2A peaks are broader than the B harmonics by a factor of about 1.5. The bottom panel of figure 4.10 shows the results from fitting to the 2A+B peak, whilst

this peak contains a portion of the A peak, its central energy and width is the same as the B harmonics (to within the confidence bands). In addition, the intensity of this peak is nearly identical to that of the 3B peak.

4.5 Polarisation Dependence

One possible explanation for the observed peaks in the Raman spectra, is that they are due to a novel nanowire form of HgTe. This section presents the evidence that the observed Raman features in the sample are due to nanowire like structures. It has been discussed in section 2.5.3 that a group of randomly orientated nanowire structures will interact with and emit Raman scattered light preferentially polarised parallel to the axis of the nanowire with a 3:1 contrast ratio. The experiment was set-up as discussed in chapter 3 and performed at 2 input polarisations (vertical and horizontal with respect to the lab frame). As with the previous experiments, the A, B, 2A, 2B and 2A+B data were fit with simple Lorentzian lineshapes, and the peak intensity plotted as a function of analyser angle. The results of the experiment are illustrated on a polar plot in figure 4.11. In each trace the horizontal and vertical input polarisation data have been normalised to the average of initial and final value of each respective trace, this was chosen as the only overlapping points in each plot.

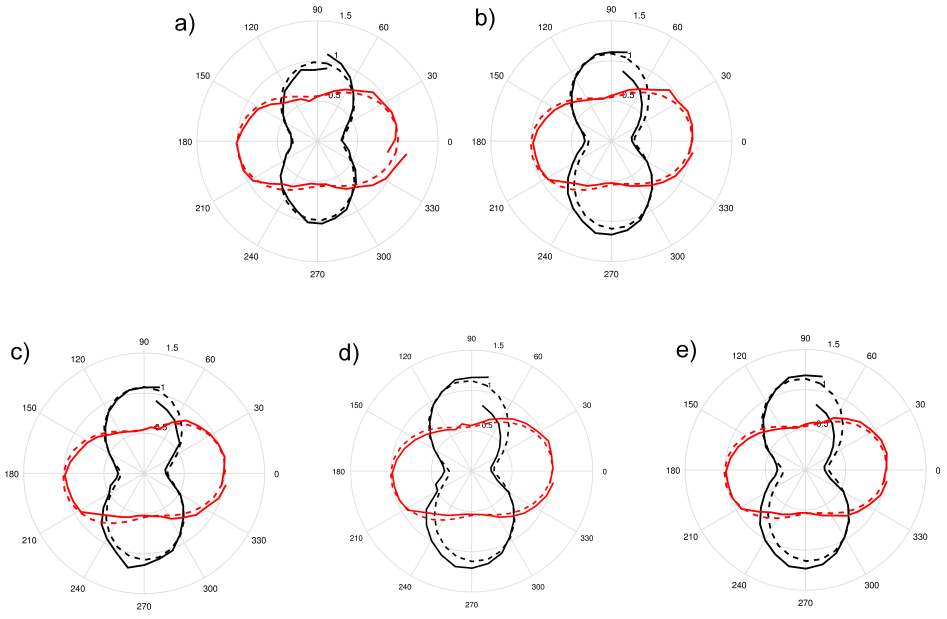

Figure 4.11: Polarisation dependence of the fitted intensity for a) the A peak, b) B peak, c) 2A peak, d) 2B peak and e) 2A+B peak for both vertical (black) and horizontal (red) input polarisations, each normalised to the average of the overlap points. In each figure the corresponding best fit for each trace is indicated by the dashed lines.

It can be seen from all panels of figure 4.11 that all the peaks obey a similar polarisation dependence. It can also be seen that there is a stronger contrast ratio for the vertical input polarisation when compared to the horizontal in all cases. To quantify the contrast ratio between the maxima and minima of the major and minor axis respectively, the data was fit to the equation;

$$k + q(cos^2(\theta + b)), \tag{4.1}$$

where b, q and k are fitting parameters for phase off-set, amplitude of modulation and peak intensity off-set respectively. Through this fit it is possible to use the ratio of k+q:q to quantify the contrast ratio of the best fit. The fitted values for k and q at both vertical and horizontal input polarisations are presented in table 4.7.

Label	Vertical		Horizontal	
	q (Amplitude)	k	q (Amplitude)	k
A	0.23	0.1	0.25	0.32
B	6.77	2.36	3.28	4.19
2A	0.14	0.05	0.1	0.14
2B	2.02	0.65	0.85	1.01
2A+B	0.56	0.18	0.24	0.27

Table 4.7: Table presenting the fitted amplitude of modulation and linear off-set for all the measured peaks at vertical and horizontal input polarisations.

Using the values from the peak data presented in table 4.7, the contrast ratio of the fits(k+q:q) were calculated and are presented in table 4.8 along with the mean value and standard error.

Label	Vertical	Horizontal
	Ratio	Ratio
A	3.22:1	1.78:1
B	3.86:1	1.86:1
2A	3.5:1	1.87:1
2B	4.09:1	1.84
2A+B	4.12:1	1.88
Mean(std error)	3.76(0.1)	1.85(0.02)

Table 4.8: Table presenting the ratio of the fitted amplitude of modulation and linear off-set for all the measured peaks at vertical and horizontal input polarisations.

It is clear from figure 4.11 that when excited with vertically and horizontally polarised light, there is a large change in the intensity of the Raman scattered light. This could mean one of two things; 1) the Raman scattered light is polarised, which is not what would be expected in a Raman process. Or, more likely 2) the light is unpolarised, but is more intense when the analyser is parallel to the excitation plane of polarisation. When excited with vertically polarised light, the average contrast ratio between the long and short axis is 3.76:1. In the case of horizontally polarised light the equivalent

ratio is 1.85:1 on average. In both cases there is a notable difference between the two overlapping data points corresponding to the 0° and 360° polariser angle. This difference is more significant using vertically polarised light and can be up to a ∼30% variation. This error is likely due to a misalignment of half-wave plate prior to the entrance slit. Despite the variation between overlapping points, it is not enough to cast doubt on the polarisation dependence observed, and therefore the evidence strongly suggests that the Raman features A, B, 2A, 2B and 2A+B measured behave like an anisotropic structure i.e a nanowire and not isotropic bulk material, or quantum dots. It is notable that the ratio between vertically and horizontally polarised light is definitely not the same, with the ratio for horizontal being about half that of the vertical case. In theory, for truly randomly orientated nanotubes this ratio would be the same. However, because of the van der Waals forces experienced by nanotubes, the tubes likely bundle together, forming domains [1, 115]. Due to this, it is likely that the difference between the ratios of vertical and horizontal input can be explained in terms of sampling an area of sample with a preferential direction of tubes.

4.6 Possible Physical Mechanisms for the Observed Peaks

This section discusses the overall observations for the data and explains these observations in terms of the possible physical mechanisms for the peaks in the Raman spectra, relating what is observed to the hypothesis that the peaks are due to 4 fundamental vibrational modes of a novel crystalline HgTe structure embedded within a nanotube. To clarify the data so far; resonance Raman spectroscopy at 4K has measured new Raman features that cannot be explained simply in terms of bulk HgTe or unfilled carbon nanotubes. Through fitting and quantitative analysis, these new features can be labelled as combinations or overtones of at least 3 fundamental peaks (A, B and C), in addition a 4th peak (D) is observed which does not have any clear harmonics or interactions with A, B and C. By tuning the incident laser energy it has been demonstrated that neither the Raman shift, or width of the measured features (A, B, 2A, 2B, 2A+B and 3B) have a significant dependence on the excitation energy. It is clear that the intensity of all the features have a strong dependence of excitation energy. The A and 2A features are resonant at the same basic energy (∼1.74eV) with comparable width (∼54meV), and the B, 2B and 2A+B resonate at ∼1.777eV with a width of ∼33meV. Polarisation dependent Raman spectra at a constant excitation energy clearly shows that all of the measured features behave in a way expected to for a nanowire like structure.
In chapter 3 the results of HRTEM characterisation was also presented, where it is clear in the sample images taken, that the predominant species present are carbon nanotubes, and Mercury Telluride embedded down the central pore of the SWCNTs. The typical bulk form of HgTe is a zinc blend-type structure that crystallizes in $P\bar{4}3m$. In this form, the Hg and Te atoms are in tetrahedral 4:4 coordination similar to carbon in diamond

(Fig 4.12(a))[7]. In three separate studies [5, 1, 177] the crystallisation of this material was assessed in a range of SWCNTs and double walled nanotubes (DWCNTs) and HRTEM (supported by CASTEP DFT [1]) found that in a diameter range spanning between 1.2-1.4 nm, a novel tubular form of HgTe predominates (Figs 4.12 (b) and (c)) in which the bonding of Hg and Te is transformed from tetrahedral to trigonal planar and that the coordination of Hg and Te is reduced from 4:4 (tetrahedral) to 3:3 (i.e. trigonal planar, in the case of Hg).

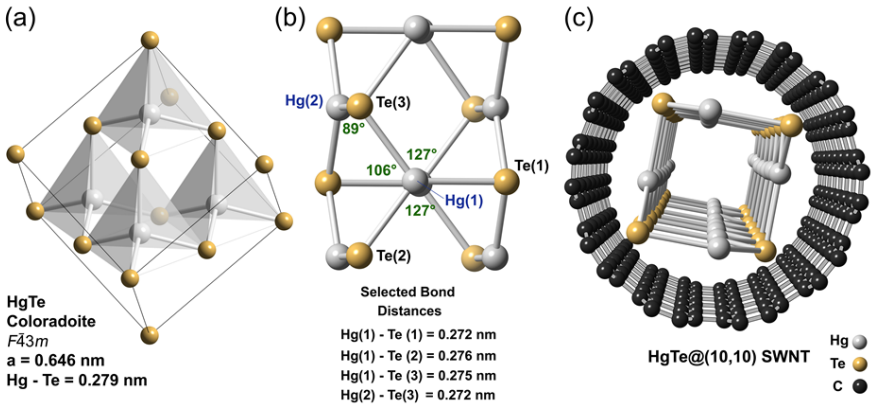

Figure 4.12: (a) Bulk zinc blend structure of HgTe with the Hg and Te positions reversed relative to the reported form [7] and with the average Hg-Te bond distance indicated. (b) Side on view of the DFT optimized 'tubular' form of HgTe (adapted from [1]). Te-Hg-Te bond angles in green and selected bond distances are indicated. (c) End-on view of the structure from (b) mounted in a (10,10)SWCNT.

From the TEM data, and the evidence presented through the Raman it is likely the peaks observed in the Raman spectra are due to vibrational modes associated with HgTe filling or the SWCNTs themselves. This section will now discuss the evidence and physics that supports the claim the features observed are due to a nanowire like structure of HgTe or SWCNTs.

One possible explanation of the modes observed is they are due to modified bulk HgTe or HgTe quantum dots. This is because the multiple harmonics and combinations observed in the Raman spectra are characteristic of II-VI semiconductors [175, 178]. Furthermore, because Hg and Te are large atoms, the expected vibrational energy would be relatively low, this is what is observed with the A and B peaks. Finally, low energy vibrational modes are expected for low dimensional structures e.g quantum dots because of the reduced coordination and translation symmetry. When taken in isolation, these arguments about the nature of Hg or Te Raman cannot be used to make definitive conclusions, as they also hold true for nanowire forms of HgTe. However, they do suggest that the Raman is more likely from a HgTe like object. When considering the polarisation dependent data, it eliminates the possibility the modes are due to anything but nanowire structures. In addition bulk HgTe is rarely seen in the TEM images, yet the fundamental spectra is

spatially homogeneous throughout the sample surface. Also, the strong resonances observed in all the modes is entirely in line with what is expected for nanowire like objects due to the presence of van Hove singularities [179]. Overall, the evidence points towards the hypothesis the Raman modes can only be due to a nanowire structure, and possibly a HgTe nanowire structure.

When considering the evidence that the Raman can only be explained in terms of nanowires, there is still a possibility the vibrational modes are due to some extreme effect on the SWCNT host in the probed area. For example it has been reported [180, 181] that under certain resonant conditions, intense, low energy squash modes, that are extremely sensitive to environmental change, can be observed in unfilled nanotube samples. However this possibility is unlikely, as apparent from figure 4.13 which shows the resonance of the 168cm^{-1} RBM of the filled tube sample, with the tabulated data for the fitted Gaussian in table 4.9. This is because the resonance energy of the RBM observed in the filled sample is only slightly blue shifted by ∼50±40meV from the unfilled RBM resonance. This blue shift pushes the resonance further away from that of the newly observed vibrational modes in the filled sample. Although such changes to the Raman shift and resonance energies of SWCNT features have been observed in other filled tube samples [33, 182]. It seems unlikely that an effect that significantly modifies the electronic structure of the nanotube in such a way as to yield the observed vibrational modes would not also greatly modify the transitions responsible for this RBM. This argument, coupled with those made earlier supports the hypothesis that the features observed are due to 4 fundamental vibrational modes of a crystalline nanowire of HgTe.

Central Energy Energy (eV)	Width Energy (eV)
1.625 ± 0.002	0.051 ± 0.0005

Table 4.9: Table showing all fitted parameters to the Gaussian lineshape applied to the filled nanotube RBM resonance

It is also possible that the Raman modes observed are due to a variety of HgTe nanowire structures, rather than the predominant form seen in 4.12. It is reported in textbooks [137] that the existence of combination modes and overtones can only be due to phonons from the same crystal structure. Whilst we cannot be certain of this in terms of the D peak, it strongly suggests the A, B and C Raman peaks are due to vibrational modes in the same crystal. The existence of the 2A+B peak and the B+C peak means that it is possible to reject the hypothesis that the optical transitions responsible for the A, B and C modes do not coexist in the same material. The hypothesis is also further supported when taking into consideration theoretical prediction for the energy of vibrations of the observed crystal structure as will now be explained.

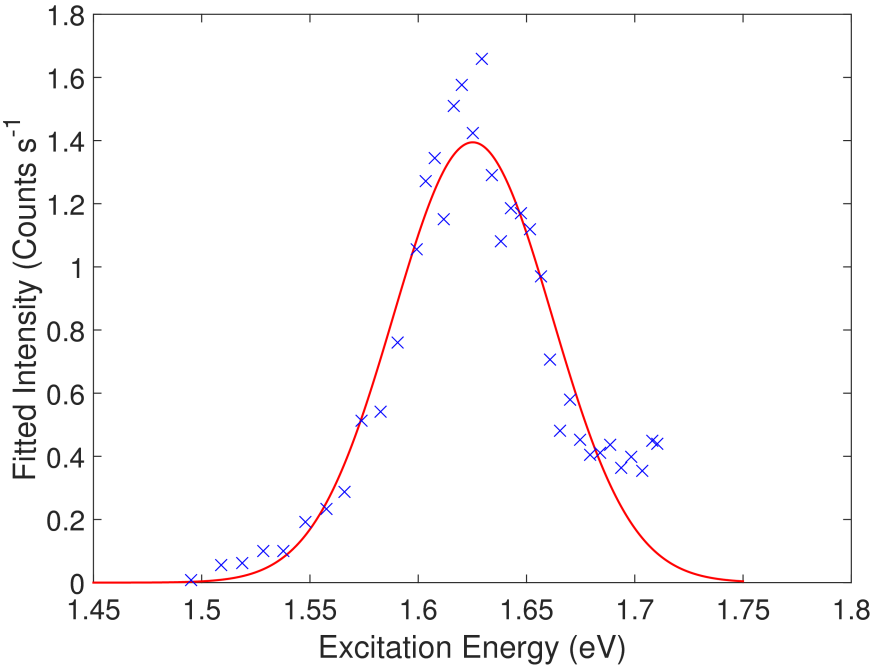

Figure 4.13: Fitted intensity to the 168cm^{-1} RBM in observed in the HgTe@SWCNT sample. Spectra has been fitted to a Gaussian lineshape to extract peak parameters shown in table 4.9 to directly compare to the central energy for the same RBM in the unfilled equivalent.

4.6.1 Symmetry Arguments

Now it has been provisionally demonstrated the peaks observed are due to vibrational modes of a novel form of HgTe nanowire, we are in a position to discuss the vibrational modes in terms of their symmetry. Vibrational group theory analysis was performed by Eric Faulques on the trial HgTe crystal structure as determined from TEM observations. The structure of the Hg and Te atoms from the TEM observations was determined to belong to the rod group p4_2m. The unit cell of this crystal contains 8 atoms (i.e Hg_4Te_4), each atom has 3N degrees of freedom and hence there are 24 mechanical degrees of freedom for the unit cell. From this information it was possible to calculate the number of different types of fully irreducible representations for the various symmetry operations applied the rod group of the crystal [1] given by;

$$\Gamma_{tot} = 4A_g + 2A_u + 4B_g + 2B_u + 2E_u + 4E_u. \tag{4.2}$$

The observed Raman peaks are hypothesised to be vibrational modes, therefore it is possible to eliminate the 3 translational modes, which were determined to be one A_u mode and one E_u (which is doubly degenerate). It is also possible to eliminate the rotational modes, which was determined to be one A_g mode around the axis of the cell, this mode should have zero frequency if the rod is isolated. The updated form of equation 4.2 leaves 15 vibrational modes as possible candidates for the modes observed

in the Raman, as given by;

$$\Gamma_{vib} = 3A_g + A_u + 4B_g + 2B_u + 2E_g + 3E_u. \tag{4.3}$$

From equation 4.3 it can be seen that there are 5 are doubly degenerate modes ($2E_g$+$3E_u$). This means there are 12 unique vibrational frequencies in the trial structure. It is clear that there are significantly more possible vibrations in the crystal than the 4 fundamental modes observed in the Raman spectra. However, through application of the Raman selection rules to the irreducible representations, it is likely that not all of the 12 vibrations will appear in the Raman. As expected by theory, the predicted modes with antisymmetric inversion symmetry i.e the $3E_u$ and A_u modes would be IR-active, and the rule of mutual exclusion would mean that in general these are not observable under Raman [183]. The non-resonant Raman selection rules predicts the Raman active modes to be; $3A_g$+$4B_g$+$2E_g$. However, because the experiments are done at strongly resonant conditions it is not clear whether these rules apply. Through these arguments, the most likely Raman active assignments for the predicted Γ point phonons are 9 vibrational modes consisting of 3 with A_g, 4 with B_g and 2 with E_g symmetry. This is still more than the 4 observed phonons, so it is clear through symmetry arguments alone, we cannot be sure of the nature of the observed modes.

4.6.1.1 Density Functional Theory

One possibility to investigate if the Raman results are consistent with the observed nanowire structure from HRTEM, and to better understand the energy of the vibrational modes observed in terms of their symmetry is to apply DFT (density functional theory) to the trial HgTe structure. This section discusses the results of DFT calculations performed by E. Faulques that are presented in [1]. DFT is a calculation to obtain quantum mechanical energies and forces for atoms in a crystal structure [184, 185, 186]. The technique can be used to calculate the energy of vibrational modes in a crystal, the phonon density of states and heat capacity of the crystal. DFT was performed using the CASTEP [186] code and applied calculated using a frozen phonon count to the HgTe unit cell, belonging to the rod group #29, $p4_2/m$, with point group symmetry C_{4h} [1]. Frozen phonon calculations involves explicitly calculating the forces between every atom in the crystal and constructing a force constant matrix. This matrix allows the calculation of the normal modes at a particular wavevector. To calculate the force caused by a specific atom, the atom is displaced and the DFT calculates the new forces on every atom. The limit for this technique, is that it generally requires large supercells to be accurate, and in this system, a small displacement of one atom in the unit cell creates forces on all the other atoms, which could limit the validity of results. The vibrational energy and its corresponding symmetry for all the vibrations predicted in eq 4.3, is presented in table 4.10.

Raman Shift cm^{-1}	Symmetry	Raman Shift cm^{-1}	Symmetry
5.1	A_g	107.2	E_u
15	B_g	110.4	A_u
21.2	E_g	112.7	B_g
27.5	B_u	121.3	E_g
36.7	B_g	130.5	B_u
53.68	A_g	132.7	A_g
53.74	E_u	148.4	B_g
106.5	A_g	149.1	E_u

Table 4.10: Table of DFT predicted Γ-point phonon mode Raman shifts and symmetry [1].

We are now able to use the arguments from 4.6.1, coupled with the results from the DFT, presented in table 4.10 to compare directly to observed Raman modes. The 4 lowest predicted Raman shifts (including the non-resonantly active B_u mode) from table 4.10 are too low frequency to observe through the experimental system so it is not possible to verify their existence and will therefore be ignored. The final 4, high energy predictions ($>130cm^{-1}$) could be present, but covered by the third order harmonics and combination modes, so again it is not possible to verify these. This leaves 8 candidates for the 4 fundamental modes (A, B, C and D) observed experimentally, of which some may not be Raman active, or resonantly enhanced. The vibrational modes predicted with B_g and A_g symmetry at 36.7 and $53.6cm^{-1}$ respectively are in reasonable agreement of the observed modes labelled A and B at 45 and $52cm^{-1}$, and are also allowed through the selection rules from section 4.6.1. However, removing the constraints as this is a strongly resonant system means that the observed B mode could also correspond to the double degenerate $53.74cm^{-1}$ predicted mode, but we cannot be sure of this. The observed C mode at $\sim 94cm^{-1}$ could correspond to the A_g mode with a predicted frequency of $106.5cm^{-1}$, likewise the D mode at $114cm^{-1}$ fits well to the mode with B_g symmetry predicted at $112.7cm^{-1}$.

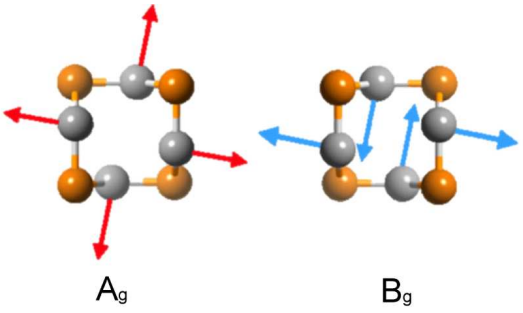

Figure 4.14: Ball and stick model of the HgTe simulated based upon TEM observations. Atomic motion of the predicted A_g and B_g vibrational modes in the Hg atoms are indicated by the arrows.

These two likely candidates (within the constraints applied) with B_g and A_g symmetry

for the A and B modes respectively, comprise of Hg atomic motion against each other in the xy-plane (Figure 4.14). The A_g vibration which leads to the largest change in inter atomic distances by figure 4.14 and would hence have a larger vibrational energy than the B_g vibration, which is what is observed. The more significant difference between the observed ($45cm^{-1}$) and predicted shift ($36.7cm^{-1}$) for the B_g phonon can be ascribed to the interaction between the HgTe rod and the surrounding nanotube, which has not been taken into account for in the calculations due to computational constraints. Finally, the $106.5cm^{-1}$ (A_g symmetry) and $112.7cm^{-1}$ (B_g symmetry) modes also both fit reasonably to the observed C and D modes at 94 and $113cm^{-1}$ respectively.

DFT also allows for the calculation of the electron band dispersion and the optical absorption constant associated with the predicted bands. The results of these calculations are presented in figure 4.15. It is clear from the right hand frame of figure 4.15 that the band structure of the HgTe rod is considerably different from that of a bulk crystal of HgTe (a semimetal)[187]. The results indicate that there are three conduction bands, close in energy, from which we predict three possible Raman resonances at the Γ point which are; 1.35, 1.5 and 1.7eV, as well as others at energies in excess of ∼2.5eV.

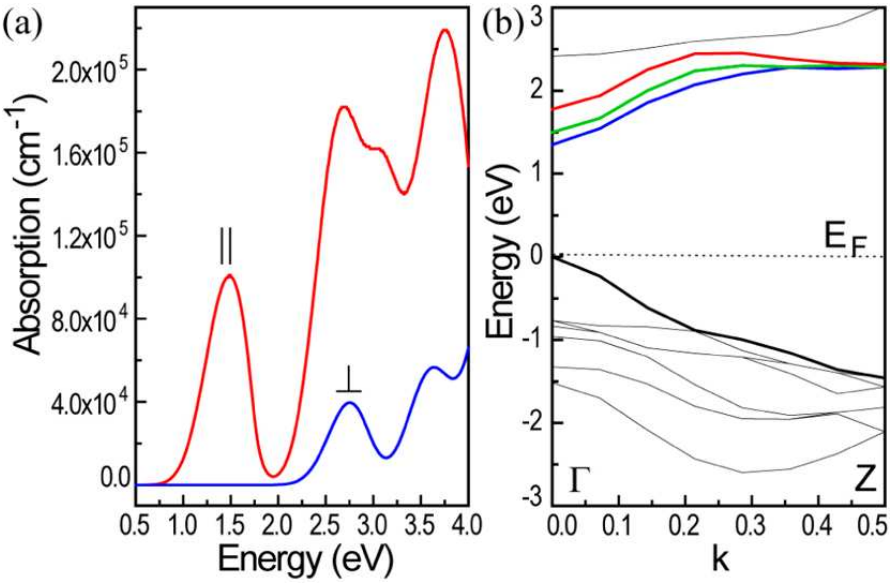

Figure 4.15: DFT predictions of the optical absorption (a) for light parallel and perpendicular to the filled tube and the electronic dispersion relation (b) for the single electron bands nearest to E_f [1].

Whilst we do not observe all the resonances predicted, the predictions do not contradict what is observed in terms of the strong resonances at ∼1.77eV for the HgTe modes. By inspection of panel a of figure 4.15, it can also be seen that these transitions are strongly polarised parallel to the filled tube. These results do not contradict what is observed experimentally and suggest, to within the errors of the DFT, that the strong resonance

observed at ∼1.77eV could be associated with the fundamental band gap of the HgTe, which would explain why only a single resonance is observed in the range measured; however, we cannot be certain of this.

4.7 Conclusion

In conclusion this chapter presented a low temperature, resonance Raman study into single-walled carbon nanotubes filled with Mercury Telluride. The measured Raman spectra contain an abundance of new features which have been clearly shown not to be associated with unfilled carbon nanotubes nor bulk HgTe or HgTe quantum dots. There is evidence the Raman peaks are due to 4 fundamental vibrational modes of a novel HgTe crystalline structure. Through detailed analysis of all of the peaks, it has been proposed and demonstrated that all non-SWCNT peaks observed can be attributed in some way to combinations or harmonics of 3 of the 4 fundamental modes, A, B and C. The existence of these harmonics provides strong evidence to the hypothesis that the features are due to a group II-VI semiconductor (i.e. HgTe). Due to the presence of clear combinations of the fundamental modes A, B and C, it can be stated that the Raman features observed are all from the same crystal structure, from the same nanotube, which is further supported by HRTEM imaging confirming the presence of the same crystalline structure of HgTe in the majority of the sample. It has been demonstrated that the Raman features measured at 4K (i.e. A, B, 2A, 2B and 2A+B) have a polarisation dependence that is indicative of a nanowire like structure and supporting HRTEM evidence [1] demonstrates the nanotube sample has filling within the tube pore with little extraneous bulk material. None of the modes observed have a significant energy dependence on their central Raman shift or width, which is entirely in line with what is expected if the features are due to vibrational modes [137]. The intensity of the modes as a function of excitation energy were fit to Gaussian lineshapes and it has been demonstrated that the B, 2B and 2A+B features are resonant at the same basic energy, whereas the A and 2A, although resonant with each-other, have a different central energy than the other features. However, it must be noted that the width of all the resonances are much larger than the energies of the fundamental Raman features that cause them, thus the resonances observed are an overlap of incoming and outgoing intermediate states, which may yield substructure with the resonances. The linewidth of the resonance for the B, 2B and 2A+B profiles were, to within errors the same, whilst the A had the same linewidth as the 2A, they were both significantly broader than the B, 2B and 2A+B.

DFT calculations, which do not include excitonic effects nor spin-orbit coupling, were performed based upon the structure of the HgTe nanowires observed by TEM. These are consistent with both the measured shifts of the Raman features and the Resonance energy to within reasonable errors. These calculations predict a bandgap for the HgTe wires of 1.35 eV; however, they also predict other optical transitions at energies of 1.5

and 1.75 eV that are candidates for the resonant optical transition. It is possible to within the errors of the DFT calculations that the resonances observed are associated with the fundamental bandgap of the filling material.

The Raman modes reported in this chapter are the first measurements of nanowires on this scale, and demonstrates the importance of resonance Raman spectroscopy studies on such low dimensional materials, which should be performed preferably at low temperatures. Whilst this chapter focuses on the analysis of the Raman features at 4 Kelvin to understand their origins, it did not go into the form of the resonances observed, nor investigate in great detail the behaviour of the linewidth of the resonances at higher order. This was intentional, as there is a lot of physics to understand with the linewidth of the resonances, not only as a function of harmonic order, but also as a function of temperature. The next chapter will report on the results and physics of temperature dependent resonance Raman spectroscopy of the sample studied in this chapter, to understand the nature of the resonance profiles and the coherence lifetime of the optical transitions responsible for them.

Chapter 5

Temperature Dependent Resonance Raman Spectroscopy Of HgTe@SWCNTs

This chapter presents a study into the temperature dynamics of the phonon modes and the resonances observed in the quantum confined HgTe structure reported in chapter 4. It will present the results of resonance Raman spectroscopy experiments performed over the excitation range 1.65-1.9eV with sample temperatures of 4K, 25K, 50K, 100K, 150K, 225K and 295K on the same sample as discussed previously. It reports a decrease in intensity of Raman scattering with increasing temperature, and explains this striking result in terms of a decrease in the coherence lifetime of the optical transition.

5.1 Motivation

The motivation behind this sequence of experiments is to better elucidate the effects observed during the preliminary experiments of chapter 4. The results presented in the previous chapter were taken at 4K, as it was found that at this temperature the signal of the Raman scattering was orders of magnitude higher than at room temperature. This effect is slightly unexpected, as in general for a Stokes Raman process, the intensity scales with temperature, due to a increase in the thermal phonon population. It has been observed in this thesis and associated publications [1, 8], that the intensity of the Raman resonances for HgTe are greatly increased at low temperature, which can possibly explain why other works on similar nanowire like structures have not observed Raman scattering from such an extended crystalline filling material [5]. It is for this reason that the main motivation behind this chapter is to better understand this effect and probe the physics underpinning the observations and to understand whether this can be extended

to other filling materials.

5.2 Experimental Details

This section briefly describes the details of the temperature dynamics experiments that are reported in this chapter. In many ways the experiments were similar to that discussed in 3 and 4.2, with the major experimental hurdle being able to accurately and repeatedly correct for sample drift due to thermal expansion as the sample temperature was changed and mechanical vibrations caused by the Helium pump. As reported previously, these issues were overcome by allowing for adequate time for the sample environment to come to thermal equilibrium, and precautions were taken to reduce mechanical vibrations introduced by the liquid Helium dewar. As with the previous chapter, localised laser heating can alter the sample temperature and produce a non-linear effect on the Raman intensity, details of laser heating was presented in chapter 3. To overcome non-linear effects that are introduced by laser heating, the laser power dependence of the Raman signal was measured, and the incident laser power set well within the linear regime of Raman intensity. This was 0.1mW for sample temperature between 4K-150K and 1mW for sample temperatures above 225K, the higher power was used at 225K-295K to ensure an adequate Raman signal.
Raman spectra were acquired in the energy range 1.65-1.80eV in 5meV steps. The sample temperature was set, and the sample position located and the system was left for 40 mins to allow the sample environment to reach thermal equilibrium. Resonance Raman spectra were acquired as previously described, and this process repeated at 7 distinct temperatures; 4, 25, 50, 100, 150, 225 and 295K.

5.3 Temperature Dependence of Optical Transitions in Unfilled SWCNTs

To understand the temperature dependence of the HgTe modes, it is useful to first consider a well-understood equivalent 1D material, namely carbon nanotubes. This is also a useful comparison because SWCNTs make up the sample, and it seems likely that a HgTe 1D material may have similar physics to other 1D materials, for example nanotubes exhibit Luttinger liquid like behaviour [61], and they may have a comparable temperature dependence. There have been a few useful studies on temperature dependent Raman spectroscopy on SWCNTs. It seems likely that if the temperature dependence of the host tubes, or unfilled equivalent behaves as expected through other reports, then it is likely that the observations on the HgTe filling is a real effect and not an experimental artefact. In addition this has potential to open up a new route of potentially interesting

physics within filled nanotubes. This section discusses in detail the observations made by other independent studies on the temperature dynamics of Raman modes in SWCNTs. One study in 2004 by Fantini et al. [126], observed in a bundle of SWCNTs, the E_{22} transition was red shifted for certain types of semiconducting nanotubes and blue shifted for other types. The resonance shifts in this study were measured by varying the incident power between 0.1 and 5mW, as a means to locally heat the sample, and measuring the Raman shift and intensity of the RBMs in the sample. It was found that some of the RBMs increased in intensity at higher powers, whilst others decreased, demonstrating that the electronic structure is dependant on sample temperature and tube type [126]. In another study by Cronin et al. [188], resonance Raman spectroscopy at 3 temperatures (573, 300 and 113K) of a 268cm^{-1} RBM in an isolated tube showed a 50meV red-shift of the resonance energy between 113 and 573K. The observed temperature dependence in both has been attributed to a number of reasons, including lattice expansion, nanotube interactions and electron-phonon coupling [126, 188]. It is interesting to point out that in this paper, the authors report that the red-shift of the resonance for isolated tubes differs from bundled tubes. They attribute this to be due to a dominance of electron-phonon coupling in the isolated tube, rather than bulk thermal expansion of an array of interacting nanotubes. It is tempting to make the hypothesis that in the case of the HgTe@SWCNTs, because the nanowire is likely screened by the nanotube from the sample environment, any red-shift observed may be predominantly due to electron-phonon coupling rather than lattice expansion. However it is not possible to probe this difference directly within this thesis. Whilst it seems that the resonances of SWCNTs behave as expected i.e the width increases and the transition red-shifts with increasing temperature, there are few reports that discuss the intensity of the resonances as a function of temperature. In one study by Simon et al. [189], the resonance intensity of the RBM SWCNTs and DWCNTs was investigated at temperatures between 80K and 600K. The interest in this work is with regard to the fundamental similarities between the inner tube of the DWCNT and the filling material in HgTe@SWCNTs, as the inner tube from [189] can be thought to be a filling compound. The authors report a decrease in the peak intensity of the resonance transition for the inner tube of the DWCNT by almost a factor of 10 between 80 and 600K. They explain the red-shift by band-gap softening at higher temperatures due to electron-phonon coupling, and the width of the transitions broaden at higher temperatures due to temperature dependant homogeneous broadening. In a separate study by May et al. [190], the authors report on a decrease in the peak resonance intensity of SWCNTs as temperature is raised and ascribe the observations to lifetime broadening [191, 192], however the work does not report in great detail on the linewidth of the resonances to support the claim.

5.4 Results of Temperature Dependant Resonance Raman Spectroscopy

This section presents the data, and fits for RRS experiments performed at various temperatures. It will begin by presenting the temperature dependence of the fundamental phonon modes observed and their respective harmonics, then move onto the interesting temperature dynamics of the resonance profiles. As demonstrated in chapter 4, the peak of the resonance for the B peaks at 4K was ∼1.77eV, and not to dissimilar for the A peaks. So in the first instance the experiments on temperature dynamics of the Raman were measured using this fixed incident wavelength.

Figure 5.1 presents the Raman spectra of the HgTe nanowire samples measured with incident photon energy of 1.77eV at 4 distinct sample temperatures, 4K, 100K, 225K and 295K. The y-axis of each panel has been converted to a log scale for ease of viewing. The data presented in this figure is of the sample spot reported in the previous chapter, and it can be seen that at low temperature the 4K spectra presented here, and in the previous chapter are virtually identical, indicating there no sample degradation has occurred over time. Other sample spots were investigated and it was found that in all cases the HgTe Raman features behaved in the same way. The chosen spot was the same as per the previous chapter due to it being a particularly spatially homogeneous area on the sample, meaning that effects of drift or spatial variation during a spectral acquisition would be minimised. Multiple sample spots were probed as detailed in chapter 3, where it was found that the same basic Raman peaks appear throughout the sample, and have the same excitation and temperature dependant behaviour. The data presented in this figure highlights the motivation of this chapter. It is clear that as temperature increases there is a decrease in the intensity of the Raman scattering, with no obvious change to the basic shape of the modes and no new peaks appearing, indicating there is no phase change in the material between these temperatures. It can be seen there is a decrease in Raman intensity of the all the HgTe Raman peaks as a function of temperature, by more than an order of magnitude over the full range of temperatures in the case of the B mode. The observed effect is also interesting as it appears to have the opposite temperature dependence to what likely is the radial breathing mode of the host tube. The temperature dependence of the RBM is much weaker, and appears to slightly increases in intensity with increasing temperature, however despite it seeming to increase we cannot be certain that it is not associated with a shift of the optical transition [188].

The remainder of this chapter will detail the temperature effects of the Raman modes observed in terms of their linewidth, centre Raman shift, then move onto presenting the temperature dependence of the resonances in order to understand the dramatic reduction in Raman scattering at higher temperatures.

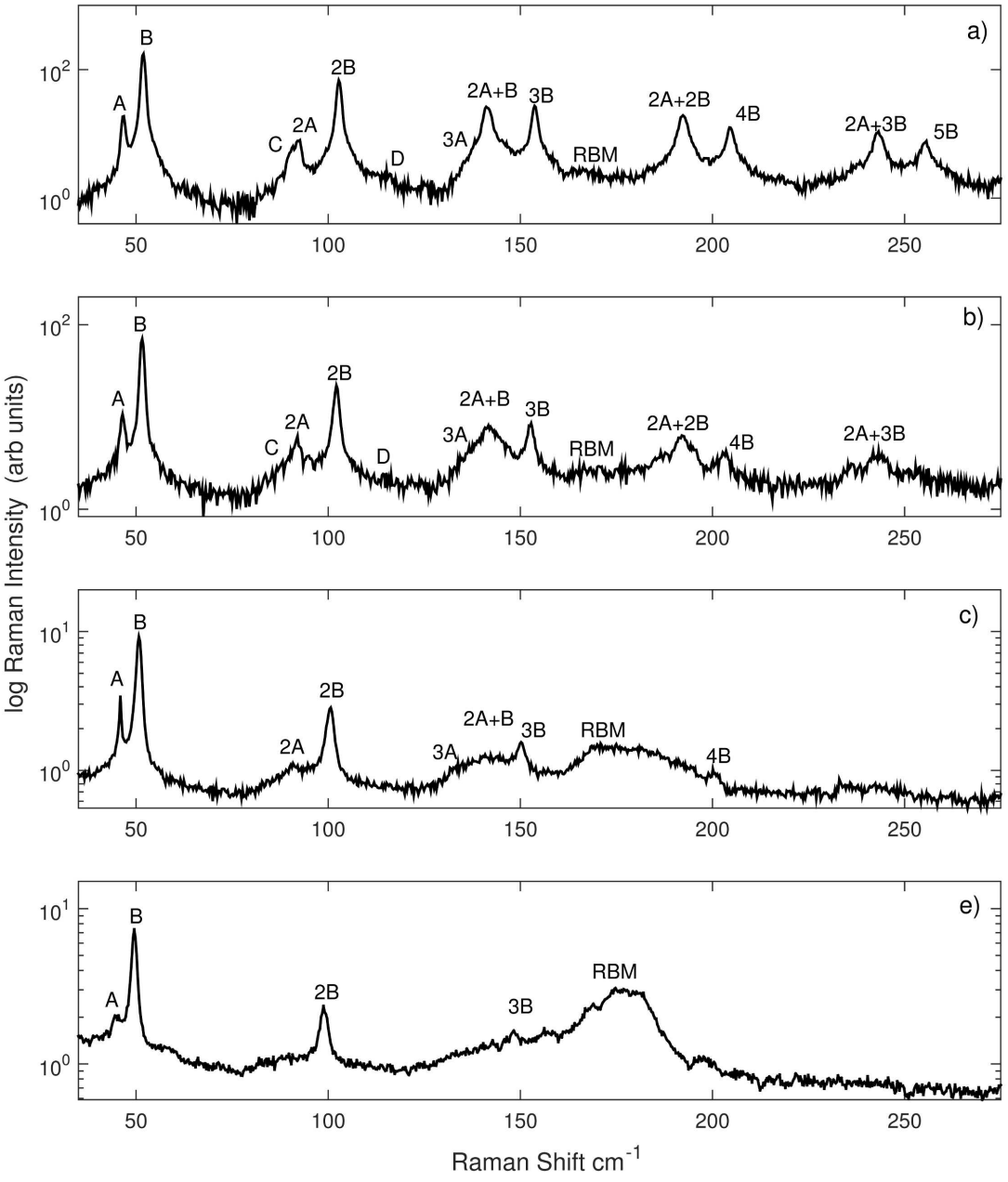

Figure 5.1: Stokes Raman spectra of SWCNTs filled with HgTe measured using a laser excitation energy of 1.77eV and cryostat temperatures of 4K, 100K, 225K and 295K by the traces in panels a)-e) respectively. The y-axis is converted to a log-scale for ease of viewing the higher order modes.

Raman Shift of Modes

Presented in figure 5.2 is the data for fitted centre shifts of the A, B, 2A, 2B, 2A+B, 3B modes as a function of temperature. Also shown in the figure is the fitted shift for the 168cm^{-1} RBM taken at its respective resonance (1.71eV). The data presented has been corrected for by the linear systematic offset of the peaks as calculated from figure 4.6 in section 4.4.1.1. Higher order modes are not presented due to the low intensity at high temperatures making the fitting unreliable. It is clear from the data in this figure,

that all of the modes (with the possible exception of the 2A+B peak) show a gradual softening as temperature is increased. This softening is observed in most materials and can be explained due to lattice expansion [193]. Also presented in figure 5.2 are the predictions for the centre shifts of the modes based upon arithmetic combinations of the fundamental modes. In all cases, again with the possible exception of 2A+B, the Raman shift of the higher order modes as a function of temperature follow the same basic behaviour of the fundamentals. It must be noted that whilst the 2A+B prediction lies close the measured values it does not appear to follow the same trend, which may suggest that the 2A+B mode is not a pure combination of A and B. This could be understood in terms of relaxation on the constraints for momentum conservation rules for multiphonon Raman scattering [137]. By fitting the shift of the A and B modes as a function of temperature to a simple linear line the rate of softening was determined to be $\sim$0.6x10^{-2}cm^{-1}K^{-1} for both the A and B modes. The equivalent fit was also applied to the 168cm^{-1} RBM (red trace in panel a of figure 5.2) and the gradient determined 0.8x10^{-2}cm^{-1}K^{-1}. This fitted value is comparable to the behaviour of other RBMs of unfilled SWCNTs [194]. Whilst there is similarity to the phonon softening rate of the SWCNT and filling modes, it is not clear whether there is any useful physics that can be immediately obtained by this relationship. Another comparison of the data would be to the bulk HgTe phonon modes and how they soften as a function of temperature. After an extensive literature search there doesn't appear to be a body of work that clarifies this situation and therefore it is unlikely a reasonable comparison can be made to bulk.

Overall the behaviour observed in the Raman shift of the phonon modes as temperature is increased is generally consistent in the sample i.e it is observed for all features, and can be understood in terms of lattice expansion.

Width of Modes

The peak widths for the fitted modes are displayed in figure 5.3. In panels (b) and (c) it can be seen at the lowest temperatures, the linewidth is close to the pixel width resolution of the CCD at the excitation energy used for this experiment, which is $\sim$0.3cm^{-1}. Despite this, the width is sufficiently broad enough to reliably fit the data. It is clear from the data presented in all the panels that all the phonon modes exhibit a broadening as a function of temperature. This effect is a commonly observed and understood process [195, 196, 197] in crystalline systems and can be explained in terms of a decrease in phonon lifetime as temperature is increased, due to the increased anharmonic decay of the phonon into lower energy phonons at higher temperatures [197, 198]. It is interesting that the linewidth of A, 2A and 2A+B mode has a stronger dependence on temperature than the B modes. To quantify the difference between the width increases as a function of temperature, the data presented in each trace was fit to a straight line, where the gradient would correspond to the rate of width increase per Kelvin change in temperature. The results of this fitting is presented in table 5.1. The corresponding y-intercept for the linear fit is presented in table 5.2. By inspection of the data presented in table 5.1 it is

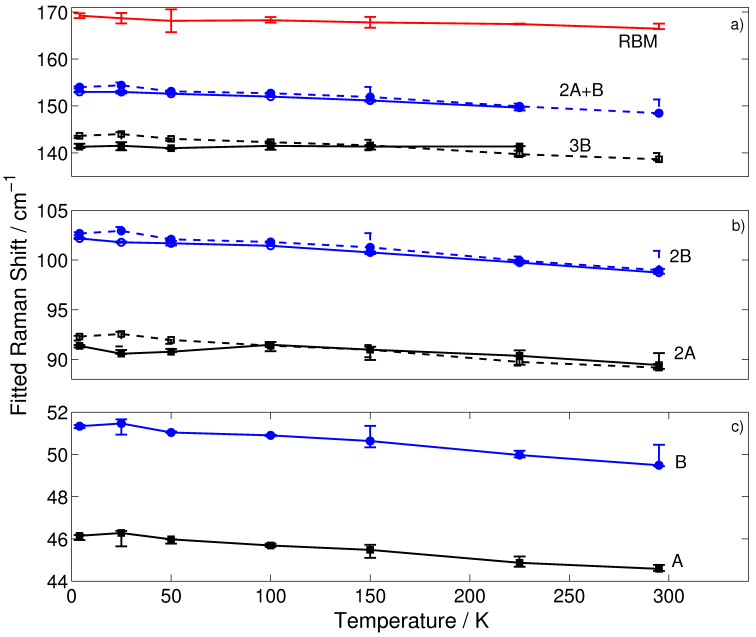

Figure 5.2: Fitted central Raman shift for the A and B (panel c), the 2A and 2B (panel B) and the 3B and 2A+B (panel a) for a sample fo HgTe filled SWCNTs as a function of discrete changes in temperatures. The dashed lines in panels a and b correspond to multiplications and combinations of the fundamental centre shifts from those presented in a. Error bars in all panels correspond to the 95% confidence bounds by fitting Lorentzian lineshapes to the observed modes.

Label	Fitted Gradient (cm^{-1}/100K)		
	Lower Confidence	Gradient	Upper Confidence
A	0.189	0.252	0.315
2A	1.512	1.997	2.482
B	0.033	0.070	0.103
2B	0.095	0.160	0.225
3B	0.054	0.113	0.173
2A+B	2.117	2.544	2.971

Table 5.1: Table presenting the fitted gradient of the straight line applied to width of each mode as a function of temperature in figure 5.3. The columns Lower and Upper confidence correspond to the 95% confidence bands of the linear fit.

clear that A, 2A and 2A+B modes broaden more rapidly than the B, 2B and 3B. It is also apparent that, to within confidence bounds of the fit the harmonics i.e. the 2A, 2B, and 3B broaden at a faster rate than the fundamentals, and that the 2A+B peak has the greatest broadening rate over all other features.

In terms of the absolute values of the linewidth from both table 5.2 and figure 5.3, in all cases the A, 2A and 2A+B modes are broader than the equivalent B, 2B and 3B at same temperature, and that whilst the width increases as a function of order, the increase in width for the 2A peak is far more significant than the increase in the B harmonics. It

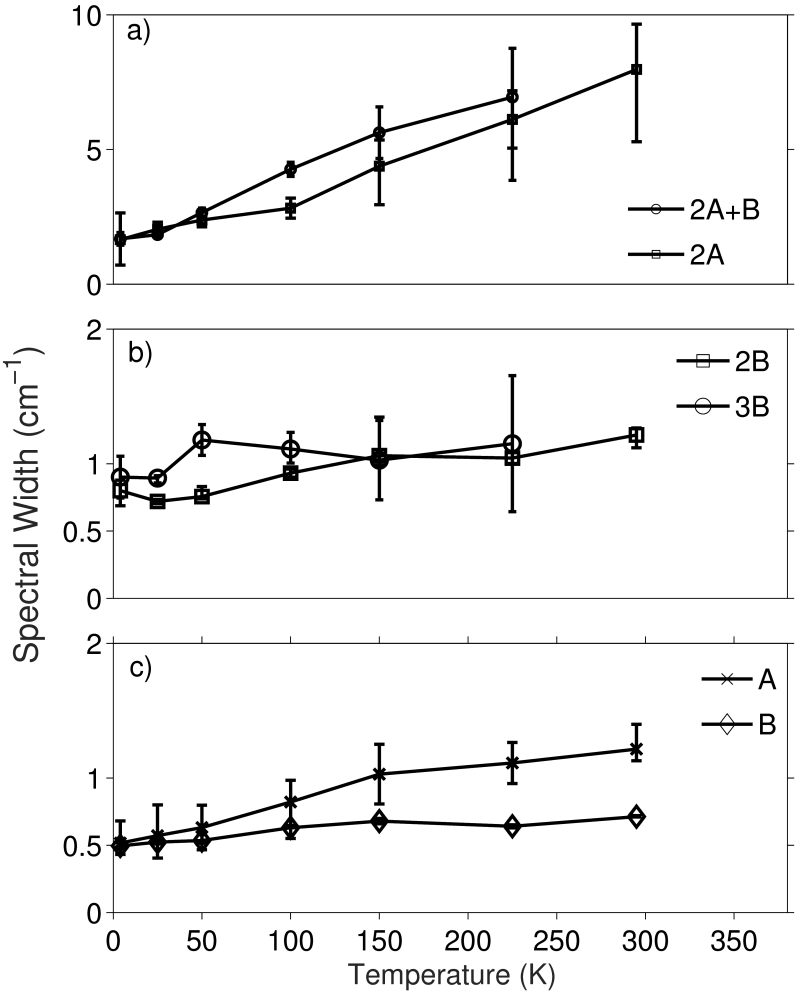

Figure 5.3: Fitted linewidth of the A and B (panel c), 2B and 3B (panel b) and the 2A and 2A+B (panel a) modes as a function of discrete changes in temperature. The error bars in each panel come from the 95% confidence bands from fitting Lorentzian lineshapes to the modes.

Label	Intercept (cm^{-1})		
	Lower Confidence	Intercept	Upper Confidence
A	0.43	0.53	0.63
2A	0.76	1.27	1.82
B	0.45	0.51	0.57
2B	0.63	0.73	0.83
3B	0.75	0.90	1.04
2A+B	0.97	1.48	1.99

Table 5.2: Table presenting the y-intercept of the fitted straight line to the data presented in figure 5.3. The columns Lower and Upper confidence correspond to the 95% confidence bands of the linear fit.

is possible that the increasing width of the B overtones could be explained in terms of the harmonics being simple linear combinations of the same phonons responsible for the fundamental, however the data is insufficient to use this explanation. However, it is clear

the 2A peak is far too broad to be a simple combination of the fundamental A mode. In this case as with the 2A+B modal shift discussed earlier this could be explained in terms of less restrictions on momentum conservation with two-phonon Raman scattering. Finally, it is apparent that the width of the 2A+B is significantly broader than the B modes, and similar in behaviour to that of the 2A, which suggests that the width of the 2A+B mode is dominated by the 2A components of the scattering.

Whilst is it fairly clear that broader linewidths of higher order modes can be understood in terms of increased anharmonic decay of the phonons into 2 lower energy phonon modes, it is not immediately obvious why the rate of broadening of the 2A mode is much greater than the A mode. Again, it is also not obvious that the data in table 5.2 reveals any useful information, especially when considering that the fundamental modes are likely to be near or at the instrumental limitation at that point.

When taken together, the temperature dependence of the centre shift and the width of the measured modes, show no significant change to the structure of the Raman spectra, and in general the observed effect can be well understood in terms of lattice expansion and lifetime effects. More significantly, because of the consistency of the Raman spectra as a function of temperature, this suggests there are no obvious changes to lattice structure of the HgTe crystal within the tube, and hence a phase change or similar effect cannot be responsible for the strong temperature dependence of the Raman scattering rate of the HgTe modes.

Photon Energy Dependence of Raman Scattering

From the data presented in fig 5.1 it is clear the intensity decreases at higher temperatures. However, as observed in other reports on nanotubes [126, 189, 188], this decrease in intensity may be an artefact from a temperature dependent shift of the resonance energy. To better elucidate the changes in intensity at a function of temperature, it is therefore necessary to map the resonances reported in the previous chapter as a function of temperature.

Preliminary evidence (presented in figure 5.4) suggests the nature of the resonance profiles do change as a function of temperature. The figure presents the data for the spectral weight of the B, 2B, 3B, A, 2A and 2A+B fitted modes in panels a)-f) respectively for temperatures 4, 100 and 225K. Spectral weight was calculated at each data point by multiplying the fitted peak intensity of the Lorentzian lineshape by it's corresponding measured linewidth, converted to pixels, at each excitation energy. It is visually clear from all panels of figure 5.4 that as temperature is increased, there is a slight red-shift of the resonance and a broadening, it is also clear that the spectral weight decreases.

As discussed in more detail later and in section 3.4, it is not possible predict the shape of the resonance without prior knowledge. Least squares fitting of a variety of standard lineshapes including Gaussian, Lorentzian and double-Lorentzian were attempted but it was not possible to identify a clear best lineshape. Therefore the resonances were all fitted using a Gaussian lineshape to allow simple quantification of the centre energy,

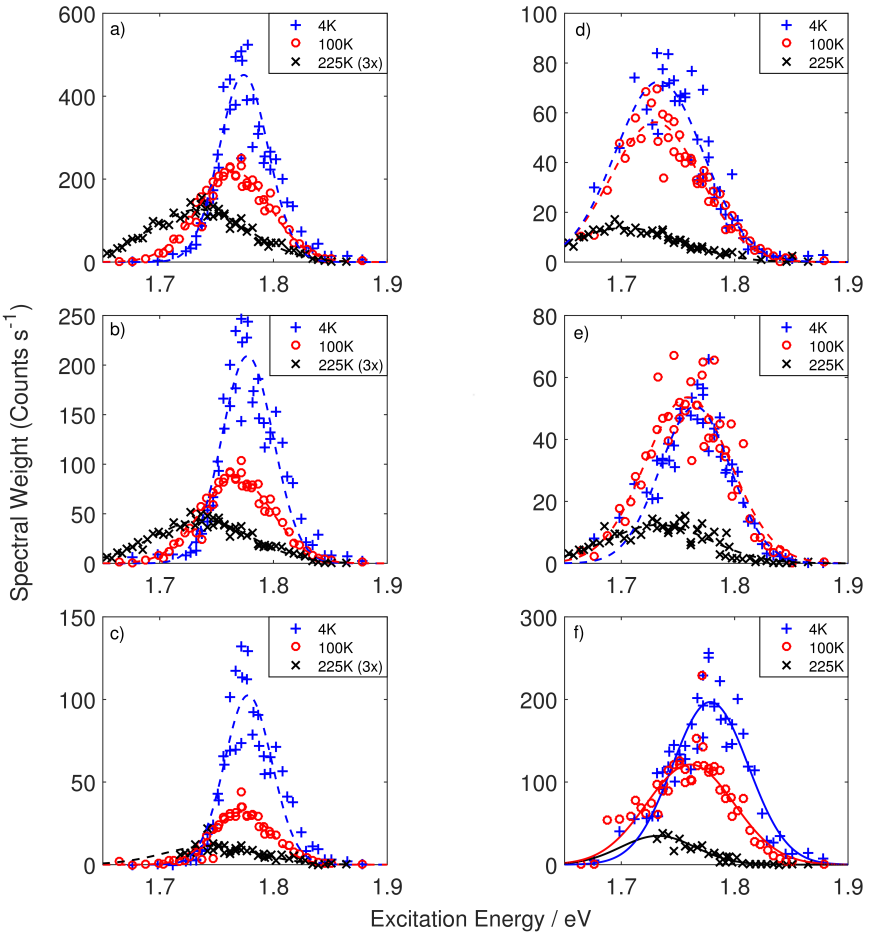

Figure 5.4: Excitation photon energy dependence of the Raman scattering intensity for the fitted modes B, 2B, 3B, A, 2A and 2A+B fitted modes in panels a)-f) respectively for temperatures 4, 100 and 225K, as illustrated by blue pluses, red circles and black crosses respectively. Also shown are the phenomenological Gaussian fits to these modes. In the case of the 225K data for panels a)-c) the data has been scaled by a factor of 3 for ease of visualisation.

width and amplitude of the resonance as a function.

A consequence of the strong temperature dependence on the Raman scattering is that at higher temperatures the fitting for the data becomes unreliable, this is highlighted by the 225K data presented in panels c and f of figure 5.4 where it was not possible to reliably fit the data at the low energy side of the resonance. It is for this reason that some of the higher order resonances (i.e. the 3B and 2A+B) at higher temperatures are not presented in the analysis of this data.

Figure 5.5 presents the fitted data for the spectral weight (a), central energy (b) and width (c) of resonances as a function of temperature. Figure 5.5 (panel b) shows the temperature dependence of the central energy of all the fitted resonance profiles. From this data it is apparent that the B, 2A, 2B, 3B and 2A+B resonances share a single centre energy for their resonances, which have a similar temperature dependence. It is also clear that the resonance of the A peak occur at lower energies. The 300K data in

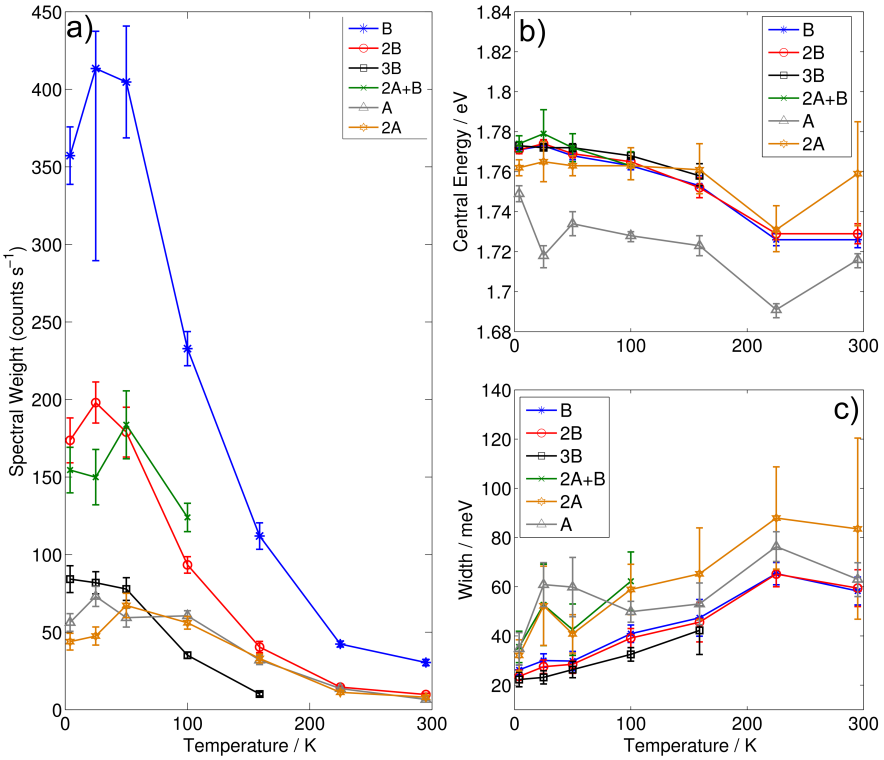

Figure 5.5: Extracted parameters of the Gaussian fit applied to the A, B, 2A, 2B, 2A+B and 3B modes as a function of temperature for the simultaneous emission model. Panel (a) shows the spectral weight of the resonances, b) the central energy and c) the fitted width. The error bars in each panel are associated with the 95% confidence bounds arising from the fitting.

all cases shows either an increase in the central energy, or no change from the previous data point, this is likely not a true representation as at higher temperatures the signal is much lower, and fitting becomes more unreliable. In all cases the resonances red-shift as temperature increases, and this can be likely ascribed to be due to lattice expansion, common in crystalline materials. Another observation in SWCNTs [188] that are isolated and suspended, suggests that the shift of the optical transitions is predominantly due to the electron-phonon coupling, rather than thermal expansion observed in bundled tubes. Since the Raman resonance observed are from a nanowire structure embedded within a nanotube, it is tempting to suggest that this could be an explanation for the observation, however we do not have appropriate data for this conclusion.

The absolute difference between the resonance energy of the fundamental A and B mode at each temperature was calculated and mean difference and standard deviation found to be 32±1.3meV. This difference is clearly much greater than the energy of the phonons of either the B or A (∼5meV) mode and is comparable to the measured resonance linewidths for both modes. Because of this, and due to the presence of clear combinations of the A and B peaks, it is likely that the optical transitions responsible for the resonances are closely related.

Figure 5.5 (panel c) illustrates the fitted linewidth of all the resonances as temperature is

increased. It is clear than in all cases the resonances increase linearly with temperature, by approximately a factor of 3 between 4K and 225K, and that the linewidth of the resonances are greater than the energy of the phonons involved. It is also apparent that the A and 2A resonances are broader than the various B resonances, in addition, the 2A+B resonance has a comparable width to the 2A resonance. It seems visually likely in the case of the B harmonics, up to at least 150K, that the resonance widths of the higher harmonics are narrower than the lower ones. This may yield information about the emission process of the phonons which will be detailed shortly.
Finally upon inspection of data presented in panel a of figure 5.5 it is clear that there is a significant drop off in intensity of all the resonances as a function of temperature. These decreases in amplitude are even more pronounced when considering the fact the thermal population of phonons increases by a factor of ∼5 for the resonances and harmonics

5.5 Discussion

This section aims to form a basis for the theoretical interpretation of the physics in the data. It will begin by explaining the details of phonon creation in a Raman process, and the parameters that the Raman scattering rate depends on. It will discuss the role of electronic coherence lifetime in the Raman scattering rate and interpret the data based on various models applied to understand the observed effects.

5.5.1 Phonon Emission

This section aims to discuss the theory behind phonon emission in a Raman process, for many types of possible emission processes. It will begin by presenting the theory behind a one-phonon Raman scattering event, and will develop the discussion from there. The basic process behind Raman scattering is well-understood, as is resonance Raman and there have been multiple books and publications on the topic; the Light Scattering in Solids series [137] being a notable contribution. Due to the weak interactions involved, time-dependent perturbation theory can be used to model Raman scattering successfully [137], and these calculations usually make use of Feynman diagram formalism [147]. For now, we will only consider the result of perturbation calculations for three Raman processes, these are; one-phonon emission, two-phonon simultaneous emission and finally two-phonon sequential emission.
For a single phonon Raman scattering event, the dominant process involves the sequential absorption of a photon creating an electronic excitation in a virtual or real state. Followed by scattering through a phonon interaction to a second virtual, or real electronic excitation. This excitation then propagates until it relaxes and emits a photon in

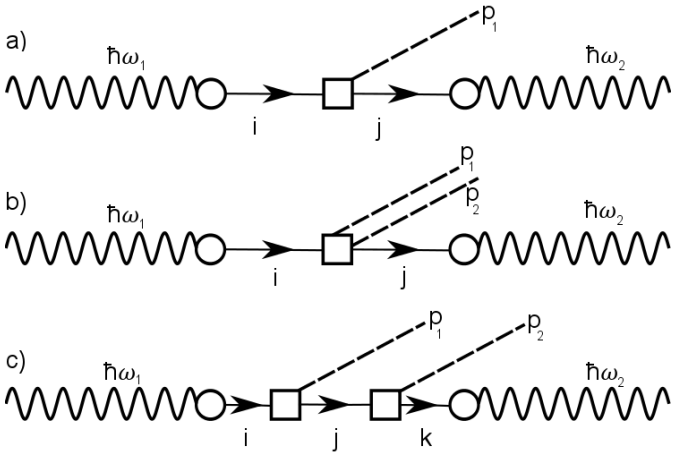

Figure 5.6: Feynman diagram of a typical Stoke's Raman process for (a) one-phonon emission, (b) two-phonon simultaneous emission and (c) two-phonon sequential emission. The process involves absorption of the incident photon ($\hbar\omega_1$), which creates and electron-hole excitation (first open circle). This excitation then propagates and scatters by the emission of a phonon (2 phonons (b)) ($p_{1,2}$) at the open square, to a second electron-hole excitation ((a) and (b)), which propagates until it decays emitting a photon ($\hbar\omega_2$) at the second open circle. In the case of (c) the a subsequent interaction creates a second phonon before the final excitation decays, emitting a photon.

the process. The Feynman diagram presented in figure 5.6 (a) gives rise to the standard formula for the probability of Raman scattering by perturbation theory [166];

$$|\sum_{i,j} \frac{\langle 0,n|\,\hat{H}_d\,|i,n\rangle\,\langle i,n|\,\hat{H}_{e-p}\,|j,n+1\rangle\,\langle j,n+1|\,\hat{H}_d\,|0,n+1\rangle}{(\hbar\omega_1-\hbar\omega_i-i\Gamma_i)\,(\hbar\omega_1-\hbar\omega_{p1}-\hbar\omega_j-i\Gamma_j)}|^2. \tag{5.1}$$

For the case of two-phonon Raman, depending on whether the emission occurs simultaneously, or sequentially the expression takes the form;

$$|\sum_{i,j} \frac{\langle 0,n|\,\hat{H}_d\,|i,n\rangle\,\langle i,n|\,\hat{H}_{e-2p}\,|j,(n+2)\rangle\,\langle j,(n+2)|\,\hat{H}_d\,|0,(n+2)\rangle}{(\hbar\omega_1-\hbar\omega_i-i\Gamma_i)\,(\hbar\omega_1-\hbar\omega_{p1}-\hbar\omega_{p2}-\hbar\omega_j-i\Gamma_j)}|^2, \tag{5.2}$$

$$|\sum_{i,j,k} \frac{\langle 0,n|\,\hat{H}_d\,|i,n\rangle\,\langle i,n|\,\hat{H}_{e-p}\,|j,(n+1)\rangle\,\langle j,(n+1)|\,\hat{H}_{e-p}\,|k,(n+2)\rangle\,\langle k,(n+2)|\,\hat{H}_d\,|0,(n+2)\rangle}{(\hbar\omega_1-\hbar\omega_i-i\Gamma_i)\,(\hbar\omega_1-\hbar\omega_{p1}-\hbar\omega_j-i\Gamma_j)\,(\hbar\omega_1-\hbar\omega_{p2}-\hbar\omega_k-i\Gamma_k)}|^2. \tag{5.3}$$

Where equation 5.2 and 5.3 corresponds to two-phonon simultaneous and sequential emission respectively. We will now discuss the various terms in equations 5.1-5.3. For clarity a list of the symbols used in the above equations are given in table 5.3.

The first index in the $\langle|$ and $|\rangle$, correspond to the electronic state the excitation is in, with $|0\rangle$ being the ground state and $|i\rangle$, $|j\rangle$, $|k\rangle$ being intermediate states, as indicated by the vertices in figure 5.6. The second index represents the phononic state, where

Table 5.3: List of symbols used in equations 5.1-5.3, details of symbols used are discussed in main body of the text.

Symbol	Description
$\|0/i/j/k\rangle$	Ground state and excited states
$\|n\rangle$	Phonon state
$\hat{H}_d$	Dipole Hamiltonian
$\hat{H}_{e-p}$	Electron-phonon Hamiltonian
$\hat{H}_{e-2p}$	Electron-phonon-phonon Hamiltonian
$\hbar\omega_1$	Laser photon energy
$\hbar\omega_{i,j,k}$	Intermediate state energy
$\hbar\omega_{p1,p2}$	Phonon energy
$i\Gamma_{i,j,k}$	Broadening term

$|n\rangle$ is the number of thermal phonons in that state, which is defined by Bose-Einstein statistics. The term $|n+1\rangle$ indicates that the one extra phonon has been added to that state. The term $\hat{H}_d$ is the Hamiltonian describing the dipole that is formed by electronic excitation from the ground state, to some higher state maintaining the phonon population [137, 199]. This dipole Hamiltonian, or radiation-matter interaction Hamiltonian is fairly well-understood [200, 137] and can create an array of excitations i.e unbound electron-hole pairs or excitons [201], hence why we refer to the photon interaction as an electronic excitation to cover all possibilities. It is also the interaction responsible for the relaxation of the electronic excitation back to the ground state, emitting a photon in the process. The term $\hat{H}_{e-p}$ is a phonon interaction Hamiltonian describing the interaction between the electronic excitation and the crystal structure through either creation of destruction of a phonon, causing the electronic excitation to scatter from the excited state $|i,n\rangle$, to either another virtual or real energy state $|j,n\pm1\rangle$, which depends on whether a phonon has been destroyed or created. There are text-books [122, 202] and multiple publications [203, 204, 205, 206] on the derivation and concept of this Hamiltonian and will not be detailed in this thesis. In general, it can be understood, to first order in terms of it's phonon creation/annihilation operators.

The Hamiltonian can be understood as the total energy of the system, which changes with the atomic displacement. We can define a potential $\mathrm{V(x_i,r_i)}$, where r_i is the coordinates of the displaced atoms relative to the equilibrium position, defined as; $\mathrm{r}_i=\mathrm{r}_i^0+\delta\mathrm{r}_i$. In this case, r_i^0 is the coordinates of the i^{th} atom in the unit-cell at equilibrium position, and $\delta\mathrm{r}_i$ is the displacement. The term x_i is the coordinates of the electrons in the crystal relative to the position of the ions. For a perturbation resulting in a small displacement of the atoms we can Taylor expand the crystal potential[122, 202] as;

$$V(x_i,r_i) \approx \sum_{i=1\ldots N} V(x_i,r_{0i}) + \sum_{i=1\ldots N} \frac{\partial V(x_i,r_i)}{\partial r_i}(r_i) + \sum_{i=1\ldots N}\sum_{j=1\ldots N} \frac{1}{2!}\frac{\partial^2 V(x,r_i)}{\partial r_i \partial r_j}(r_i r_j) + O^n. \tag{5.4}$$

The first term, $\sum_{i=1...N}(V(x_i, r_{0i}))$, in 5.4, is the interaction potential at equilibrium, which is not of interest when considering atomic displacements, and can be ignored. We will continue by focusing on the first order term in 5.4 and how they relate to phonon creation/annihilation then move onto higher order terms. At this point it becomes useful to represent the displacement operator in a new basis which would also change the basis of the potential, and Hamiltonian. We convert the atomic displacement, r_i, which is a set of vectors of displacement coordinates to a set of vectors of amplitudes of normal modes[203, 206]. Where the amplitude, $(\hat{A})$, in these vectors can be written in terms of phonon creation/annihilation operators a and $a^\dagger$ [202] of wave vector k, such that;

$$\hat{A}_k = \sqrt{\frac{\hbar}{2m\omega_k}}\left(\hat{a}_k^\dagger + \hat{a}_k\right) \tag{5.5}$$

where ω_k is the frequency of the vibrational mode and m is the mass of the oscillator. This second quantization[206] allows us to rewrite the potential expressed in equation 5.4, instead of being over a sum of atomic positions, to be a sum over all vibrational modes, m, of all wavevectors;

$$\sum_{m,k} V_{m,k}(r_i)\hat{A}_k, \tag{5.6}$$

From this, the potential, which can be understood in terms of amplitudes of normal modes consisting of phonon creation/annihilation operators, can be used to rewrite the Hamiltonian in terms of these phonon operators[207]. When considering the first order expansion of the crystal potential we can combine equation 5.4 with equation 5.6 so the Hamiltonian takes the form;

$$\hat{H}_{e-p} = \sum_{m,k} g_{k,m,r_i}(\hat{a}_k^\dagger + \hat{a}_k) \tag{5.7}$$

where g_{k,m,r_i} is a notation used collecting all the other terms for the electron-phonon interaction matrix elements [207], that are not relevant in terms of the phonon creation operators [207, 202, 206]. The terms $a^\dagger$ and a are ladder operators satisfying Bose commutation rules [122], corresponding to destruction and creation of phonons by small displacements of atoms in the lattice.

In the case of a single phonon emission process, including sequential emission of single phonons, we see the Hamiltonian, $\hat{H}_{e-p}$, increases the number of phonons in a particular state by one (as we are only concerned with the Stoke's process), at each application of the operator. For the case of simultaneous emission (equation 5.2) we see the Hamiltonian corresponding to the scattering of the electronic excitation is labelled $\hat{H}_{e-2p}$. This represents the situation where higher order terms of the crystal potential [122, 208], contribute additional phonon creation operations. For example, in the case of 2-phonon emission it can be shown [207, 202] that the quadratic term in displacement part of the

crystal potential in equation 5.4 leads to squaring the creation/annihilation operators;

$$\left(a^{\dagger}+a\right)^{2}=(a^{\dagger}a^{\dagger}+2a^{\dagger}a+aa). \tag{5.8}$$

From this equation it can be seen that the in quadratic term of the potential, there are two terms which either create or annihilate 2 phonons. By extension of this, it follows that for a 3-phonon process the cubic term of the potential is used which will lead to three phonon creation/annihilation operations and so on.

Now we have detailed the terms in the numerator of each equation that physically represent the interaction of the radiation with the crystal structure, and scattering events in the crystal, we can move onto the denominator, which is predominantly responsible for resonance effects observed in materials [137]. In the denominator the first term ω_1 corresponds to the frequency of the incident radiation. The term ω_i, corresponds to the frequency of the electronic excitation in state $|i\rangle$, where Γ_i is the imaginary component of energy of the state, representing to the finite lifetime of the state itself. Likewise ω_j-iΓ_j and ω_k-iΓ_k is the frequency of the electronic excitation with it's finite lifetime after the scattering event. The denominator also contains the terms; ω_{p1}, ω_{p2}, where the first of these corresponds to the frequency of the first phonon created in the process that causes the scattering from a state $|i\rangle$ to $|j\rangle$ for a 1-phonon process (equation 5.1) and a 2-phonon simultaneous process (equation 5.2). The second frequency, ω_{p2}, corresponds to the frequency of the second phonon created through either the simultaneous emission process (equation 5.2) or as a result from the scattered electronic excitation scattering from a state $|j\rangle$ to a new state $|k\rangle$, emitting this phonon in the process, as represented in equation 5.3.

In all the expressions given, there are many possible energy states in which the photon can excite, and many states which the excitation can be scattered to. Each of these possibilities generates their own amplitude component, and therefore the total probability is square of the sum of all amplitudes for all possible configurations of the states $|i\rangle$, $|j\rangle$ and $|k\rangle$ that exist[122]. In 1D materials, because of the presence of vHs, it is likely that there are only a finite amount of available electronic states that are close in energy to the laser energy (i.e at resonance), which make a significant contribution to the total probability [4], the amplitude component of the other states therein do not contribute significantly to the sum. This will be a useful starting point in the understanding of the Raman scattering cross-section.

We will begin now by trying to understand the resonance behaviour for a one-phonon process, for simplicity we will first make the assumption there is one, discrete electronic transition. This eliminates the need to sum over many states. This assumption is reasonable when considering the vHs in 1D systems as previously mentioned. Another assumption we will make is that phonon energy is zero. This assumption is made on the basis that the energy of the fundamental phonons involved in the scattering process is measured to be much less than the than the width of the resonance. For this level of interpretation, neglecting the phonon energy is a reasonable approximation based on the

experimental observations figure shown in 5.4, as if the phonon energy was significant the result would be a double resonance which we clearly do not observe. However, in regard to fitting of the measured resonances, the phonon energy was taken into account. Based upon these assumptions we will first consider the case of one-phonon Raman and rewrite equation 5.1 to simplify the interpretation;

$$I(\omega_l) = \mid \frac{A}{(\omega_l - \omega_i)^2 + \Gamma_i^2} \mid^2 . \tag{5.9}$$

We see that the intensity of the Raman scattering (I), is proportional to some amplitude component in the numerator, and inversely proportional the square of difference between the laser energy (ω_l) and the energy of the transition (ω_i) as well as the square of the linewidth in the denominator. This equation is a double-Lorentzian like lineshape, and can be used to fit the resonances. It is clear from equation 5.9 that if a resonance condition is satisfied i.e $\omega_1 - \omega_i \equiv 0$ the strength of the Raman scattering intensity greatly increases. The only remaining term in the denominator is the lifetime broadening parameter, which means that the resonance is limited by lifetime broadening[209]. In this case it can be seen that the strength of the Raman scales as Γ^{-4}.

We are now in a position to use the resonance conditions, and assumptions imposed for the 1-phonon process and apply for multi-phonon Raman. We will concern ourselves with 2-phonon Raman, through either a sequential emission process or simultaneous, and it will be clear that the extrapolation to 3,4...n-phonons is relatively simple. In the case of 2-phonon simultaneous emission, the resonance takes the form;

$$I(\omega_l) = \mid \frac{A}{(\omega_l - \omega_i)^2 + \Gamma_i^2} \mid^2 . \tag{5.10}$$

It can be seen from equation 5.10, that at resonance, it can be written so the terms in the denominator are the same as for equation 5.9 so the Γ dependence on the Raman scattering-cross section will be the same as for the case in a 1-phonon process i.e. scales as Γ^{-4}. In the case of n-phonons in simultaneous emission, the only additional terms in the denominator corresponds to the energy of subsequent phonons, which we set to zero, no new Γ terms arise, hence for n-phonons the scattering cross-section will always scale as Γ^{-4}. It turns out that even the higher orders resonances, we do not observe any splitting of the resonances that would arise if the phonon energy played a significant role in the lineshape.

In the case of sequential emission of 2 phonons (5.3), the equation can be simplified as;

$$I(\omega) = \mid \frac{A}{(\omega_l - \omega_i)^2 + \Gamma_i^2} \mid^3 . \tag{5.11}$$

Where the power of 3 arises from the fact there is an additional intermediate state contributing another linewidth term. From this it can be seen the scattering cross-section will scale as Γ^{-6}. It is clear that upon additional phonons being emitted in the

sequential process, new terms of Γ are inserted to equation 5.3 and 5.11, and so for n phonons the scattering cross-section will scale as $\Gamma^{-2(1+n)}$. A table summarising all the Γ dependencies is presented in table **??**

Phonon order	Γ dependence on scattering cross-section	
	Sequential	Simultaneous
1	Γ^{-4}	Γ^{-4}
2	Γ^{-6}	Γ^{-4}
3	Γ^{-8}	Γ^{-4}
n	$\Gamma^{-2(1+n)}$	Γ^{-4}

Table 5.4: Table summarising the linewidth dependence of the Raman scattering cross-section as a function of the number of emitted phonons, and by which process the phonons are emitted.

By the clear distinction in the Γ term of scattering-cross section in either the regime of simultaneous, or sequential emission, it may be tempting to suggest that by investigating the intensity of the harmonics and their respective linewidths at a single temperature, it would be possible to isolate the emission mechanism. Especially as it can be seen visually from the B peaks in figure 5.1, that the intensity drop as a function of order has some trend. However, this is more complicated than it seems, as the model which would be applied for simultaneous emission does not take into account changes in the strength of the excitation-phonon interaction Hamiltonian, where it was earlier demonstrated to be different to that of a single phonon. In the case of the sequential emission, the addition of new states in the process further complicates the system and may not fit simply to the $\Gamma^{-2(1+n)}$. In addition, there is no reason that all the phonons have to be emitted either sequentially, or simultaneously, it is possible and even likely that both mechanisms play a role in the process.

Another complication to multiphonon emission is the momentum selection rules. In a single phonon emission process because of momentum conservation rules only small wavevector phonons (i.e. close to the Brillouin zone) are seen. In the case of multiphonon Raman scattering the rules are less restrictive providing the total momentum of the phonons is approximately zero allowing for $q \neq 0$ phonons.

Overall, this approach to determine the emission mechanism, is not likely to elucidate into any useful physics and hence will not be pursued. On the other hand, it is apparent that for higher order emission, in the case of sequential emission, there is a strong dependence on Γ, and it is clear that the linewidth of the resonance would narrow as a function of order, yet in the case of simultaneous emission it would remain unchanged. We will explore the details of this in section 5.6.

5.5.2 Effect of Phonon Population on Scattering Strength

Thus far we have only concerned ourselves with the linewidth dependence of the Raman scattering cross-section, and generally have not considered the number of phonons, except in regard to their fundamental creation / destruction in a scattering process. As seen in equation 5.1 and the equations for 2-phonon Raman, the term in the numerator, n, represents the number of phonons in a certain state. This number of phonons always has some value as set out by the thermal phonon population and scales with temperature by the Bose-Einstein distribution;

$$n = \frac{1}{exp(\hbar\omega/k_B T) - 1}. \tag{5.12}$$

In the case of one phonon scattering there is a population contribution to the temperature dependence of the scattering intensity, which scales linearly with (1+n)[4], due to the application of the raising or lowering operators in the interaction Hamiltonian. In the case of two phonon scattering, regardless of whether the process is sequential or simultaneous the prediction of the population contribution depends on whether the phonon creation operator creates the same single phonon mode, in which case the prediction is (1+n)(2+n). Or, whether the operator creates two different phonon modes, in which case the prediction is $(1+n)^2$. The expected temperature dependence of 1+n, (1+n)(2+n) and $(1+n)^2$ is given in figure 5.7, and was calculated using equation 5.12. From the results presented in figure 5.7 it is immediately obvious that a change in the population this would cause an increase in the Raman scattering rate, by either a factor of 5, for the case of 1+n, up to a factor of 22 for the case of $(1+n)^2$ (or a factor of 14 for the(1+n)(2+n) case). Using these results it is possible to remove the contribution of thermal phonon to the intensity of the Raman at a given temperature. To reduce any effect of changes in thermal phonon population contributing to the spectral weight of the resonance.

Based upon experimental observations shown in figure 5.3 and figure 5.5, it is clear the range of linewidths of the phonons ($\sim$0.06-0.8meV^{-1}) at the extremes limits of temperature and harmonic order (figure 5.3) are several orders of magnitude smaller than their resonances widths ($\sim$20-80meV). Based upon this, it is reasonable to assume that the probability of the phonons dephasing within the lifetime of the resonance process is small and probably won't occur. Therefore, the emission will not be into discrete phonon modes, but instead form a coherent superposition of phonon modes, which can be treated a single mode. Hence the prediction (1+n)(2+n) applies for a two-phonon process, as both phonons will have the same frequency and each emission increases the population by 1. By the same logic the population for a three-phonon process goes as (1+n)(2+n)(3+n) and so on. Based on this when considering the Raman scattering cross-section as a function of temperature, we will divide the intensity by it's corresponding phonon population at that particular temperature based on figure 5.7, to give a better sense of the linewidth dependence on the scattering rate.

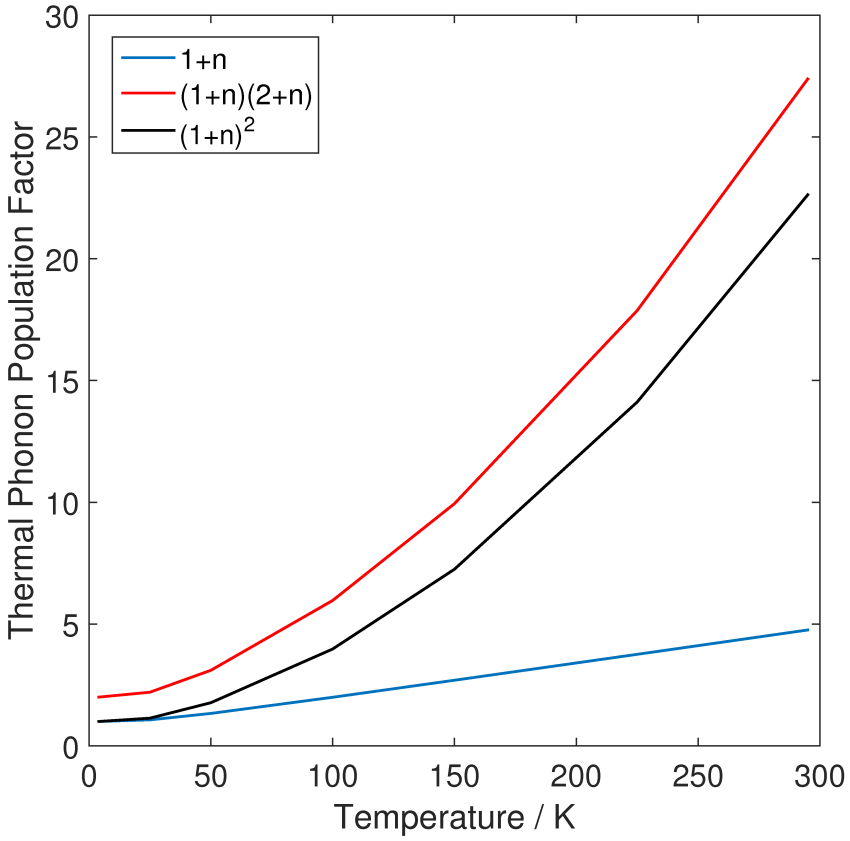

Figure 5.7: Calculated phonon population as a function of temperature for the one-phonon case (blue trace) and the two-phonon case via the two possible mechanisms (black and red trace)

5.5.3 Broadening Mechanisms

So far it has been predicted that for an incident laser energy, the same frequency as a single optical excitation, the Raman scattering cross-section scales with the linewidth of the resonance as Γ^{-4} or $\Gamma^{-2(1+n)}$. Depending on whether the phonon emission is simultaneous, or sequential, where n in this case corresponds to the number of phonons emitted (1,2,3 . . . n). Experimentally we observe two key pieces of information; 1) the resonance linewidth increases as a function of temperature and 2) the resonance intensity decreases significantly with increasing temperature. The theoretical basis discussed earlier could explain these observations, however, up to this point we have only dealt with the case that the resonance is of a discrete optical transition, and not detailed all the possible mechanisms that lead to broadening. This section discusses the mechanisms that could lead to a broadening of the optical transition/s responsible for the resonances, and discusses the physics of each and which is most likely. In general, mechanisms of broadening can be separated into two categories, these are; homogeneous broadening and inhomogeneous broadening. We will begin our discussion with the latter.

Inhomogeneous Broadening

Inhomogeneous broadening occurs in samples which consist of many similar, quantum mechanically independent sub-samples which due to variability in space or time have slightly different optical excitation energies. The response of the whole system is determined by adding up the probabilities of various responses over the distribution of the sub-samples.

In fact carbon nanotube samples are an almost ideal example of how inhomogeneous broadening can occur. They are made up of many quantum mechanically isolated individual tubes. Even tubes in close contact are strongly decoupled. If two tubes of the same type, i.e. (n,m) are in different environments whose difference effects the energy of the optical transitions then the overall absorption, Raman and other spectra of the two tubes will be the sum of the spectra for the individual tubes and the optical linewidth will be broader than that of either of the tubes individually.

If we assume in our experiments that inhomogeneous broadening was the dominant process and controlled the measured linewidth (B) of the resonance, then what would be the effect on the total Raman scattering rate. Effectively we are saying if we assume the resonance is made up of a large number of narrow linewidth transitions from the many different sub-systems. Which are spread in frequency due to inhomogeneous broadening by a factor of the resonance linewidth (B). Then the temperature dependant increase in B is due to these transitions spreading out in energy and not themselves changing in number or width. In this case, the reason the total intensity decreases is because the number of optically active states which can be excited in an energy range goes down by a factor of B. This dependence has been experimentally verified [210, 211].

It is clear this behaviour is not reconcilable within these experiments. For example, over the full temperature range we observe a factor of $\sim$3 increase in the linewidth, and a factor of $\sim$10 decrease in the Raman scattering strength. In addition it seems unlikely that inhomogeneous broadening will have a strong temperature dependence. If temperature dependent inhomogeneous broadening did occur, it would imply that the level of inhomogeneity of one area of sample with respect to another changes, which doesn't seem likely. This seems even less likely when considering over the full temperature range the central energy shifts by a few per cent, whereas the linewidth increases by a factor of 3.

Homogeneous Broadening

Homogeneous broadening refers to the broadening which occurs in a single quantum mechanical system. The regime of homogeneous broadening governs two possibilities. The first is the simplest example and corresponds to lifetime broadening of a single optical transition. This regime has already been discussed earlier. The second case is the possibility of multiple excitations close in energy, or a continuum of states. In this case the calculation must take into account the possibility of superposition of states. Which we

account for by including a sum of amplitudes each state provides over all paths before calculating the probability.

As we have already considered the lifetime broadening scenario in the extreme, let us now consider the other extreme case of homogeneous broadening in which the broadening due to the continuum of states is much greater than the lifetime broadening. In this case the temperature dependent linewidth would imply that the underlying quantum mechanics of the system was changing leading to a broader continuum of electronic states without significantly changing the average energy of the electronic states. This is unlikely but possible. However if it was to occur it would lead to the same dependence of the Raman intensity on the resonance linewidth as already calculated for the single optical transition.

Mixed Broadening

Up to this point we have discussed cases where one mechanism contributes solely to the linewidth and has a temperature dependence. Let us now consider the possibility that there is multiple mechanisms broadening.

One example would be of a lifetime broadened inhomogeneous broadening. As with the lifetime broadened example, the total scattering rate would scale as Γ^{-4}, however,the amount of lines that can be optically excited increases with Γ leading to a Γ^{-3} dependence. Another example of this would be a lifetime broadened continuum of states. In this case, a change in the underlying optical transition resonance would not greatly alter the total Raman scattering rate. This can be understood by examining figure 5.8. If the excitations responsible for the overall resonance were to homogeneously broaden, but not greatly shift the central energy of the resonance (which is believable based on temperature dependence of the central energy in figure 5.5). Then the resonance would scale inversely proportional to the linewidth, because the amount that each contributes decreases. However, in this regime the number of states available increases linearly with the linewidth. This effectively cancels the inverse behaviour leading to no net change in the overall resonance scattering cross-section. However, this logic requires the assumption that all the broaden in energy in the same way, and that the linewidth of the state is much less than the linewidth of the resonance. In both cases this is believable based on the data.

In principle all or a combination of the above mechanisms will play some role in the spectra presented in this work, and the relative dominance of the mechanisms may change as a function of temperature. However, as we will see later, it seems likely that the linewidth through out the temperature range is dominated by coherence lifetime broadening. We have two key pieces of experimental evidence which can help us to try and clarify the theoretical situation; the temperature dependence of the resonance width and maximum amplitude. As illustrated in fig 5.5, all of the resonances broaden with increasing temperature. Of the three mechanisms which can lead to resonance broadening, coherent

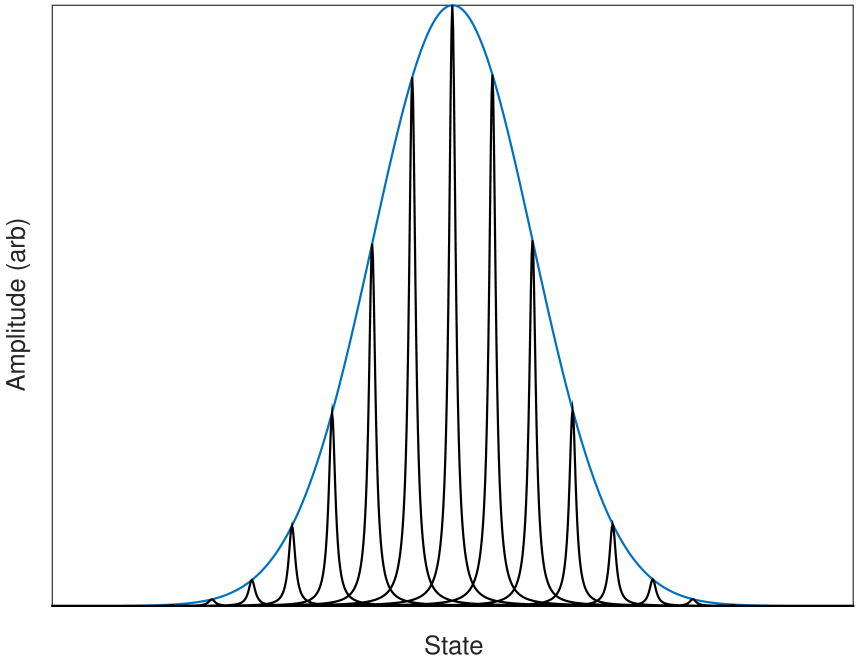

Figure 5.8: Illustration of multiple homogeneously broadened states close in energy, contributing an amplitude component to the overall resonance observed.

lifetime broadening is the one most likely to lead to a temperature dependent linewidth. If we make the assumption that the other two mechanisms; inhomogeneous broadening and broadening due to a continuum of states, are not temperature dependent. Then at higher temperatures we can be relatively confident that the linewidth is dominated by the coherence linewidth of the underlying electronic states and we can effectively treat the resonance as being due to a discrete optical excitation. We will now analyse the data in terms of the theoretical behaviour for both cases of multi-phonon emission, with the underlying assumption that the broadening is coherence lifetime dominated.

5.6 Interpretation of Data Based on Theoretical Models

Now we have demonstrated there is a quantitative difference between the various models, we are in a position to interpret these models when applied to the data. As stated earlier, multiple phenomenological fits were applied to the resonance data and it was found that Gaussian lineshape was marginally the best. This is illustrated by the data presented in figure 5.9 which shows the 4K resonance data of the B mode fitted to a Gaussian, a Lorentzian and a double Lorentzian. The R^2 values of the fits are presented in table 5.5. This section will now discuss the various fits applied to the resonance data, and their interpretation. We will begin by dealing with the Gaussian fits discussing all the physics and interpretations to this case. The section finishes by presenting the equivalent fitted

data for the sequential or simultaneous emission model, highlighting the differences and similarities and demonstrating that the choice of model does not alter the conclusions.

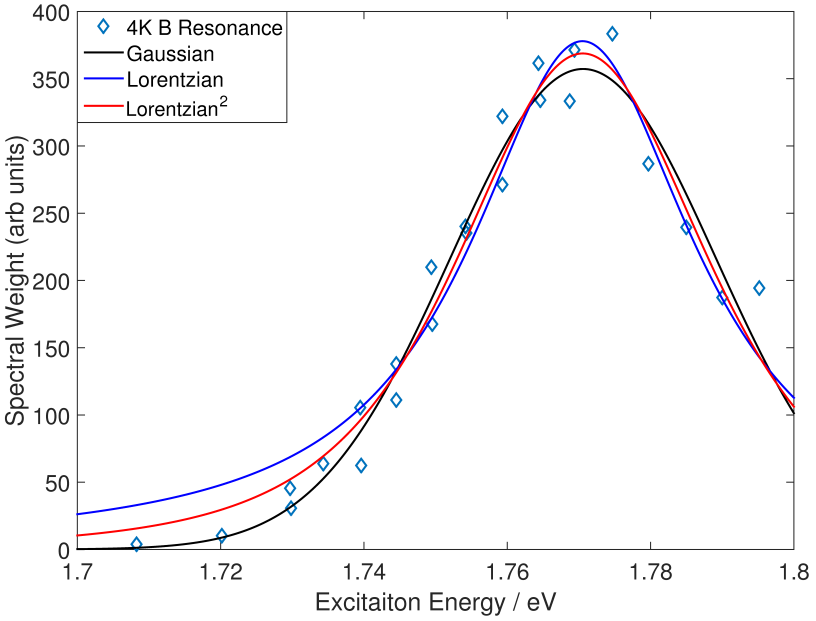

Figure 5.9: 4K resonance data of B mode fit to a Gaussian, Lorentzian and double-Lorentzian lineshape. It is clear that there is no great difference between the fits applied and by the R^2, the Gaussian is marginally the better fit, hence why it was initially chosen to fit the data.

Table 5.5: R^2 values based on least squares fitting of the B resonance data at 4K to the various lineshapes.

Lineshape	R^2
Gaussian	0.9692
Lorentzian	0.9516
Double-Lorentzian	0.9672

5.6.1 Gaussian Lineshapes

Whilst Raman is a relatively well-understood process, the physics of multiphonon emission can become complicated quickly. It has been discussed that it is not simple to predict the true form of the resonance without prior knowledge of the resonance. Up to this point we have only applied Gaussian lineshapes to fit the data, this is presented in figure 5.10. The Gaussian lineshape was chosen to parametrise the amplitude, central energy and width of the resonance. As demonstrated in the previous section, the Gaussian produced a marginally better fit. This section discusses the physics of the data presented in section 5.4 and how this can be understood in terms of coherence lifetime broadening of the underlying transition.

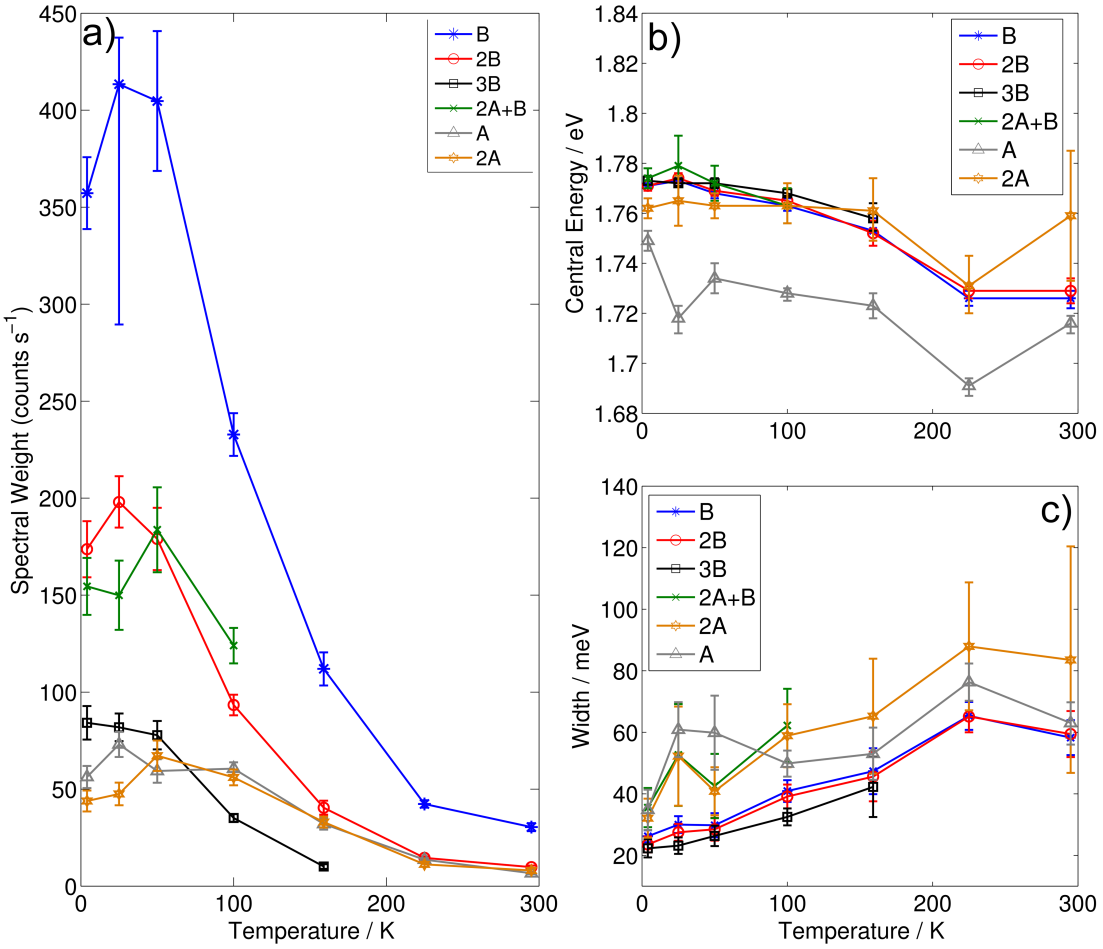

Figure 5.10: Extracted parameters of the Gaussian fit applied to the A, B, 2A, 2B, 2A+B and 3B modes as a function of temperature. Panel (a) shows the spectral weight of the resonances, b) the central energy and c) the fitted width. The error bars in each panel are associated with the 95% confidence bounds arising from the fitting.

5.6.1.1 Resonance Shift

Panel b of figure 5.10 presents the central energy of all the observed resonances as a function of temperature. By inspection of the data presented in this figure, it can be seen that most of the modes are resonant at the same basic energy, with the exception of the A resonance which is notably red shifted. It is also clear from this figure, that as temperature is increased there is a red shift of all the modes by approximately the same rate. As explained earlier, this red-shift is likely due to lattice expansion as temperature is increased. It stands to reason that if all the resonances were from the same crystal structure, then they should also have a comparable red-shift. The clear difference between the resonance energy of the A feature and the others highlights the fact that the underlying physics behind the optical transition is more complicated than it first seems.

This is because although we observe combination modes of the A and B features implying they are from the same crystal structure, the resonances imply a different electronic structure. We will explore this in more depth later.

5.6.1.2 Resonance Width

Most importantly for the interpretation of the data is the linewidth of the resonances, as it underpins the theory behind lifetime broadening. Figure 5.10 (c) shows the fitted resonance linewidths, which all clearly increase as a function of temperature. In this model, the width of the B, 2B and 3B resonances all increase at the same rate (a factor of 3 between 4K and 225K). In addition it seems that at a given temperature, the linewidth narrows as a function of order, this is most pronounced at higher temperatures. However, due to the error bounds from the fitting, we cannot be certain of this. With the A, 2A and 2A+B, it can be seen they all increase at higher temperatures, and the that 2A+B and 2A are the same to within the errors. It appears that the 2A is broader than the A, where this is most apparent at higher temperatures. However, like with the B resonances, we cannot be certain of this due to the uncertainty from the fits. Overall the evidence from the linewidths suggest the emission mechanism for the multiphonon Raman resonances is simultaneous, however we cannot exclude the possibility of sequential emission. We will explore further in section 5.6.2.

5.6.1.3 Spectral Weight

It is clear from figure 5.10 (a) that the spectral weight of all resonances decreases at the extreme limits of temperature. In some intermediate temperatures (below 50K) there seems to be some increase, however in these cases we cannot be certain due to the errors. Overall, it is clear that at the extremes of the temperatures ranges probed (4K-295K) all of the resonances drop off by a significant portion, at least a factor of 5 (for the 2A) and up to a factor of $\sim$17 (for the 2B resonance). This decrease is contrary to the expected behaviour of the resonance intensity if it was dominated by the thermal phonon population. In order to better understand the change in spectral weight, we will first remove any temperature dependent phonon population effect.

Correcting for Thermal Phonons

As mentioned earlier in section 5.5.2 the amplitude of the fit contains the electron-phonon interaction Hamiltonian which in turn contains a term for the thermal phonon population, which scales with temperature. The calculation for the thermal phonon number (1+n) is relatively simple, and can be applied to the observed spectral weight to normalise out the contribution of thermal phonons. The value of 1+n was calculated using the equation in section 5.5.2 for each phonon mode at each sample temperature. For

higher order resonances the calculation was done under the both the assumptions that a) the phonons emitted were coherent, meaning the calculation was (1+n)(2+n) and (1+n)(2+n)(3+n) for the 2A, 2B and 2A+B and 3B resonances respectively. Or b) the phonons were incoherent meaning the calculation was $(1+n)^2$ for 2A and 2B and $(1+n)^3$ for 2A+B and 3B. Figure 5.11 presents the log of the spectral weight, corrected for by the thermal phonon population for both scenarios. As can be seen from the thermal phonon

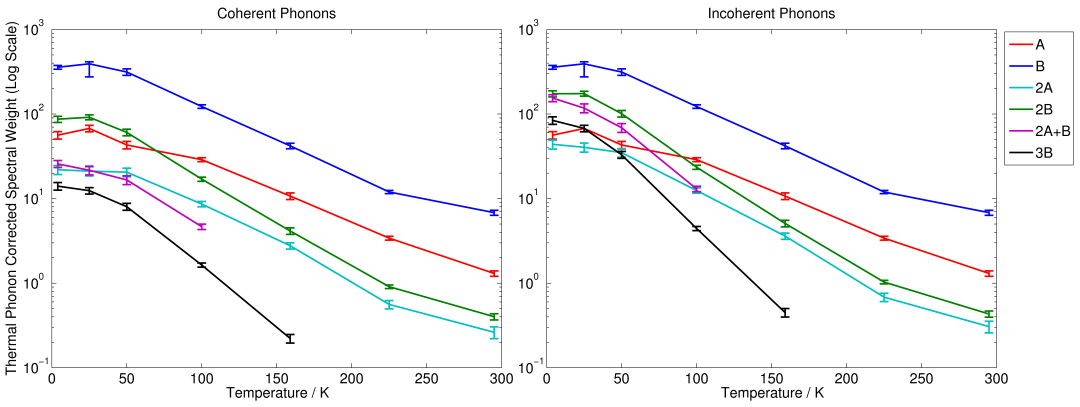

Figure 5.11: Log of the phonon population corrected spectral weight as a function of temperature. Errors are from the 95% confidence bounds of the fitting. Left panel shows corrected spectral weight assuming phonons are into the same mode. The right panel is the correction assuming the phonons are emitted into multiple modes.

corrected spectral weight in figure 5.11, it does not matter which correction factor is applied as it does not significantly alter the conclusion that the spectral weight decreases with increasing temperature. In fact, by correcting the for thermal phonons the drop off in intensity is even more significant. Where for the case of the 2A resonance which decreased by a factor of 5 between 4K-295K now drops off by a factor of ∼80 over the same range. Likewise, the most pronounced decrease is the 2B resonance which drops off by a factor of ∼210 between 4K and 295K. Finally the few cases of increasing spectral weight at higher temperatures seen in figure 5.10 are significantly reduced in both cases from figure 5.11, so can likely be entirely explained in terms of thermal phonon population increasing.

Interestingly, the phonon correction factor has the effect of seemingly levelling out the spectral weight for all the resonances between 4K-50K, it is unclear what causes this effect but is likely related to the linewidth which exhibits similar effects up to this temperature.

5.6.1.4 Interpretation of Gaussian Fits

Using the Gaussian model, and applying the thermal phonon corrections discussed previously, we are now in a position to explore the correlation between the resonance linewidth

and intensity separate from any thermal phonon population effect. We present plots of the log of the spectral weight corrected for the thermal phonon population versus the log of the B resonance width for the B, 2B and 3B peaks in figure 5.12. The (a) and (b) panels cover both of the phonon population scenarios already discussed i.e. coherent and incoherent. Also shown are best linear fits to the various data sets; the best fit slopes and their 95% confidence limits are presented in table 5.6. This will in principle allow us to understand the emission mechanism based on the gradient of the straight line fit applied to the data.

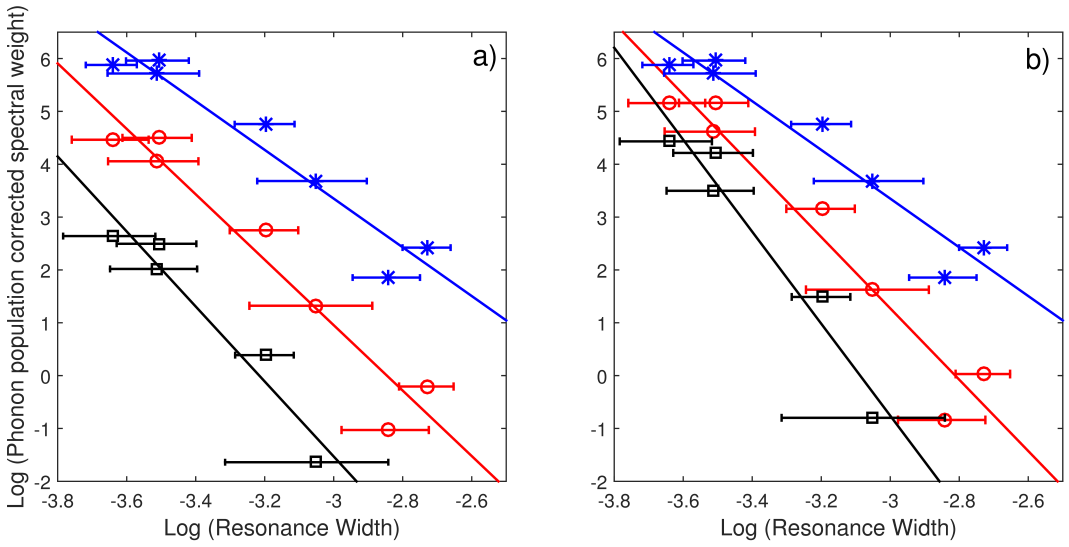

Figure 5.12: Log of the phonon population corrected spectral weight as a function of the changing resonance width of the B mode. Panel a) shows the phonon correction of (1+n), (1+n)(2+n) and (1+n)(2+n)(3+n) for the B, 2B and 3B resonances. Panel b) has been corrected for using (1+n), $(1+n)^2$ and $(1+n)^3$ for the B, 2B and 3B respectively. In each panel of the figure the blue stars, red circles and black squares are the data for the B, 2B and 3B resonances respectively. Error bars in the x-axis are associated with 95% confidence bounds from the Gaussian fit of the linewidth, errors in the y-axis are to small to be visually clear on this plot and have been omitted.

The results of the linear fits indicate that the best explanation for the temperature dependence of the Raman scattering intensity is the model which assumes that the B, 2B and 3B resonances can be treated as being due to a single optical transition which is coherent lifetime broadened and that the phonon emission in the higher order harmonics likely occurs sequentially. It is clear that the results cannot be explained in terms of a temperature dependent inhomogeneous broadening and that the width of the transitions cannot be dominated by a continuum of optical transitions. However it is not entirely possible to exclude the possibility of simultaneous emission of phonons based on confidence bounds of the straight line fit presented in table 5.6. By comparison of the two possible thermal phonon correction cases, both scenarios yield similar gradients with similar uncertainty. Upon more detailed inspection however, it appears that the upper

Table 5.6: Fitted data from figure 5.12 with 95% confidence intervals from the fits for both the thermal phonon correction cases. Case I corresponds to the fits from Fig 5.12 a), case II corresponds to the thermal phonon correction from Fig 5.12 b).

Label	Thermal phonon correction I			Thermal phonon correction II		
	Lower 95%	Value	Upper 95%	Lower 95%	Value	Upper 95%
A	-9.5	-3.5	-2.5	-9.5	-3.5	-2.5
2A	-11.7	-4.4	-2.7	-12.9	-4.9	-2.9
2A+B	-6.2	-3.7	-1.2	-9.1	-5.3	-1.4
B	-6.0	-4.6	-3.1	-6.0	-4.6	-3.1
2B	-8.0	-6.2	-4.3	-8.7	-6.7	-4.7
3B	-10.4	-7.1	-3.7	-12.4	-8.7	-4.9

confidence bands of the gradient for the B, 2B and 3B case through phonon correction case I allows for the possibility of simultaneous emission. Whereas the upper confidence bands for the 2B and 3B in case II do not allow for this, or at least extremely unlikely base upon the data. Overall it seems that there is no great difference in which thermal phonon correction case is applied as both produce data that don't disagree with one another. Whilst we cannot be certain of the emission mechanism, the data in both scenarios supports the hypothesis that the intensity is controlled by a temperature broadening of the coherence linewidth of the underlying transition.

In conclusion, the Gaussian line provides a good fit to the data, and allows us to understand the physics of underlying optical transition. The results presented in figure 5.12 support the hypothesis that the optical transition responsible for the Raman resonance width is dominated by coherence lifetime broadening over most of the temperature range down to at least 50K. If this is the case then it should be possible to determine the coherence lifetime from the linewidth. As the conversion factor for the harmonic peaks depends upon whether the phonon emission is simultaneous or sequential, we analyse the B peak alone. In this case we obtain estimates of the coherent lifetime for the underlying optical transition of 9fs at 295K and 18fs at 50K, by using the formula $\tau = \hbar/\Gamma$. Whilst this value of the coherence lifetime seems very short, it is not unreasonable when considering the coherence lifetime of the inner wall of a double-walled carbon nanotube has a coherence lifetime of ∼25fs at 80K [189]. There seems to be contradictions in the data, that whilst the behaviour of the linewidth suggests a simultaneous emission mechanism, the data from figure 5.12 favours sequential emission. However, due to the uncertainty we cannot be sure of either these interpretations at this level. The next section will discuss this in greater detail.

5.6.2 Alternative Multiphonon Lineshapes

From the interpretation of the data based on the Gaussian model, we have not been able to definitively isolate the emission mechanism for the multiphonon emission. In

addition, from the models presented earlier in section 5.5.1, it is clear that the forms of the resonances for n-phonon resonances are different depending on whether the emission is simultaneous or sequential, and does not take the form of a Gaussian but a Lorentzian like lineshape. This section presents the same resonance Raman data, however the data has been fit using the models for simultaneous emission (5.10) and sequential emission (5.11). In both cases we have removed any Γ dependence from the numerator of both equations to ensure any change to the Raman intensity is likely to be associated with changes in linewidth. This process will allow us to demonstrate that the conclusions we are able to draw based upon the data are not contradicted by which model we apply. Further supporting the statement the Gaussian is a reasonable fit and the observations in the data could be understood in terms of temperature dependent coherence lifetime broadening.

5.6.2.1 Central Energy

We begin the interpretation with the central energy of the resonances. It stands to reason that through either model the fits should yield basically the same central resonance energy, which again should be equivalent to the Gaussian fits.

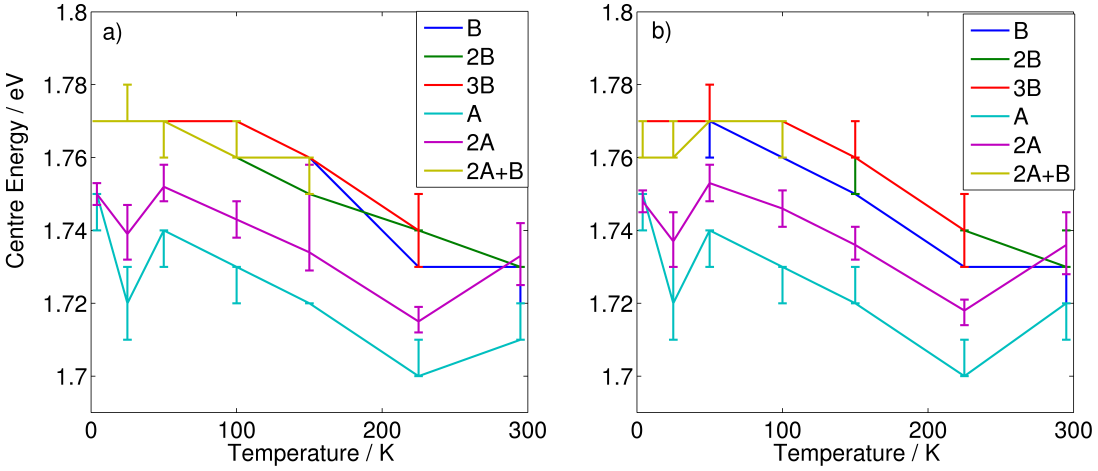

Figure 5.13: Fitted central energy for the a) sequential emission model and b) simultaneous emission model. In both panels the error bars are 95% confidence bands from fitting process.

It is clear from inspection of figure 5.13 that in both panels there is a softening of the resonances at higher temperatures, and through both models the softening and fits are basically the same. When compared to the equivalent Gaussian lineshape there are several observations. First of all it is clear that the A, B, 2B, 2A+B and 3B modes are at the same basic energy to within errors. However, there does appear to be a difference between the 2A central energy, which is slightly red shifted from the Gaussian fits by on average 18.6±0.6meV at each temperature. The exact cause of this difference

is uncertain, and may be due to the phonon energy, however we don't observe this in the other resonances. Despite this observation, the overall trend of a red-shift as a function of temperature is the same for a Gaussian model and can be understood in terms of lattice expansion.

5.6.2.2 Resonance Linewidth

One of the most notable differences between multiphonon emission for sequential or simultaneous emission is the order of power on the linewidth at higher number of phonons. Figure 5.14 presents the fitted linewidth for a) the sequential model and b) the simultaneous model. It is clear from both panels that as temperature increases the linewidth also increases. Out of the two models the one most similar to the Gaussian equivalent is panel b (simultaneous emission model). In this model it could be argued there is some narrowing of the resonance linewidth as a function of order, this is most notable at low temperature (below 50K) for the B resonances, but we cannot be certain of this to within the confidence bands of the fit. Despite the errors being large, it is fairly clear that in panel a, the resonance width broadens as a function of order. This observation is unexpected as the fitted linewidth should be invariant at higher order for both models. This observation suggests that the more likely emission mechanism is simultaneous. However, it is hard to reconcile these differences between the error bars from the fits. Whilst there is some differences in the absolute values of the width between the two models, with the sequential (panel a) being slightly broader, they are not radically dissimilar, nor very different from the Gaussian equivalent.

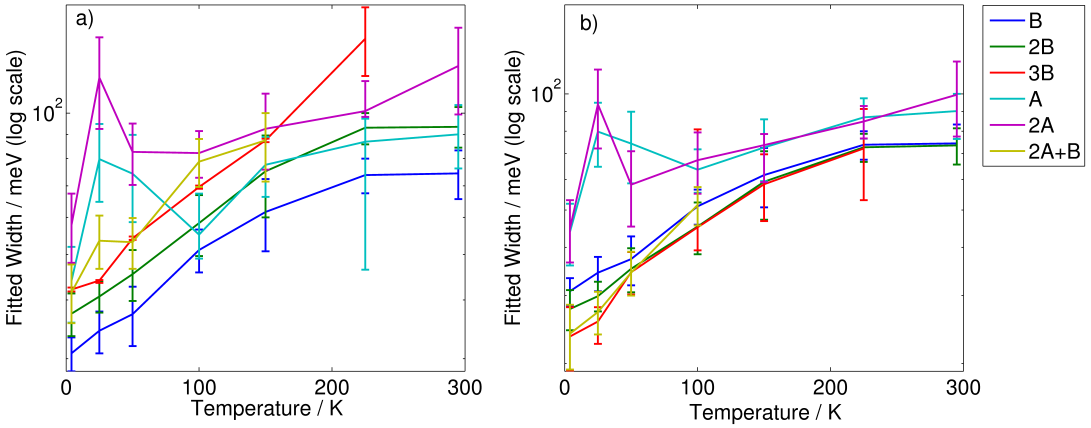

Figure 5.14: Fitted resonance width for the a) sequential emission model and b) simultaneous emission model. In both panels the error bars are 95% confidence bands from fitting process.

Overall we have demonstrated that the resonance linewidth increases for both models, and that the simultaneous emission model seems to agree better with the Gaussian equivalent than the sequential. Whilst the absolute value of the widths differ slightly, they are

still on the same order of magnitude. This suggests that the calculation for the coherence lifetime using the simultaneous/sequential emission model will not be significantly different from the calculated lifetime using the Gaussian linewidths.

5.6.2.3 Resonance Amplitude

Figure 5.15 presents the fitted amplitude for the sequential (panel a) and simultaneous model (panel b). In both cases these fits are clearly visually different from the Gaussian equivalents. This is to be expected, as when fitting the data to equation 5.10 and 5.11, we have deliberately removed any explicit Γ dependence in the numerator, leaving only an amplitude component. The fact that variation in the amplitude is less than an order of magnitude, highlights the fact that the observed decrease in resonance intensity, is clearly controlled by the linewidth, Γ. We will begin our discussion with panel a, which presents the sequential emission model. In this case we can clearly see that there is no significant change to the amplitude of any of the resonances at the extremes of temperature. The 2A+B and 3B traces have no error bars due to fitting limitations and vary more significantly. However, if the error bars were comparable to the other features it would follow the trend. There is one anomaly associated with the 25K data point for the 2A resonance, however it does not detract from the overall trend. In some cases it can be seen that there is a slight increase in amplitude as a function of temperature, this is likely associated with thermal phonon populations and we will correct for this shortly. In the case of panel b, the increases in amplitude are more pronounced up to ∼100K for the B, 2B 2A+B and 3B resonances and it is fairly clear the A resonance decreases. We will continue the discussion of both these data sets after removing the thermal phonon population component as previously described.

Thermal Phonon Correction

As discussed earlier (section 5.5.2), the amplitude parameter has no explicit Γ term, but does posses an intrinsic dependence on the thermal phonon population. In principle it is possible to correct for the phonon population by dividing the amplitude component by the corresponding population for a particular phonon energy at a distinct temperature. This thermal phonon population factor was calculated for each resonance at each temperature assuming the phonon emission was coherent, using (1+n) for A and B, (1+n)(2+n) for 2A and 2B and finally, (1+n)(2+n)(3+n) for 2A+B and 3B. The thermal phonon corrected amplitude is presented in figure 5.16. As can be seen from the data presented in figure 5.16, correcting the amplitude by the relative population of thermal phonons does not significantly alter the trend for the sequential emission model (panel a), however does seem to flatten out some of the increases in amplitude at higher temperature. In the case of sequential emission, correcting for thermal phonons seems to linearise the data causing little variation of the amplitude component of any of the resonances at the extremes of sample temperature.

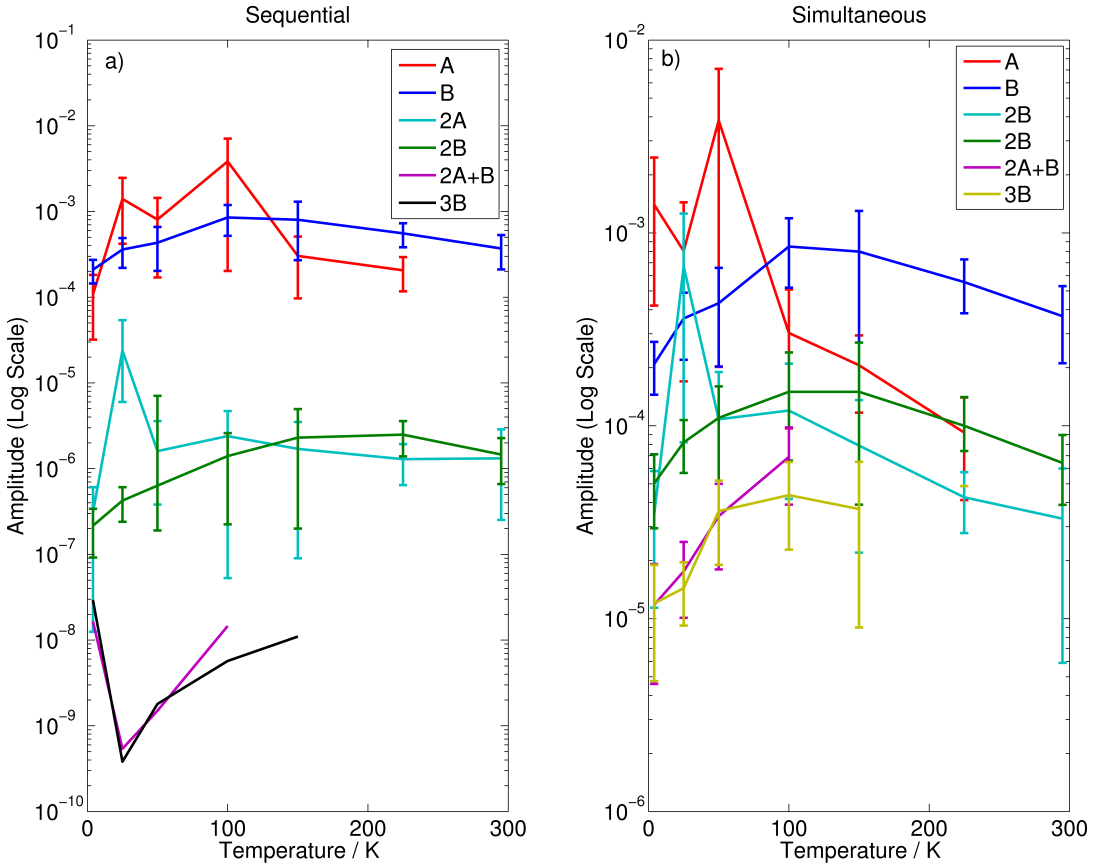

Figure 5.15: Log plot of amplitude for the a) sequential emission model and b) simultaneous emission model. In both panels the error bars are 95% confidence bands from fitting process. In the case of the 3B and 2A+B traces in panel a) no confidence bounds were determined due to computational limits.

Panel b which shows the thermal phonon corrected simultaneous model still has some changes, which become more pronounced. The amplitude of all resonances clearly decreases at higher temperature. Despite this, the magnitude of decrease is not the same for this when compared to the Gaussian, for example the B resonance in panel b of figure 5.16, decreases by a factor of 2.5, compared to the factor of 50 for the Gaussian fit of B resonance. It is fairly clear that the sequential emission model provides a better fit for the data in terms of linearising the amplitude component. This observation does not disagree with the observations from figure 5.12 which suggest sequential emission is the likely mechanism. In regard to panel b, in principle the amplitude component also contains more information, for example, it is possible there is a temperature dependence on the electron-phonon interaction Hamiltonian. However, we are not able to explicitly correct for this, and it may hint at something more complex about the nature of the resonances. This may also apply for the A resonance in panel a. Overall the thermal phonon corrected fitted amplitude does not disagree with the Gaussian fits, and the lack of variation in panel a supports the Gaussian fitted data in figure 5.12, hinting the emission mechanism may be sequential.

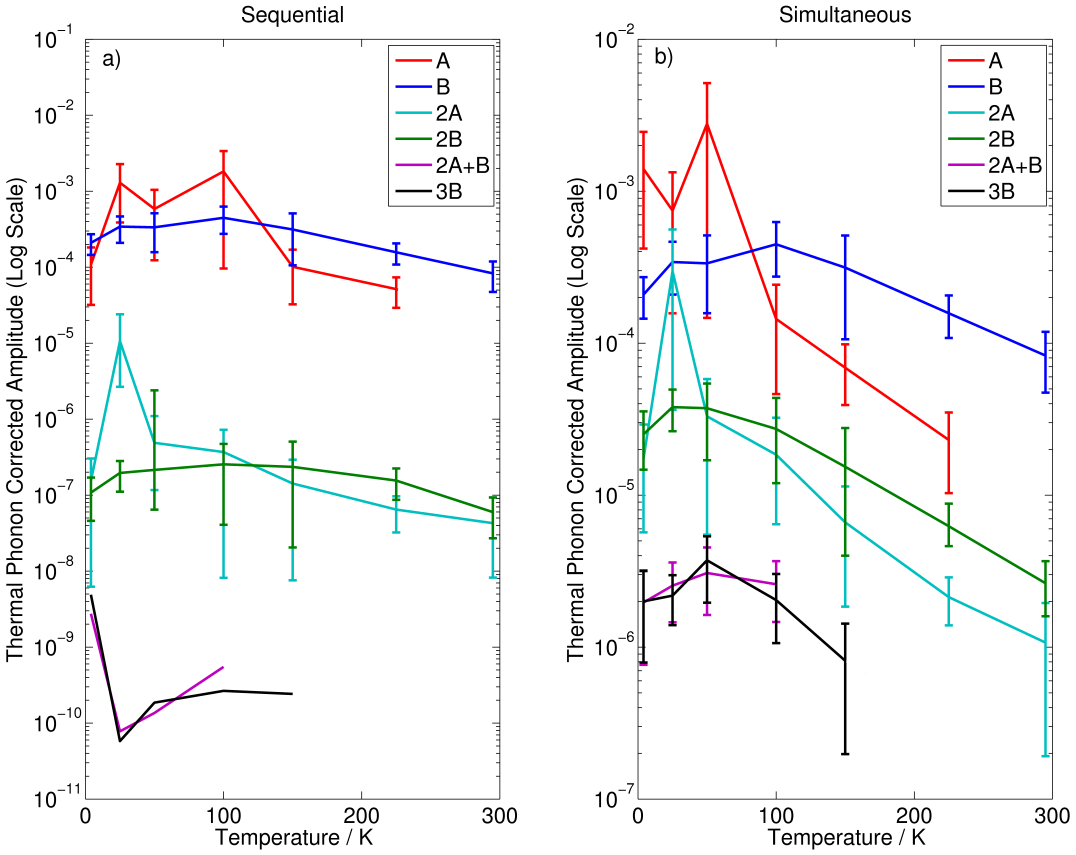

Figure 5.16: Log plot of thermal-phonon corrected amplitude for the a) sequential emission model and b) simultaneous emission model. The phonon correction factor was applied to each resonance calculating their corresponding thermal population at each temperature for each phonon energy using the form (1+n) for the A and B, (1+n)(2+n) for the 2A and 2B and (1+n)(2+n)(3+n) for the 2A+B and 3B. In both panels the error bars are 95% confidence bands from fitting process. In the case of the 3B and 2A+B traces in panel a) no confidence bounds were determined due to computational limits.

5.6.2.4 Comparison of Models

By direct comparison of both the sequential and simultaneous emission models we have demonstrated that central energies of the resonances is independent of the model applied and can be understood due to lattice expansion. We have also demonstrated that the amplitude component of the fit favours a sequential emission mechanism. However, because the variation in amplitude for simultaneous is much less than the change observed in the spectral weight, we cannot be certain of this. The amplitude data in both emission mechanisms does not directly contradict the Gaussian equivalents and supports the claim that the Raman intensity is controlled by the linewidth.

It appears that the linewidth of the Gaussian model behaves in a similar way to the simultaneous emission, and the fact the resonance width at any given temperature remains

basically the same supports the hypothesis that the emission mechanism is simultaneous rather than sequential. Based on the contradictions and uncertainty in evidence presented in the data, it seems impossible to isolate the emission mechanism into an either sequential or simultaneous basis, when in all possibility the emission mechanism can be a combination of both. We have also demonstrated that the models for multiphonon emission don't provide any more or less information that the Gaussian fits, and that a calculation of the coherence lifetime using the Gaussian linewidth is a reasonable approximation of the lifetime.

5.7 Conclusion

In conclusion this chapter presented the first in depth study of the temperature and excitation energy dependence of the Raman scattering from extreme HgTe nanowires with a diameter corresponding to two atoms. Specifically the main objectives were to measure the temperature dependence of centre shift and line-width of the two main phonon modes at 47 and 51 cm^{-1} and their overtones as well as to understand the temperature dynamics of the resonances observed. The energy dependence of the Raman spectra shows a strong clear resonance which red shifts with increasing temperature. There is clear evidence that this resonance is associated with a single line, which may allow for the possibility of a narrow band of states. As might be expected for a 1D system with strong van Hove singularities[4], or more likely strong excitonic effects [141]. There is strong support for the hypothesis that at temperatures above 150K the resonance width is dominated by the coherent lifetime broadening of the underlying optical transitions. The intensity of the Raman scattering from the extreme nanowires has a very strong temperature dependence, dropping by more than an order of magnitude from 4K to room temperature. This effect is even more pronounced once the thermal phonon population is corrected for. This observation combined with the strongly resonant nature of the Raman scattering is presumably why Raman from HgTe fillings of SWCNTs haven't been observed before despite a few Raman studies having been performed on such samples. Whilst the data is not totally conclusive, it seems highly likely that the reason for the temperature dependence is the decrease in the coherence lifetime of the optical transitions responsible for the resonance. If this is the case then this chapter demonstrates that Raman scattering provides an opportunity to study not only the scattering of the electronic states by phonons but also due to a wider range of mechanisms. One outstanding issue that cannot be reconciled by the current data is whether the multiphonon peaks are due to sequential or simultaneous emission of phonons. Based on all the evidence presented by fitting different models, we gain no unique advantage in terms of information by fitting either a Gaussian or Lorentzian like lineshape. Based on the Gaussian fits we were able to calculate the coherence lifetime of the underlying optical transition responsible for the B resonance to be 9fs at 295K and 18fs at 50K, which is

comparable to the inner wall of DWCNTs.

At this point it is interesting to compare the results here with Raman scattering from related systems. The most notable system being the well-understood 1D material, SWCNTs themselves. These share the strongly resonant behaviour seen in the HgTe nanowires. However due to the range of possible SWCNTs conformations it is nearly always likely to observe Raman from some tube or other at any specific excitation wavelength. In the case of filled tube Raman however this is not the case and without exploring a wide range of excitation wavelengths it may not be possible to see anything in the Raman spectrum due to the filling. In this regard the strong Raman resonances as a result of strong excitonic effects makes nanotubes and extreme nanowires very similar, and may hold further prospect to model such extreme nanowires as Luttinger liquids like their nanotube counterparts [61]. In addition it seems likely that the optical transitions responsible for the resonance data may be excitonic in nature. However, it is also interesting to note that the resonances in SWCNTs are not strongly temperature dependent and there is no real advantage to cooling down SWCNTs to obtain their spectrum, yet in the case of HgTe nanowire case 4K measurements are far preferable and arguably essential for preliminary characterisation of such structures. The real interest in this work, is as to whether the strong temperature dependence is unique to this particular HgTe crystal structure, or perhaps more global to a whole family of extreme nanowire materials, it seems more likely the latter to be the case.

Chapter 6

Conclusions and Outlook

The aim of this thesis has been to report on new Raman modes attributable to a novel form of HgTe just two atoms in diameter. It reports strong resonances associated with the HgTe peaks, and explains the peaks observed as to be due to four fundamental vibrational modes. We investigate the mechanism which controls the linewidth broadening that results in the decrease in rate of Raman scattering as a function of increasing temperature. This work has yielded new information on the electronic properties of extreme nanowire systems.

This thesis has presented the first in depth study of the temperature and energy dependence of the Raman scattering from extreme HgTe nanowires with a diameter corresponding to two atoms. In chapter 4 we presented the results from resonance Raman experiments on the HgTe@SWCTNs sample at 4K where the measured spectra contain a large number of features not observed in bulk HgTe or unfilled SWCNTs. These features can be separated into 4 fundamental modes at 47, 51, 94 and 114 cm^{-1} plus the overtones and combinations of the first three of these modes. The polarisation dependence of all measurable features were shown to be consistent with nanowire Raman. Through resonance Raman spectroscopy we demonstrated the Raman peaks had clear resonances, which along with future theoretical interpretation may allow for better understanding of the electronic states involved in the resonances and/or extra details on the electron-phonon interaction. We measured the excitation energy dependence of centre shift, linewidth and Raman scattering cross-section of the two main Raman peaks at 47 and 51 cm^{-1} as well as their overtones. It was demonstrated that there is no clear change to the Raman shift or linewidth of the peaks as a function of energy. However, the resonance profiles do clearly change with excitation energy showing a red-shift of the resonances and a slight broadening as the excitation energy decreases.
These results are supported by DFT calculations, which although they do not include excitionic effects, are consistent with the observed experimental data. The calculations

predict a band-gap for HgTe nanowires of 1.35eV; however, they also predict other transitions at energies of 1.5 and 1.75eV which are candidates for the resonant optical transition. In addition to within the uncertainty of the calculations it is possible that the resonance observed is associated with the fundamental band-gap of the material.

In chapter 5 we presented the temperature dependent resonance Raman spectroscopy experiments on the nanowire structure to better understand the decreasing rate of Raman scattering as temperature is increased. It was shown that the resonance of the peaks red shifts and broadens with increasing temperature. There is clear evidence that this resonance is associated with a narrow band of optical transitions as might be expected for a 1D system with strong excitonic effects. There is strong support for the hypothesis that at temperatures above 150K the resonance width is dominated by the coherent lifetime broadening of the underlying optical transitions. The intensity of the Raman scattering from the extreme nanowires has a very strong temperature dependence dropping by more than an order of magnitude from 4K to room temperature. This combined with the strongly resonant nature of the Raman scattering is presumably why Raman from HgTe fillings of SWCNTs haven't been observed before despite a number of Raman studies having been performed on such samples. Whilst the data is not totally conclusive, it seems highly likely that the reason for the temperature dependence is the decrease in the coherent lifetime of the optical transitions responsible for the resonance. If this is the case then Raman scattering gives us an opportunity to study not only the scattering of the electronic states by phonons but also due to a wider range of mechanisms.

As set out in the thesis it is not entirely clear from the results whether multiphonon Raman in the HgTe nanowires is due to sequential or simultaneous emission of the phonons; this is a question which has been open for bulk semiconductors for at least 40 years [212, 213]. The temperature dependence of the scattering strength suggest that sequential emission is more likely however the relative linewidth of the different resonances suggest that simultaneous emission is more likely. It is clearly possible for both mechanisms to be active at the same time and this may explain the apparent contradiction between the two aspects of the data.

In general the results add to the understanding of coherence related effects in 1D systems. The agreement between the results presented here and the equivalent measurements on carbon nanotubes suggests that despite having 1D of freedom, the optical transitions in both systems can be treated as coherently broadened transitions with discrete energies. It also suggests that the underlying physics of the transition is due to excitons rather than van Hove singularities, as is true with SWCNT systems. It is not clear as to the direct practical applications of the coherence of optical transitions in 1D systems, however the optical properties of carbon nanotubes is generating a huge amount of interest[214] and small diameter nanowires such as the ones investigated in this thesis are likely to bring additional new information to the field of carbon nanotube technology.

Overall, these results have general implications for the application of Raman scattering to nanowires. In particular these results indicate that for some nanowire systems that

low temperature Raman measurements may be required in order to obtain a measurable spectrum. The lack of strong temperature dependence of Raman in 2D and 3D systems means that the practical difficulties of cryogenic sample environments are commonly not worth the effort. This may not be the case in 1D systems. Another more general point is that the temperature dependence of the intensity of Raman scattering does not receive sufficient attention. A clear example of this is from the temperature dependant Raman spectra in literature reported on carbon nanotubes, which could contain significant physics, but hasn't received a large amount of attention. Whilst measuring the temperature dependence of the intensity is more challenging than measuring the temperature dependence of the other peak parameters it can be done with a reasonable accuracy with enough care and attention and can further elucidate the physics of the system being investigated.

6.1 Perspectives

The main goal in this thesis was to better understand the optical transitions of a particular extreme nanowire system. Whilst this objective has been achieved and in many ways surpassed, it is useful to think about how this research fits in to the wider physics community and where it could lead to.

We will begin by short term outcomes of this research. It is clear that cryogenic resonance Raman studies provides a plethora of information, if we were to continue on the assumption that Raman studies on these extreme materials are useful and relevant then the next obvious experiment would be spectroelectrochemical [108, 109, 110] gating of filled nanotubes. This may allow better insight into charge transfer effects between the nanowire and the host tube.

Another interesting development of this project is to investigate an array of other materials within the nanotube, not only to understand the physics of these 1D materials, but also for potential applications. For example, it has been previously shown some materials exhibit phase-change behaviour within carbon nanotubes [91], however in the reference mentioned this was done under TEM. No reports have demonstrated clear phase-change behaviour of extreme nanowires, which opens up a unique opportunity for demonstrating phase-change behaviour of a material within a nanotube. Raman could be a useful probe for this sort of experiment, as it is likely Raman is sensitive to amorphous and crystalline phases of a material. In addition it may be possible to laser anneal a PCM with the probe laser.

One key hurdle faced with most studies on filled carbon nanotubes and nanotubes in general is the polydispersity. In an ideal measurement scenario, inhomogeneous effects from tube-tube interactions could be significantly reduced with the ability to isolate and individualise filled nanotubes. This may be possible with density gradient ultracentrifucation. [97] Furthermore the ability to deposit a single tube on a TEM grid for HRTEM

characterisation and then to perform Raman studies on the same tube with a definite known internal crystal structure would reduce any uncertainty as to what is being measured in the Raman.

The previous short-term experiments have all assumed that temperature dependant Raman studies would the characterisation tool of use. Clearly there may be other experiments that might be easier to perform once the basic electronic structure of the filling material is understood. For example measured the heat capacity of the filling material using differential scanning calorimetry [215] could be a relatively simple experiment and provide information.

In terms of the medium to long term relevance of this research. Let us consider one obvious application of extreme nanowires; transistors, or at least some sort of interconnect. Fundamentally, studies on the physics and properties of extreme nanowire systems is important, especially as transistor size is fast approaching the fundamental limit of miniaturisation (e.g. extreme nanowire). This thesis has demonstrated the physics of materials is very different at the extreme limit, which is very likely to be an important consideration when transistor device size reaches this sort of size scale i.e the few atom scale. The experiments discussed in this thesis provide a rigorous study of certain filling materials, which could in principle be used to improve theoretical models of an array of extreme nanowire systems. As stated earlier phase-change materials (PCMS) have lots of applications in memory devices. Filled nanotubes could provide the smallest phase-change memory element meaning the highest storage density possible.

In general there are many potential interesting applications and useful physics out of filled nanotubes, which mainly depend on the type of filling material impregnated within the tube. In terms of semiconductor materials embedded within tubes, it is clear in the case of HgTe, and other associated filling materials (e.g PbI_2) that new vibrational modes can appear, and the electronic properties of the material can be significantly altered. This highlights the use of this kind of study on extreme nanowire systems. Most importantly, this study demonstrates whatever research or measurement is performed on extreme nanowires, it has to be rigorous enough to be certain of the results, as there are many variables that could alter the conclusions.

Fin

References

[1] J. H. Spencer, J. M. Nesbitt, H. Trewhitt, R. J. Kashtiban, G. Bell, V. G. Ivanov, E. Faulques, J. Sloan, and D. C. Smith, "Raman spectroscopy of optical transitions and vibrational energies of 1 nm hgte extreme nanowires within single walled carbon nanotubes," *ACS Nano*, vol. 8, no. 9, pp. 9044–9052, 2014. PMID: 25163005.

[2] V. N. Popov, "Carbon nanotubes: Properties and application," *Materials Science and Engineering R: Reports*, vol. 43, no. 2004, pp. 61–102, 2004.

[3] M. V. Kharlamova, "Electronic properties of pristine and modified single-walled carbon nanotubes," *Uspekhi Fizicheskih Nauk*, vol. 183, pp. 1145–1174, 2013.

[4] M. S. Dresselhaus, G. Dresselhaus, R. Saito, and A. Jorio, "Raman spectroscopy of carbon nanotubes," *Physics Reports*, vol. 409, pp. 47–99, Mar. 2005.

[5] R. Carter, J. Sloan, A. Kirkland, R. Meyer, P. Lindan, G. Lin, M. Green, A. Vlandas, J. Hutchison, and J. Harding, "Correlation of structural and electronic properties in a new low-dimensional form of mercury telluride," *Physical Review Letters*, vol. 96, May 2006.

[6] E. Zielony, E. Placzek-Popko, P. Kamyczek, A. Henrykowski, and G. Karczewski, "Raman spectroscopy of cdte/znte quantum dot structures," *Optica Applicata*, vol. 43, pp. 181–185, 2013.

[7] A. Werner, H. D. Hochheimer, K. Strössner, and A. Jayaraman, "High-pressure x-ray diffraction studies on hgte and hgs to 20 gpa," *Phys. Rev. B*, vol. 28, pp. 3330–3334, Sep 1983.

[8] D. C. Smith, J. H. Spencer, J. Sloan, L. P. McDonnell, H. Trewhitt, R. J. Kashtiban, and E. Faulques, "Resonance raman spectroscopy of extreme nanowires and other 1d systems," no. 110, pp. e53434–, 2016.

[9] V. A. Kosobukin, "Theory of exciton-polaritonic absorption in multiple quantum wells," *physica status solidi (b)*, vol. 208, no. 1, pp. 271–283, 1998.

[10] S. Rudin and T. L. Reinecke, "Temperature-dependent exciton linewidths in semiconductor quantum wells," *Phys. Rev. B*, vol. 41, pp. 3017–3027, Feb 1990.

[11] S. J. Tans, M. H. Devoret, H. Dai, A. Thess, R. E. Smalley, L. J. Geerligs, and C. Dekker, "Individual single-wall carbon nanotubes as quantum wires," *Nature*, vol. 386, pp. 474–477, Apr. 1997.

[12] M. A. Reed, J. N. Randall, R. J. Aggarwal, R. J. Matyi, T. M. Moore, and A. E. Wetsel, "Observation of discrete electronic states in a zero-dimensional semiconductor nanostructure," *Phys. Rev. Lett.*, vol. 60, pp. 535–537, Feb 1988.

[13] M. Dresselhaus, G. Dresselhaus, and R. Saito, "Physics of carbon nanotubes," *Carbon*, vol. 33, no. 95, pp. 883–891, 1995.

[14] C. D. Spataru, S. Ismail-Beigi, L. X. Benedict, and S. G. Louie, "Excitonic effects and optical spectra of single-walled carbon nanotubes," *Phys. Rev. Lett.*, vol. 92, p. 077402, Feb 2004.

[15] F. Wang, D. J. Cho, B. Kessler, J. Deslippe, P. J. Schuck, S. G. Louie, A. Zettl, T. F. Heinz, and Y. R. Shen, "Observation of excitons in one-dimensional metallic single-walled carbon nanotubes," *Phys. Rev. Lett.*, vol. 99, p. 227401, Nov 2007.

[16] R. E. Peierls, "Cohesive forces in metals," in *Quantum Theory of Solids*, Oxford: Oxford University Press, 2001.

[17] S.-i. Tomonaga, "Remarks on bloch's method of sound waves applied to many-fermion problems," *Progress of Theoretical Physics*, vol. 5, no. 4, pp. 544–569, 1950.

[18] J. M. Luttinger, "An exactly soluble model of a many-fermion system," *Journal of Mathematical Physics*, vol. 4, no. 9, pp. 1154–1162, 1963.

[19] J. M. Krans, J. M. van Ruitenbeek, V. V. Fisun, I. K. Yanson, and L. J. de Jongh, "The signature of conductance quantization in metallic point contacts," *Nature*, vol. 375, pp. 767–769, June 1995.

[20] L. Olesen, E. Laegsgaard, I. Stensgaard, F. Besenbacher, J. Schio/tz, P. Stoltze, K. W. Jacobsen, and J. K. No/rskov, "Quantized conductance in an atom-sized point contact," *Phys. Rev. Lett.*, vol. 72, pp. 2251–2254, Apr 1994.

[21] M. Monthioux, "Filling single-wall carbon nanotubes," *Carbon*, vol. 40, no. 10, pp. 1809 – 1823, 2002.

[22] E. Borowiak-Palen, a. Bachmatiuk, M. H. Rümmeli, T. Gemming, T. Pichler, and R. J. Kalenczuk, "Iron filled singlewalled carbon nanotubes - synthesis and characteristic properties," *Physica Status Solidi (B)*, vol. 243, pp. 3277–3280, 2006.

[23] C. Liang, G. Meng, and L. Zhang, "Carbon nanotubes filled partially or completely with nickel," *Journal of Crystal Growth*, vol. 218, pp. 136–139, 2000.

[24] M. Kharlamova and J. Niu, "Comparison of metallic silver and copper doping effects on single-walled carbon nanotubes," *Applied Physics A*, vol. 109, no. 1, pp. 25–29, 2012.

[25] M. V. Kharlamova and J. J. Niu, "New method of the directional modification of the electronic structure of single-walled carbon nanotubes by filling channels with metallic copper from a liquid phase," 2012.

[26] T. Fujimori, A. Morelos-Gómez, Z. Zhu, H. Muramatsu, R. Futamura, K. Urita, M. Terrones, T. Hayashi, M. Endo, S. Young Hong, and et al., "Conducting linear chains of sulphur inside carbon nanotubes," *Nat Comms*, vol. 4, Jul 2013.

[27] M. Sendova and E. Flahaut, "Comparative micro-Raman spectroscopy study of tellurium-filled double-walled carbon nanotubes," *Journal of Applied Physics*, vol. 103, no. 2008, p. 024311, 2008.

[28] M. Sendova, L. Datas, and E. Flahaut, "Micro-raman scattering of selenium-filled double-walled carbon nanotubes: Temperature study," *Journal of Applied Physics*, vol. 105, no. 9, pp. –, 2009.

[29] M. Chernysheva, E. Kiseleva, N. Verbitskii, a.a. Eliseev, a.V. Lukashin, Y. Tretyakov, S. Savilov, N. Kiselev, O. Zhigalina, a.S. Kumskov, a.V. Krestinin, and J. Hutchison, "The electronic properties of SWNTs intercalated by electron acceptors," *Physica E: Low-dimensional Systems and Nanostructures*, vol. 40, pp. 2283–2288, May 2008.

[30] R. Senga, H.-P. Komsa, Z. Liu, K. Hirose-Takai, A. V. Krasheninnikov, and K. Suenaga, "Atomic structure and dynamic behaviour of trulyăone-dimensional ionic chains inside carbonănanotubes," *Nat Mater*, vol. 13, pp. 1050–1054, Nov. 2014.

[31] F. Hennrich, R. Krupke, S. Lebedkin, K. Arnold, R. Fischer, D. E. Resasco, and M. M. Kappes, "Raman spectroscopy of individual single-walled carbon nanotubes from various sources.," *The journal of physical chemistry. B*, vol. 109, pp. 10567–10573, 2005.

[32] M. S. Dresselhaus, G. Dresselhaus, A. Jorio, A. G. Souza Filho, and R. Saito, "Raman spectroscopy on isolated single wall carbon nanotubes," *Carbon*, vol. 40, no. 12, pp. 2043–2061, 2002.

[33] S. Bose, S. Behera, S. Sarangi, and P. Entel, "Raman spectra of filled carbon nanotubes," *Physica B: Condensed Matter*, vol. 351, no. 1âĂŞ2, pp. 129 – 136, 2004.

[34] A. Eliseev, L. Yashina, N. Verbitskiy, M. Brzhezinskaya, M. Kharlamova, M. Chernysheva, a.V. Lukashin, N. Kiselev, A. Kumskov, B. Freitag, A. Generalov,

A. Vinogradov, Y. Zubavichus, E. Kleimenov, and M. Nachtegaal, "Interaction between single walled carbon nanotube and 1D crystal in CuX@SWCNT (X=Cl, Br, I) nanostructures," *Carbon*, vol. 50, pp. 4021–4039, Sept. 2012.

[35] A. Eliseev, L. Yashina, M. Brzhezinskaya, M. Chernysheva, M. Kharlamova, N. Verbitsky, A. Lukashin, N. Kiselev, A. Kumskov, R. Zakalyuhin, J. Hutchison, B. Freitag, and A. Vinogradov, "Structure and electronic properties of AgX (X=Cl, Br, I)-intercalated single-walled carbon nanotubes," *Carbon*, vol. 48, pp. 2708–2721, Aug. 2010.

[36] M. V. Kharlamova, "Raman Spectroscopy Study of the Doping Effect of the Encapsulated Iron, Cobalt, and Nickel Bromides on Single-Walled Carbon Nanotubes," *Journal of Spectroscopy*, vol. 2015, p. 8, 2015.

[37] M. V. Kharlamova, L. V. Yashina, a. a. Eliseev, a. a. Volykhov, V. S. Neudachina, M. M. Brzhezinskaya, T. S. Zyubina, a. V. Lukashin, and Y. D. Tretyakov, "Single-walled carbon nanotubes filled with nickel halogenides: Atomic structure and doping effect," *Physica Status Solidi (B)*, vol. 249, pp. 2328–2332, Dec. 2012.

[38] L.-J. Li, T.-W. Lin, J. Doig, I. Mortimer, J. Wiltshire, R. Taylor, J. Sloan, M. Green, and R. Nicholas, "Crystal-encapsulation-induced band-structure change in single-walled carbon nanotubes: Photoluminescence and raman spectra," *Phys. Rev. B*, vol. 74, Dec 2006.

[39] M. Sendova, E. Flahaut, and B. DeBono, "Raman spectroscopy of pbi2-filled double-walled carbon nanotubes," *Journal of Applied Physics*, vol. 98, no. 10, pp. 104304–104304–4, 2005.

[40] S. Iijima, "Helical microtubules of graphitic carbon," *Nature*, vol. 354, no. 6348, pp. 56–58, 1991.

[41] D. S. Bethune, R. D. Johnson, J. R. Salem, M. S. de Vries, and C. S. Yannoni, "Atoms in carbon cages: the structure and properties of endohedral fullerenes," *Nature*, vol. 366, no. 6451, pp. 123–128, 1993.

[42] S. Iijima and T. Ichihashi, "Single-shell carbon nanotubes of 1-nm diameter," *Nature*, vol. 363, no. 6430, pp. 603–605, 1993.

[43] H. Golnabi, "Carbon nanotube research developments in terms of published papers and patents, synthesis and production," *Scientia Iranica*, vol. 19, no. 6, pp. 2012 – 2022, 2012.

[44] P. Lambin, "Electronic structure of carbon nanotubes," *Comptes Rendus Physique*, vol. 4, no. 9, pp. 1009 – 1019, 2003. Dossier: Carbon nanotubes: state of the art and applications.

[45] J. C. Charlier, X. Blase, and S. Roche, "Electronic and transport properties of nanotubes," *Reviews of Modern Physics*, vol. 79, no. June, pp. 677–732, 2007.

[46] S. Reich, C. Thomsen, and P. Ordejón, "Electronic band structure of isolated and bundled carbon nanotubes," *Physical Review B*, vol. 65, no. 15, p. 155411, 2002.

[47] R. Saito, M. Fujita, G. Dresselhaus, and M. S. Dresselhaus, "Electronic structure of chiral graphene tubules," *Applied Physics Letters*, vol. 60, no. 1992, pp. 2204–2206, 1992.

[48] S. Xie, W. Li, Z. Pan, B. Chang, and L. Sun, "Mechanical and physical properties on carbon nanotube," *Journal of Physics and Chemistry of Solids*, vol. 61, no. 7, pp. 1153 – 1158, 2000.

[49] R. S. Ruoff and D. C. Lorents, "Mechanical and thermal properties of carbon nanotubes," *Carbon*, vol. 33, no. 7, pp. 925 – 930, 1995. Nanotubes.

[50] S. Tans, A. Verschueren, and C. Dekker, "Room-temperature transistor based on a single carbon nanotube," *Nature*, vol. 672, no. 1989, pp. 669–672, 1998.

[51] R. Martel, T. Schmidt, H. R. Shea, T. Hertel, and P. Avouris, "Single- and multi-wall carbon nanotube field-effect transistors," *Applied Physics Letters*, vol. 73, no. 17, pp. 2447–2449, 1998.

[52] A. D. Franklin, M. Luisier, S. J. Han, G. Tulevski, C. M. Breslin, L. Gignac, M. S. Lundstrom, and W. Haensch, "Sub-10 nm Carbon Nanotube Transistor," *Nano Letters*, vol. 12, no. 2, pp. 758–762, 2012.

[53] J. Cao, Q. Wang, and H. Dai, "Electron transport in very clean, as-grown suspended carbon nanotubes," *Nature Materials*, vol. 4, no. 10, pp. 745–749, 2005.

[54] A. Javey, J. Guo, Q. Wang, M. Lundstrom, and H. Dai, "Ballistic carbon nanotube field-effect transistors.," *Nature*, vol. 424, no. 6949, pp. 654–657, 2003.

[55] A. K. Hüttel, G. A. Steele, B. Witkamp, M. Poot, L. P. Kouwenhoven, and H. S. J. van der Zant, "Carbon nanotubes as ultrahigh quality factor mechanical resonators," *Nano Letters*, vol. 9, no. 7, pp. 2547–2552, 2009. PMID: 19492820.

[56] M. Nishio, S. Sawaya, S. Akita, and Y. Nakayama, "Carbon nanotube oscillators toward zeptogram detection," *Applied Physics Letters*, vol. 86, no. 13, 2005.

[57] A. a. Bhirde, V. Patel, J. Gavard, G. Zhang, A. a. Sousa, A. Masedunskas, R. D. Leapman, R. Weigert, J. S. Gutkind, and J. F. Rusling, "Targeted killing of cancer cells in vivo and in vitro with EGF-directed carbon nanotube-based drug delivery.," *ACS nano*, vol. 3, no. 2, pp. 307–16, 2009.

[58] T. a. Hilder and J. M. Hill, "Modeling the loading and unloading of drugs into nanotubes," *Small*, vol. 5, no. 3, pp. 300–308, 2009.

[59] M. S. Dresselhaus, G. Dresselhaus, and M. Hofmann, "The big picture of Raman scattering in carbon nanotubes," *Vibrational Spectroscopy*, vol. 45, pp. 71–81, Nov. 2007.

[60] H. Kataura, Y. Kumazawa, Y. Maniwa, I. Umezu, S. Suzuki, Y. Ohtsuka, and Y. Achiba, "Optical properties of single-wall carbon nanotubes," *Synthetic Metals*, vol. 103, pp. 2555–2558, June 1999.

[61] M. Bockrath, D. H. Cobden, J. Lu, A. G. Rinzler, R. E. Smalley, L. Balents, and P. L. McEuen, "Luttinger-liquid behaviour in carbon nanotubes," *Nature*, vol. 397, pp. 598–601, feb 1999.

[62] C. T. White and T. N. Todorov, "Carbon nanotubes as long ballistic conductors," *Nature*, vol. 393, pp. 240–242, May 1998.

[63] J. Sloan, J. Hammer, M. Zwiefka-Sibley, M. L. H. Green, and J. Sloan, "The opening and filling of single walled carbon nanotubes (SWTs)," *Chemical Communications*, vol. 1, pp. 347–348, 1998.

[64] B. Smith, C. J. Tabin, M. Monthioux, and D. Luzzi, "Encapsulated C60 in carbon nanotubes," *Nature*, vol. 396, no. November, pp. 323–324, 1998.

[65] R. Hatakeyama and Y. F. Li, "Synthesis and electronic-property control of Cs-encapsulated single- and double-walled carbon nanotubes by plasma ion irradiation," *Journal of Applied Physics*, vol. 102, no. 2007, 2007.

[66] L. Guan, K. Suenaga, Z. Shi, Z. Gu, and S. Iijima, "Polymorphic structures of iodine and their phase transition in confined nanospace," *Nano Letters*, vol. 7, pp. 1532–1535, 2007.

[67] K. R. Kissell, K. B. Hartman, P. a. W. Van der Heide, and L. J. Wilson, "Preparation of I2@SWNTs: synthesis and spectroscopic characterization of I2-loaded SWNTs.," *The journal of physical chemistry. B*, vol. 110, pp. 17425–17429, 2006.

[68] T. Pichler, C. Kramberger, P. Ayala, H. Shiozawa, M. Knupfer, M. H. Rümmeli, D. Batchelor, R. Kitaura, N. Imazu, K. Kobayashi, and H. Shinohara, "Bonding environment and electronic structure of Gd metallofullerene and Gd nanowire filled single-wall carbon nanotubes," *Physica Status Solidi (B) Basic Research*, vol. 245, pp. 2038–2041, 2008.

[69] T. Okazaki, K. Suenaga, K. Hirahara, S. Bandow, S. Iijima, and H. Shinohara, "Electronic and geometric structures of metallofullerene peapods," *Physica B: Condensed Matter*, vol. 323, pp. 97–99, 2002.

[70] B. W. Smith, D. E. Luzzi, and Y. Achiba, "Tumbling atoms and evidence for charge transfer in La2@C80@SWNT," *Chemical Physics Letters*, vol. 331, no. December, pp. 137–142, 2000.

[71] J. Sloan, D. M. Wright, S. Bailey, G. Brown, A. P. E. York, K. S. Coleman, M. L. H. Green, J. Sloan, D. M. Wright, J. L. Hutchison, and H.-G. Woo, "Capillarity and silver nanowire formation observed in single walled carbon nanotubes," *Chemical Communications*, no. 8, pp. 699–700, 1999.

[72] R. Cisneros, C. Ramírez, and C. Wang, "Ellipsometry and ab initio approaches to the refractive index of porous silicon," *Journal of Physics: Condensed Matter*, vol. 19, p. 395010, Oct. 2007.

[73] R. Zakalyukin, B. Mavrin, L. DemâĂŹyanets, and N. Kiselev, "Synthesis and characterization of single-walled carbon nanotubes filled with the superionic material snf2," *Carbon*, vol. 46, no. 12, pp. 1574 – 1578, 2008.

[74] A. A. Eliseev, N. I. Verbitskiy, A. A. Volykhov, A. V. Fedorov, O. Y. Vilkov, I. I. Verbitskiy, M. M. Brzhezinskaya, N. A. Kiselev, and L. V. Yashina, "The impact of dimensionality and stoichiometry of cubr on its coupling to sp2-carbon," *Carbon*, pp. –, 2015.

[75] L. V. Yashina, A. A. Eliseev, M. V. Kharlamova, A. A. Volykhov, A. V. Egorov, S. V. Savilov, A. V. Lukashin, R. PÃijttner, and A. I. Belogorokhov, "Growth and characterization of one-dimensional snte crystals within the single-walled carbon nanotube channels," *The Journal of Physical Chemistry C*, vol. 115, no. 9, pp. 3578–3586, 2011.

[76] L.-J. Li, T.-W. Lin, J. Doig, I. B. Mortimer, J. G. Wiltshire, R. A. Taylor, J. Sloan, M. L. H. Green, and R. J. Nicholas, "Crystal-encapsulation-induced band-structure change in single-walled carbon nanotubes: Photoluminescence and raman spectra," *Phys. Rev. B*, vol. 74, p. 245418, Dec 2006.

[77] P. Corio, A. Santos, P. Santos, M. Temperini, V. Brar, M. Pimenta, and M. Dresselhaus, "Characterization of single wall carbon nanotubes filled with silver and with chromium compounds," *Chemical Physics Letters*, vol. 383, no. 5Ű6, pp. 475 – 480, 2004.

[78] M. Chernysheva, A. Eliseev, A. Lukashin, Y. Tretyakov, S. Savilov, N. Kiselev, O. Zhigalina, A. Kumskov, A. Krestinin, and J. Hutchison, "Filling of single-walled carbon nanotubes by cui nanocrystals via capillary technique," *Physica E: Low-dimensional Systems and Nanostructures*, vol. 37, no. 1Ű2, pp. 62 – 65, 2007. Proceedings of the E-MRS 2006 Symposium E: Science and Technology of Nanotubes and Nanowires.

[79] M. Kharlamova, A. Eliseev, L. Yashina, D. Petukhov, C.-P. Liu, C.-Y. Wang, D. Semenenko, and A. Belogorokhov, "Study of the electronic structure of single-walled carbon nanotubes filled with cobalt bromide," *JETP Letters*, vol. 91, no. 4, pp. 196–200, 2010.

[80] M. V. Kharlamova, L. V. Yashina, and A. V. Lukashin, "Charge transfer in single-walled carbon nanotubes filled with cadmium halogenides," *Journal of Materials Science*, vol. 48, no. 24, pp. 8412–8419, 2013. Times Cited: 0.

[81] M. V. Kharlamova, L. V. Yashina, A. A. Volykhov, J. J. Niu, V. S. Neudachina, M. M. Brzhezinskaya, T. S. Zyubina, A. I. Belogorokhov, and A. A. Eliseev, "Acceptor doping of single-walled carbon nanotubes by encapsulation of zinc halogenides," *European Physical Journal B*, vol. 85, no. 1, 2012. Times Cited: 7.

[82] A. Ilie, J. S. Bendall, D. Roy, E. Philp, and M. L. H. Green, "Effects of ki encapsulation in single-walled carbon nanotubes by raman and optical absorption spectroscopy," *The Journal of Physical Chemistry B*, vol. 110, no. 28, pp. 13848–13857, 2006.

[83] X. Liu, I. Marangon, G. Melinte, C. Wilhelm, C. Ménard-Moyon, B. P. Pichon, O. Ersen, K. Aubertin, W. Baaziz, C. Pham-Huu, S. Bégin-Colin, A. Bianco, F. Gazeau, and D. Bégin, "Design of Covalently Functionalized Carbon Nanotubes Filled with Metal Oxide Nanoparticles for Imaging, Therapy, and Magnetic Manipulation," *Acs Nano*, vol. 8, no. 11, pp. 11290–11304, 2014.

[84] T. Shimada, Y. Ohno, T. Okazaki, T. Sugai, K. Suenaga, S. Kishimoto, T. Mizutani, T. Inoue, R. Taniguchi, N. Fukui, H. Okubo, and H. Shinohara, "Transport properties of c78, {C90} and dy@c82 fullerenes-nanopeapods by field effect transistors," *Physica E: Low-dimensional Systems and Nanostructures*, vol. 21, no. 2âĂŞ4, pp. 1089 – 1092, 2004. Proceedings of the Eleventh International Conference on Modulated Semiconductor Structures.

[85] T. Okazaki, T. Shimada, K. Suenaga, Y. Ohno, T. Mizutani, J. Lee, Y. Kuk, and H. Shinohara, "Electronic properties of gd@c82 metallofullerene peapods: (gd@c82)n@swnts," *Applied Physics A*, vol. 76, no. 4, pp. 475–478.

[86] P. Chiu, G. Gu, G. Kim, G. Philipp, S. Roth, S. Yang, and S. Yang, "Temperature-induced change from p to n conduction in metallofullerene nanotube peapods," *Applied Physics Letters*, vol. 79, pp. 3845–3847, 12 2001.

[87] C.-K. Yang, J. Zhao, and J. P. Lu, "Magnetism of transition-metal/carbon-nanotube hybrid structures," *Phys. Rev. Lett.*, vol. 90, p. 257203, Jun 2003.

[88] A. M. Popov, Y. E. Lozovik, S. Fiorito, and L. Yahia, "Biocompatibility and applications of carbon nanotubes in medical nanorobots," *International Journal of Nanomedicine*, vol. 2, pp. 361–372, Sept. 2007.

[89] D. B. W. C. B. Carter, *Transmission Electron Microscopy*. Springer US, 1996.

[90] J. Sloan, J. Hammer, M. Zwiefka-Sibley, and M. L. H. Green, "The opening and filling of single walled carbon nanotubes (swts)," *Chemical Communications*, no. 3, pp. 347–348, 1998.

[91] C. E. Giusca, V. Stolojan, J. Sloan, F. BÃűrrnert, H. Shiozawa, K. Sader, M. H. RÃijmmeli, B. BÃijchner, and S. R. P. Silva, "Confined crystals of the smallest phase-change material," *Nano Letters*, vol. 13, no. 9, pp. 4020–4027, 2013.

[92] M. S. Strano, "Electronic Structure Control of Single-Walled Carbon Nanotube Functionalization," *Science (New York, NY)*, vol. 301, no. September, pp. 1519–1522, 2003.

[93] a. R. T. S. Attal and O. Regev, "Determination of the concentration of single-walled carbon nanotubes in aqueous dispersions using uv-visible absorption spectroscopy," *Analytical Chemistry*, vol. 78, no. 23, pp. 8098–8104, 2006. PMID: 17134145.

[94] S. Kazaoui, N. Minami, H. Kataura, and Y. Achiba, "Absorption spectroscopy of single-wall carbon nanotubes: effects of chemical and electrochemical doping," *Synthetic Metals*, vol. 121, no. 1âĂŞ3, pp. 1201 – 1202, 2001. Proceedings of the International Conference on the Science and Technology of Synthetic Metals.

[95] T. Takenobu, T. Takano, M. Shiraishi, Y. Murakami, M. Ata, H. Kataura, Y. Achiba, and Y. Iwasa, "Stable and controlled amphoteric doping by encapsulation of organic molecules inside carbon nanotubes," *Nat Mater*, vol. 2, pp. 683–688, Oct. 2003.

[96] L.-J. Li, A. N. Khlobystov, J. G. Wiltshire, G. A. D. Briggs, and R. J. Nicholas, "Diameter-selective encapsulation of metallocenes in single-walled carbon nanotubes," *Nat Mater*, vol. 4, pp. 481–485, June 2005.

[97] P. Zhao, E. Einarsson, G. Lagoudas, J. Shiomi, S. Chiashi, and S. Maruyama, "Tunable separation of single-walled carbon nanotubes by dual-surfactant density gradient ultracentrifugation," *Nano Research*, vol. 4, no. 7, pp. 623–634, 2011.

[98] R. B. Weisman, , and S. M. Bachilo, "Dependence of optical transition energies on structure for single-walled carbon nanotubes in aqueous suspension: An empirical kataura plot," *Nano Letters*, vol. 3, no. 9, pp. 1235–1238, 2003.

[99] M. J. O'Connell, "Band gap fluorescence from individual single-walled carbon nanotubes," *Science*, vol. 297, pp. 593–596, Jul 2002.

[100] L.-J. Li, R. J. Nicholas, C.-Y. Chen, R. C. Darton, and S. C. Baker, "Comparative study of photoluminescence of single-walled carbon nanotubes wrapped with sodium dodecyl sulfate, surfactin and polyvinylpyrrolidone," *Nanotechnology*, vol. 16, no. 5, p. S202, 2005.

[101] M. V. Kharlamova, "Comparison of influence of incorporated 3d-, 4d- and 4f-metal chlorides on electronic properties of single-walled carbon nanotubes," *Applied Physics A*, vol. 111, no. 3, pp. 725–731, 2013.

[102] P. Corio, A. P. Santos, P. S. Santos, M. L. A. Temperini, V. W. Brar, M. A. Pimenta, and M. S. Dresselhaus, "Characterization of single wall carbon nanotubes filled with silver and with chromium compounds," *Chemical Physics Letters*, vol. 383, pp. 475–480, Jan. 2004.

[103] A. S. Kumskov, V. G. Zhigalina, A. L. Chuvilin, N. I. Verbitskiy, A. G. Ryabenko, D. D. Zaytsev, A. A. Eliseev, and N. A. Kiselev, "The structure of 1d and 3d cui nanocrystals grown within 1.5-2.5 nm single wall carbon nanotubes obtained by catalyzed chemical vapor deposition," *Carbon*, vol. 50, no. 12, pp. 4696–4704, 2012. Times Cited: 1.

[104] M. V. Kharlamova, M. M. Brzhezinskay, A. S. Vinogradov, I. P. Suzdalev, Y. V. Maksimov, V. K. Imshennik, S. V. Novichikhin, A. V. Krestinin, L. V. Yashina, A. V. Lukashin, Y. D. Tret'yakov, and A. A. Eliseev, "The formation and properties of one-dimensional fehal2 (hal = cl, br, i) nanocrystals in channels of single-walled carbon nanotubes," *Nanotechnologies in Russia*, vol. 4, no. 9, pp. 634–646, 2009.

[105] M. V. Kharlamova, A. A. Eliseev, L. V. Yashina, A. V. Lukashin, and Y. D. Tretyakov, "Synthesis of nanocomposites on basis of single-walled carbon nanotubes intercalated by manganese halogenides," *Journal of Physics: Conference Series*, vol. 345, no. 1, p. 012034, 2012.

[106] M. V. Kharlamova, A. A. Eliseev, L. V. Yashina, D. I. Petukhov, C.-P. Liu, C.-Y. Wang, D. A. Semenenko, and A. I. Belogorokhov, "Study of the electronic structure of single-walled carbon nanotubes filled with cobalt bromide," *JETP Letters*, vol. 91, no. 4, pp. 196–200, 2010.

[107] M. Kalbac, H. Farhat, L. Kavan, J. Kong, K.-i. Sasaki, R. Saito, and M. S. Dresselhaus, "Electrochemical charging of individual single-walled carbon nanotubes," *ACS Nano*, vol. 3, no. 8, pp. 2320–2328, 2009. PMID: 19645423.

[108] L. Kavan, M. KalbÃącĬŇ, M. ZukalovÃą, and L. Dunsch, "Electrochemical doping of chirality-resolved carbon nanotubes," *The Journal of Physical Chemistry B*, vol. 109, no. 42, pp. 19613–19619, 2005.

[109] M. Kalbac, L. Kavan, and L. Dunsch, "Changes in the electronic states of single-walled carbon nanotubes as followed by a raman spectroelectrochemical analysis of the radial breathing mode," *The Journal of Physical Chemistry C*, vol. 112, no. 43, pp. 16759–16763, 2008.

[110] S. Kazaoui, N. Minami, N. Matsuda, H. Kataura, and Y. Achiba, "Electrochemical tuning of electronic states in single-wall carbon nanotubes studied by in situ absorption spectroscopy and ac resistance," *Applied Physics Letters*, vol. 78, no. 22, pp. 3433–3435, 2001.

[111] GaufresE., T. Y.-Wa, LapointeF., CabanaJ., NadonM.-A., CottenyeN., RaymondF., SzkopekT., and MartelR., "Giant raman scattering from j-aggregated dyes inside carbon nanotubes for multispectral imaging," *Nat Photon*, vol. 8, pp. 72–78, Jan. 2014.

[112] G. Li, C. Fu, M. B. Oviedo, M. Chen, X. Tian, E. Bekyarova, M. E. Itkis, B. M. Wong, J. Guo, and R. C. Haddon, "Giant raman response to the encapsulation of sulfur in narrow diameter single-walled carbon nanotubes," *Journal of the American Chemical Society*, vol. 138, no. 1, pp. 40–43, 2016. PMID: 26675065.

[113] K. Yanagi, Y. Miyata, and H. Kataura, "Highly stabilized b-carotene in carbon nanotubes," *Advanced Materials*, vol. 18, no. 4, pp. 437–441, 2006.

[114] M. Dresselhaus, G. Dresselhaus, R. Saito, and A. Jorio, "Raman spectroscopy of carbon nanotubes," *Physics Reports*, vol. 409, pp. 47–99, Mar 2005.

[115] H. F. Bettinger, "Carbon nanotubesŮbasic concepts and physical properties. by s. reich, c. thomsen, j. maultzsch.," *ChemPhysChem*, vol. 5, no. 12, pp. 1914–1915, 2004.

[116] J. Sloan and M. Monthioux, *Filled Carbon Nanotubes: (X@CNTs)*, pp. 225–271. John Wiley & Sons, Ltd, 2011.

[117] T. Hertel, R. E. Walkup, and P. Avouris, "Deformation of carbon nanotubes by surface van der Waals forces," *Phys. Rev. B*, vol. 58, no. November, pp. 13870–13873, 1998.

[118] R. Saito, G. Dresselhaus, and M. Dresselhaus, *Physical Properties of Carbon Nanotubes*. World Scientific Publishing Company, July 1998.

[119] a. Jorio, R. Saito, J. H. Hafner, C. M. Lieber, M. Hunter, T. McClure, G. Dresselhaus, and M. S. Dresselhaus, "Structural (n, m) determination of isolated single-wall carbon nanotubes by resonant Raman scattering," *Physical Review Letters*, vol. 86, pp. 1118–1121, 2001.

[120] A. K. Geim and K. S. Novoselov, "The rise of graphene," *Nature Materials*, vol. 6, pp. 183–191, 2007.

[121] L. Malard, M. Pimenta, G. Dresselhaus, and M. Dresselhaus, "Raman spectroscopy in graphene," *Physics Reports*, vol. 473, no. 5âĂŞ6, pp. 51 – 87, 2009.

[122] N. Ashcroft and N. Mermin, *Solid State Physics*. HRW international editions, Holt, Rinehart and Winston, 1976.

[123] G. G. Samsonidze, A. R. Saito, D. A. Jorio, E. M. A. Pimenta, E. A. G. Souza Filho, F. A. Gruneis, A.neis, D. G. Dresselhaus, and M. S. Dresselhausa, "The concept of cutting lines in carbon nanotube science," *Journal of Nanoscience and Nanotechnology*, vol. 3, pp. 431–458, Dec 2003.

[124] G. G. Samsonidze, R. Saito, N. Kobayashi, a. GruÌĹneis, J. Jiang, a. Jorio, S. G. Chou, G. Dresselhaus, and M. S. Dresselhaus, "Family behavior of the optical transition energies in single-wall carbon nanotubes of smaller diameters," *Applied Physics Letters*, vol. 85, no. 23, p. 5703, 2004.

[125] L. Van Hove, "The occurrence of singularities in the elastic frequency distribution of a crystal," *Phys. Rev.*, vol. 89, pp. 1189–1193, Mar 1953.

[126] C. Fantini, a. Jorio, M. Souza, M. S. Strano, M. S. Dresselhaus, and M. a. Pimenta, "Optical transition energies for carbon nanotubes from resonant raman spectroscopy: Environment and temperature effects," *Physical Review Letters*, vol. 93, no. October, pp. 1–4, 2004.

[127] R. Saito, A. Gruneis, G. G. Samsonidze, V. W. Brar, G. Dresselhaus, M. S. Dresselhaus, A. Jorio, L. G. Cancado, C. Fantini, M. A. Pimenta, and A. G. Souza, "Double resonance raman spectroscopy of single-wall carbon nanotubes," *New Journal of Physics*, vol. 5, 2003.

[128] a. Jorio, a. Souza Filho, G. Dresselhaus, M. Dresselhaus, R. Saito, J. Hafner, C. Lieber, F. Matinaga, M. Dantas, and M. Pimenta, "Joint density of electronic states for one isolated single-wall carbon nanotube studied by resonant Raman scattering," *Physical Review B*, vol. 63, p. 245416, jun 2001.

[129] J.-C. Blancon, M. Paillet, H. N. Tran, X. T. Than, S. A. Guebrou, A. Ayari, A. San Miguel, N.-M. Phan, A.-A. Zahab, J.-L. Sauvajol, N. Del Fatti, and F. Vallée, "Direct measurement of the absolute absorption spectrum of individual semiconducting single-wall carbon nanotubes.," *Nature communications*, vol. 4, p. 2542, 2013.

[130] R. Saito, G. Dresselhaus, and M. S. Dresselhaus, "Trigonal warping effect of carbon nanotubes," *Phys. Rev. B*, vol. 61, pp. 2981–2990, Jan 2000.

[131] V. Zeghbroeck, *Principles of Semiconductor Devices and Heterojunctions*. Prentice Hall PTR, 2007.

[132] M. S. Dresselhaus and P. C. Eklund, "Phonons in carbon nanotubes," *Advances in Physics*, vol. 49, no. 6, pp. 705–814, 2000.

[133] G. Srivastava, *The Physics of Phonons*. Taylor & Francis, 1990.

[134] R. Sharma, K. S. Sharma, and L. Dass, "Role of phonons in superconductivity," *Czechoslovak Journal of Physics B*, vol. 39, no. 5, pp. 537–548, 1989.

[135] X.-L. Zhang and W.-M. Liu, "Electron-phonon coupling and its implication for the superconducting topological insulators," *Scientific Reports*, vol. 5, pp. 8964–, Mar. 2015.

[136] H. P. Myers, *Introductory Solid State Physics*. Taylor & Francis, 1990.

[137] M. Cardona and G. Guntherodt, *Light Scattering in Solids VIII*. Springer Berlin Heidelberg, 2000.

[138] M. Brewster, O. Schimek, S. Reich, and S. Gradecak, "Exciton-phonon coupling in individual gaas nanowires studied using resonant raman spectroscopy," *Physical Review B*, vol. 80, no. 20, 2009.

[139] M. S. Dresselhaus, G. Dresselhaus, R. Saito, and A. Jorio, "Exciton photophysics of carbon nanotubes," *Annual Review of Physical Chemistry*, vol. 58, no. 1, pp. 719–747, 2007. PMID: 17201684.

[140] J.-Y. Park, S. Rosenblatt, Y. Yaish, V. Sazonova, H. ÃIJstÃijnel, S. Braig, T. A. Arias, P. W. Brouwer, , and P. L. McEuen, "Electron-phonon scattering in metallic single-walled carbon nanotubes," *Nano Letters*, vol. 4, no. 3, pp. 517–520, 2004.

[141] F. Wang, G. Dukovic, L. E. Brus, and T. F. Heinz, "The optical resonances in carbon nanotubes arise from excitons," *Science*, vol. 308, no. 5723, pp. 838–841, 2005.

[142] I. B. Mortimer and R. J. Nicholas, "Role of bright and dark excitons in the temperature-dependent photoluminescence of carbon nanotubes," *Phys. Rev. Lett.*, vol. 98, p. 027404, Jan 2007.

[143] D. Gardiner, P. Graves, and H. Bowley, *Practical Raman spectroscopy*. Springer, 1989.

[144] A. Kudelski, "Analytical applications of raman spectroscopy," *Talanta*, vol. 76, no. 1, pp. 1 – 8, 2008.

[145] D. A. Long, "Introductory raman spectroscopy. john r. ferraro, kazuo nakamoto and chris w. brown. academic press, amsterdam, second edition, 2003. xiii + 434," *Journal of Raman Spectroscopy*, vol. 36, no. 10, pp. 1012–1012, 2005.

[146] E. Smith and G. Dent, *Introduction, Basic Theory and Principles*, pp. 1–21. John Wiley & Sons, Ltd, 2005.

[147] A. Yariv, "The application of time evolution operators and feynman diagrams to nonlinear optics," *IEEE Journal of Quantum Electronics*, vol. 13, no. December, 1977.

[148] E. Cazzanelli, M. Castriota, L. Caputi, a. Cupolillo, C. Giallombardo, and L. Papagno, "High-temperature evolution of linear carbon chains inside multiwalled nanotubes," *Physical Review B*, vol. 75, p. 121405, mar 2007.

[149] S. Chiashi, Y. Murakami, Y. Miyauchi, and S. Maruyama, "Temperature dependence of raman scattering from single-walled carbon nanotubes: Undefined radial breathing mode peaks at high temperatures," *Japanese Journal of Applied Physics*, vol. 47, no. 4, pp. 2010–2015, 2008.

[150] R. M. Martin and L. M. Falicov, "Resonant Raman Scattering," in *Light Scattering in Solids SE - 3* (M. Cardona, ed.), vol. 8 of *Topics in Applied Physics*, pp. 79–145, Springer Berlin Heidelberg, 1975.

[151] A. C. Ferrari, "Raman spectroscopy of graphene and graphite: Disorder, electron-phonon coupling, doping and nonadiabatic effects," *Solid State Communications*, vol. 143, no. 1-2, pp. 47–57, 2007. Times Cited: 831.

[152] A. Jorio, C. Fantini, M. S. S. Dantas, M. A. Pimenta, A. G. Souza Filho, G. G. Samsonidze, V. W. Brar, G. Dresselhaus, M. S. Dresselhaus, A. K. Swan, M. S. Ünlü, B. B. Goldberg, and R. Saito, "Linewidth of the raman features of individual single-wall carbon nanotubes," *Phys. Rev. B*, vol. 66, p. 115411, Sep 2002.

[153] L. Cançado, M. Pimenta, R. Saito, a. Jorio, L. Ladeira, a. Grueneis, a. Souza-Filho, G. Dresselhaus, and M. Dresselhaus, "Stokes and anti-Stokes double resonance Raman scattering in two-dimensional graphite," *Physical Review B*, vol. 66, pp. 1–5, 2002.

[154] F. Tuinstra and J. L. Koenig, "Raman Spectrum of Graphite," *The Journal of Chemical Physics*, vol. 53, no. 3, p. 1126, 1970.

[155] M. Matthews, M. Pimenta, G. Dresselhaus, M. Dresselhaus, and M. Endo, "Origin of dispersive effects of the Raman D band in carbon materials," *Physical Review B*, vol. 59, no. 10, pp. R6585–R6588, 1999.

[156] G. Brown, S. Bailey, M. Novotny, R. Carter, E. Flahaut, K. Coleman, J. Hutchison, M. Green, and J. Sloan, "High yield incorporation and washing properties of halides incorporated into single walled carbon nanotubes," *Applied Physics A*, vol. 76, no. 4, pp. 457–462, 2003.

[157] A. Krestinin, N. Kiselev, A. Raevskii, D. Ryabenko, A.G. andZakharov, and G. Zvereva, "Perspectives of single-wall carbon nano-tube production in the arc discharge process," *Eurasian Chemico-Technological Journal*, vol. 1, pp. 7–18, 2003.

[158] S. Friedrichs, J. Sloan, M. L. H. Green, J. L. Hutchison, R. R. Meyer, and A. I. Kirkland, "Simultaneous determination of inclusion crystallography and nanotube conformation for a sb_2o_3/single − walled nanotube composite," *Phys. Rev. B*, vol. 64, p. 045406, Jun 2001.

[159] R. Carter, J. Sloan, A. Kirkland, R. Meyer, P. Lindan, G. Lin, M. Green, A. Vlandas, J. Hutchison, and J. Harding, "Correlation of structural and electronic properties in a new low-dimensional form of mercury telluride," *Physical Review Letters*, vol. 96, May 2006.

[160] M. Wollenhaupt, A. Assion, and T. Baumert, "Short and ultrashort laser pulses," in *Springer Handbook of Lasers and Optics* (F. TrÃď ger, ed.), pp. 1047–1094, Springer Berlin Heidelberg, 2012.

[161] O. Svelto, *Principles of Lasers*. Springer US, 2010.

[162] A. M. Rao, E. Richter, S. Bandow, B. Chase, P. C. Eklund, K. A. Williams, S. Fang, K. R. Subbaswamy, M. Menon, A. Thess, R. E. Smalley, G. Dresselhaus, and M. S. Dresselhaus, "Diameter-selective raman scattering from vibrational modes in carbon nanotubes," *Science*, vol. 275, no. 5297, pp. 187–191, 1997.

[163] Q. Cheng, S. Debnath, E. Gregan, and H. J. Byrne, "Vibrational mode assignments for bundled single-wall carbon nanotubes using raman spectroscopy at different excitation energies," *Applied Physics A*, vol. 102, pp. 309–317, Feb 2011.

[164] J. H. Parker, D. W. Feldman, and M. Ashkin, "Raman scattering by silicon and germanium," *Phys. Rev.*, vol. 155, pp. 712–714, Mar 1967.

[165] H. G. M. Edwards, *Modern Raman Spectroscopy - A Practical Approach*, vol. 36. 2005.

[166] A. J. Shields, M. Cardona, R. Nötzel, and K. Ploog, "Influence of the exciton lifetime on resonant Raman scattering in quantum wells," *Physical Review B*, vol. 46, no. October, pp. 10490–10493, 1992.

[167] J. Sloan, A. I. Kirkland, J. L. Hutchison, and M. L. H. Green, "Integral atomic layer architectures of 1d crystals inserted into single walled carbon nanotubes," *Chemical Communications*, no. 13, pp. 1319–1332, 2002.

[168] J. Sloan, S. J. Grosvenor, S. Friedrichs, A. I. Kirkland, J. L. Hutchison, and M. L. H. Green, "A one-dimensional bai2 chain with five- and six-coordination, formed within a single-walled carbon nanotube," *Angewandte Chemie-International Edition*, vol. 41, no. 7, pp. 1156–+, 2002. Times Cited: 42.

[169] C. Liu, J. Wang, and B. Li, "Preparation and characterization of ordered mesoporous silica membrane," *Journal of Non-Crystalline Solids*, vol. 351, pp. 409–412, Mar. 2005.

[170] M. S. Strano, S. K. Doorn, E. H. Haroz, C. Kittrell, R. H. Hauge, and R. E. Smalley, "Assignment of (n, m) Raman and optical features of metallic single-walled carbon nanotubes," *Nano Letters*, vol. 3, pp. 1091–1096, 2003.

[171] P. T. Araujo, P. B. C. Pesce, M. S. Dresselhaus, K. Sato, R. Saito, and A. Jorio, "Resonance raman spectroscopy of the radial breathing modes in carbon nanotubes," *Physica E-Low-Dimensional Systems & Nanostructures*, vol. 42, no. 5, pp. 1251–1261, 2010. Times Cited: 32.

[172] S. W. Liu, J. J. Zhu, Y. Mastai, I. Felner, and A. Gedanken, "Preparation and characteristics of carbon nanotubes filled with cobalt," *Chemistry of Materials*, vol. 12, no. 8, pp. 2205–2211, 2000.

[173] A. Ingale, M. L. Bansal, and A. P. Roy, "Resonance raman-scattering in hgte - to-phonon and forbidden-lo-phonon cross-section near the e1 gap," *Physical Review B*, vol. 40, no. 18, pp. 12353–12358, 1989.

[174] M. Bansal and A. Ingale, "Resonance raman scattering in mercury telluride," *Journal of Chemical Sciences*, vol. 102, no. 5, pp. 643–652, 1990.

[175] M. Rosch, R. Atzmuller, G. Schaack, and C. Becker, "Resonant Raman scattering in a zero-gap semiconductor: Interference effects and deformation potentials at the E1 and E1+ Delta 1 gaps of HgTe.," *Physical review. B, Condensed matter*, vol. 49, pp. 13460–13474, May 1994.

[176] A. a. Puretzky, D. B. Geohegan, and C. M. Rouleau, "Narrow and intense resonances in the low-frequency region of surface-enhanced Raman spectra of single-wall carbon nanotubes," *Physical Review B - Condensed Matter and Materials Physics*, vol. 82, pp. 1–9, 2010.

[177] J. Sloan, R. Carter, A. Vlandas, R. R. Meyer, Z. Liu, K. Suenaga, P. J. D. Lindan, G. Lin, J. Harding, E. Flahaut, C. Giusca, S. R. P. Silva, J. L. Hutchison, and A. I. Kirkland, *Microscopy of Semiconducting Materials 2007*, ch. Band-Gap Modification Induced in HgTe by Dimensional Constraint in Carbon Nanotubes: Effect of Nanotube Diameter on Microstructure, pp. 213–216. Dordrecht: Springer Netherlands, 2008.

[178] J. Huso, J. L. Morrison, J. Mitchell, E. Casey, H. Hoeck, C. Walker, L. Bergman, W. M. H. Oo, and M. D. McCluskey, "Optical transitions and multiphonon raman scattering of cu doped zno and mgzno ceramics," *Applied Physics Letters*, vol. 94, no. 6, 2009.

[179] J. Kürti, V. Zólyomi, A. Grüneis, and H. Kuzmany, "Double resonant raman phenomena enhanced by van hove singularities in single-wall carbon nanotubes," *Phys. Rev. B*, vol. 65, p. 165433, Apr 2002.

[180] A. A. Puretzky, D. B. Geohegan, and C. M. Rouleau, "Narrow and intense resonances in the low-frequency region of surface-enhanced raman spectra of single-wall carbon nanotubes," *Phys. Rev. B*, vol. 82, p. 245402, Dec 2010.

[181] Y. Shen, N. Quirke, and D. Zerulla, "Polarisation dependence of the squash mode in the extreme low frequency vibrational region of single walled carbon nanotubes," *Applied Physics Letters*, vol. 106, no. 20, 2015.

[182] M. Sendova, E. Flahaut, and T. Hartsfield, "Temperature dependence of raman scattering in filled double-walled carbon nanotubes," *Journal of Applied Physics*, vol. 108, no. 4, pp. 044309–044309–6, 2010.

[183] P. Bernath, *Spectra of Atoms and Molecules*. Oxford University Press, 2005.

[184] K. Refson, P. R. Tulip, and S. J. Clark, "Variational density-functional perturbation theory for dielectrics and lattice dynamics," *Phys. Rev. B*, vol. 73, p. 155114, Apr 2006.

[185] J. P. Perdew, K. Burke, and M. Ernzerhof, "Generalized gradient approximation made simple," *Phys. Rev. Lett.*, vol. 77, pp. 3865–3868, Oct 1996.

[186] S. J. Clark, M. D. Segall, C. J. Pickard, P. J. Hasnip, M. J. Probert, K. Refson, and M. C. Payne, *First principles methods using CASTEP*, vol. 220. 2005. Times Cited: 1438.

[187] J. Chu, *New Data and Updates for III-V, II-VI and I-VII Compounds*, ch. HgTe: band structure, density of states, pp. 403–405. Berlin, Heidelberg: Springer Berlin Heidelberg, 2010.

[188] S. B. Cronin, Y. Yin, A. Walsh, R. B. Capaz, A. Stolyarov, P. Tangney, M. L. Cohen, S. G. Louie, A. K. Swan, M. S. Ünlü, B. B. Goldberg, and M. Tinkham, "Temperature dependence of the optical transition energies of carbon nanotubes: The role of electron-phonon coupling and thermal expansion," *Phys. Rev. Lett.*, vol. 96, p. 127403, Mar 2006.

[189] F. Simon, R. Pfeiffer, and H. Kuzmany, "Temperature dependence of the optical excitation lifetime and band gap in chirality assigned semiconducting single-wall carbon nanotubes," *Phys. Rev. B*, vol. 74, p. 121411, Sep 2006.

[190] P. May, H. Telg, G. Zhong, J. Robertson, C. Thomsen, and J. Maultzsch, "Observation of excitonic effects in metallic single-walled carbon nanotubes," *Phys. Rev. B*, vol. 82, p. 195412, Nov 2010.

[191] H. Telg, J. Maultzsch, S. Reich, F. Hennrich, and C. Thomsen, "Chirality distribution and transition energies of carbon nanotubes," *Phys. Rev. Lett.*, vol. 93, p. 177401, Oct 2004.

[192] . Vasili Perebeinos, J. Tersoff, , and P. Avouris, "Radiative lifetime of excitons in carbon nanotubes," *Nano Letters*, vol. 5, no. 12, pp. 2495–2499, 2005. PMID: 16351202.

[193] M. Huang, H. Yan, C. Chen, D. Song, T. F. Heinz, and J. Hone, "Phonon softening and crystallographic orientation of strained graphene studied by raman spectroscopy," *Proceedings of the National Academy of Sciences*, vol. 106, no. 18, pp. 7304–7308, 2009.

[194] N. R. Raravikar, P. Keblinski, A. M. Rao, M. S. Dresselhaus, L. S. Schadler, and P. M. Ajayan, "Temperature dependence of radial breathing mode raman frequency of single-walled carbon nanotubes," *Phys. Rev. B*, vol. 66, p. 235424, Dec 2002.

[195] P. G. Klemens, "Anharmonic decay of optical phonons," *Phys. Rev.*, vol. 148, pp. 845–848, Aug 1966.

[196] M. Zoli, "Temperature-dependent frequency shifts and broadening of phonon linewidths in lead," *Journal of Physics: Condensed Matter*, vol. 3, no. 33, p. 6249, 1991.

[197] S. Anand, P. Verma, K. Jain, and S. Abbi, "Temperature dependence of optical phonon lifetimes in znse," *Physica B: Condensed Matter*, vol. 226, no. 4, pp. 331 – 337, 1996.

[198] J. Menéndez and M. Cardona, "Temperature dependence of the first-order raman scattering by phonons in si, ge, and $\alpha - \mathrm{Sn}$: Anharmonic effects," *Phys. Rev. B*, vol. 29, pp. 2051–2059, Feb 1984.

[199] A. Grüneis, R. Saito, G. G. Samsonidze, T. Kimura, M. A. Pimenta, A. Jorio, A. G. S. Filho, G. Dresselhaus, and M. S. Dresselhaus, "Inhomogeneous optical absorption around the K point in graphite and carbon nanotubes," *Phys. Rev. B*, vol. 67, p. 165402, Apr 2003.

[200] A. Jorio, M. Dresselhaus, R. Saito, and G. Dresselhaus, *Raman Spectroscopy in Graphene Related Systems*. Wiley, 2011.

[201] A. Garciacristobal, A. Cantarero, C. Trallero‐giner, and M. Cardona, "Excitonic model for 2nd‐order resonant raman‐scattering," *Physical Review B*, vol. 49, no. 19, pp. 13430–13445, 1994.

[202] D. Wallace, *Thermodynamics of Crystals*. Dover books on physics, Dover Publications, 1998.

[203] X. B. Zhang, T. Taliercio, S. Kolliakos, and P. Lefebvre, "Influence of electron-phonon interaction on the optical properties of iii nitride semiconductors," *Journal of Physics: Condensed Matter*, vol. 13, no. 32, p. 7053, 2001.

[204] B. Fain, A. Boeglin, and S. H. Lin, "Theory of multiphoton processes: General formalism," *The Journal of Chemical Physics*, vol. 88, no. 12, pp. 7559–7571, 1988.

[205] D. M. Basko, "Theory of resonant multiphonon raman scattering in graphene," *Phys. Rev. B*, vol. 78, p. 125418, Sep 2008.

[206] J. Bardeen and D. Pines, "Electron-phonon interaction in metals," *Phys. Rev.*, vol. 99, pp. 1140–1150, Aug 1955.

[207] N. Bock, *The electron-phonon interaction in metals*. PhD thesis, State University of New York at Buffalo, 2004.

[208] P. A. M. Dirac, "The quantum theory of the emission and absorption of radiation," *Proceedings of the Royal Society of London A: Mathematical, Physical and Engineering Sciences*, vol. 114, no. 767, pp. 243–265, 1927.

[209] E. Pike and S. Sarkar, *The Quantum Theory of Radiation*. Clarendon Press, 1995.

[210] a. V. Koudinov, Y. G. Kusrayev, D. Wolverson, L. C. Smith, J. J. Davies, G. Karczewski, and T. Wojtowicz, "Giant modulation of resonance Raman scattering from (Cd,Mn)Te quantum wells by secondary illumination," *Physical Review B - Condensed Matter and Materials Physics*, vol. 79, pp. 1–4, 2009.

[211] J. Hegarty, M. D. Sturge, C. Weisbuch, A. C. Gossard, and W. Wiegmann, "Resonant rayleigh scattering from an inhomogeneously broadened transition: A new probe of the homogeneous linewidth," *Phys. Rev. Lett.*, vol. 49, pp. 930–932, Sep 1982.

[212] R. M. Martin and C. M. Varma, "Cascade theory of inelastic scattering of light," *Phys. Rev. Lett.*, vol. 26, pp. 1241–1244, May 1971.

[213] R. Zeyher, "Calculation of resonant second-order raman efficiencies for allowed and forbidden scattering," *Phys. Rev. B*, vol. 9, pp. 4439–4447, May 1974.

[214] M. S. Hofmann, J. T. Gluckert, J. Noe, C. Bourjau, R. Dehmel, and A. Hogele, "Bright, long-lived and coherent excitons in carbon nanotube quantum dots," *Nat Nano*, vol. 8, pp. 502–505, July 2013.

[215] P. S. Gill, S. R. Sauerbrunn, and M. Reading, "Modulated differential scanning calorimetry," *Journal of Thermal Analysis*, vol. 40, no. 3, pp. 931–939, 1993.

List of Publications

Raman Spectroscopy of Optical Transitions and Vibrational Energies of 1 nm HgTe Extreme Nanowires within Single Walled Carbon Nanotubes Joseph H. Spencer, John M. Nesbitt, Harrison Trewhitt, Reza J. Kashtiban, Gavin Bell, Victor G. Ivanov, Eric Faulques, Jeremy Sloan, and David C. Smith ACS Nano 2014 8 (9), 9044-9052 DOI: 10.1021/nn5023632

Resonance Raman Spectroscopy of Extreme Nanowires and Other 1D Systems Smith, D. C., Spencer, J. H., Sloan, J., McDonnell, L. P., Trewhitt, H., Kashtiban, R. J., et al. J. Vis. Exp. (110), e53434, doi:10.3791/53434 (2016).

A Versatile Precursor System for Supercritical Fluid Electrodeposition of Main-Group Materials Bartlett, P. N., Burt, J., Cook, D. A., Cummings, C. Y., George, M. W., Hector, A. L., Hasan, M. M., Ke, J., Levason, W., Pugh, D., Reid, G., Richardson, P. W., Smith, D. C., Spencer, J., Suleiman, N. and Zhang, W. (2016), Chem. Eur. J., 22: 302-309. doi:10.1002/chem.201503301

Electrodeposition of Protocrystalline Germanium from Supercritical Difluoromethane C. Y. Cummings, P. N. Bartlett, D. Pugh, G. Reid, W. Levason, M. M. Hasan, A. L. Hector, J. Spencer, D. C. Smith, S. Marks, R. Beanland, ChemElectroChem 2016, 3, 726.

Supercritical Fluid Electrodeposition of Elemental Germanium onto Titanium Nitride Substrates Charlie Y. Cummings, Philip N. Bartlett, David Pugh, Gillian Reid, William Levason, Mahboba M. Hasan, Andrew L. Hector, Joe Spencer, and David C. Smith J. Electrochem. Soc. 2015 162(14): D619-D624;doi:10.1149/2.0771514jes